

Sprinkler Irrigation Precipitation Pattern Simulation: Model Development and Evaluation

D. Zerihun and C.A. Sanchez

University of Arizona
Maricopa Agricultural Center
37860 West Smith-Enke Road
Maricopa, Arizona 85138

A report submitted to the USBR
February 2014

Contents

Executive summary	6
Chapter 1. Introduction	10
Chapter 2. Process description	12
2.1. Formation of artificial precipitation under no-wind condition	12
2.2. Droplet size distribution measurement and characterization	16
2.3. Droplet motion, interaction among droplets and with the ambient air under field conditions	18
2.4. Simplifying assumptions and process conceptualization for physical modeling	18
2.4.1. Precipitation pattern about a sprinkler under no-wind condition	21
2.4.2. Precipitation pattern about a sprinkler under field conditions	23
Chapter 3. Sprinkler irrigation droplet dynamics modeling	25
3.1. Literature review	25
3.2. Equations used in the numerical droplet dynamics model developed in the current study	29
3.3. Special cases and parameter values	32
3.4. Numerical solution	34
3.4.1. Runge-Kutta method, a review	35
3.4.2. Adaptive step-size Runge-Kutta methods	39
3.4.3. Applications to the solution of a system of equations	42
3.5. Flow chart and computational procedure	48
Chapter 4. Sprinkler droplet volumetric application rate computation and precipitation pattern simulation	51
4.1. Introduction	51
4.2. Assumptions and rationale	52
4.2.1. Droplet volumetric application rate based on indoor measurements	52
4.2.2. Model calibration based on field measurements	56
4.2.3. Sprinkler precipitation pattern simulation under field conditions	60
4.3. Computational procedures	61
4.3.1. Droplet volumetric application rates	61
4.3.2. Spatial distribution of sprinkler irrigation	66
Chapter 5. Description of the components of the sprinkler irrigation precipitation pattern simulation model	69
Chapter 6. Model evaluation	72
6.1. Comparison of the numerical model with analytical solutions	73
6.2. Wind effects on droplet motion, simulation based analysis	77
6.3. Model evaluation with measured data and potential field-scale application	86
6.3.1. Indoor single sprinkler tests, datasets, and model evaluation	86
6.3.2. Single sprinkler evaluations under field condition	95
6.3.3. Potential application to field-scale sprinkler irrigation simulation and performance evaluation	105
Chapter 7. Sprinkler irrigation uniformity field evaluation	110
Chapter 8. Summary and Recommendations	114
References	121

List of figures

Figure 1. Schematics of the conceptualization of precipitation pattern about a sprinkler for droplet dynamics modeling	22
Figure 2 Velocity diagram depicting droplet absolute and relative velocity vectors, and wind velocity vector (where α = angle between wind velocity and droplet absolute velocity vector, β = angle between droplet absolute and relative velocity vectors and Θ = angle between wind velocity and droplet relative velocity vector)	28
Figure 3. Simplified flow diagram for the droplet dynamics submodel (Runge-Kutta approximation)	49
Figure 4. (a) Measured radial sprinkler application rate and (b) Annular ring of irrigated areas representing the radial discretization of the wetted area under the sprinkler (where r_i = the radial distance, measured from sprinkler location to, the landing point on the irrigated surface of the i th droplet diameter; R_i = the radius of the i th concentric circle delineating the i th annular ring of irrigated area from the $(i+1)$ th)	53
Figure 5 Angular setting of sprinkler nozzle from the reference axis, θ_{hx0} , and sprinkler vertical tilt angle, θ ,	54
Figure 6 Discretization of the irrigated field surface for sprinkler irrigation precipitation distribution computation (x and y = horizontal coordinate axes which represent distances on the field surface and z = the vertical coordinate, which represents applied irrigation depth or precipitation rate, Δx and Δy = grid dimensions)	58
Figure 7 Flow diagram for droplet volumetric application rate computation	62
Figure 8 Sprinkler precipitation pattern simulation under field condition	64
Figure 9 Input data sets and their relationship with the main computational phases of a sprinkler irrigation precipitation pattern simulation model	70
Figure 10 Comparison of droplet trajectories computed with the numerical and analytical models for different initial conditions	75
Figure 11 (a) Comparison of droplet radial distances computed, with the numerical and analytical models, as a function of sprinkler nozzle vertical tilt angle and (b) droplet trajectories as a function sprinkler vertical tilt angle	76
Figure 12 Droplet trajectories for wind speed of 1.25m/s and wind vector azimuth of: (a) 0° , (b) 180° , (c) 45° , (d) 225° , (e) 90° , and (f) 270° (The reference axis for measuring the angular setting of the sprinkler nozzle is the longer horizontal axis; note that the positive and negative algebraic signs in axis labels are meant to emphasize that distance measurement were made in opposite spatial direction from the origin of the coordinate system)	78
Figure 13 Droplet motion for wind speed of 2.5m/s and wind vector azimuth of: (a) 0° , (b) 180° , (c) 45° , (d) 225° , (e) 90° , and (f) 270° (The reference axis for measuring the angular setting of the sprinkler nozzle is the longer horizontal axis; note that the positive and negative algebraic signs in axis labels are meant to emphasize that distance measurement were made in opposite spatial direction from the origin of the coordinate system)	80

Figure 14	Droplet drift and radial landing distances: (a) Normalized droplet wind drift as a function of droplet diameter for wind speed of 1.25m/s, (b) Normalized droplet drift as a function droplet diameter for wind speed of 2.5m/s, (c) Drift ratio as a function of droplet diameter for wind speed of 1.25m/s, (d) Drift ratio as a function of droplet diameter for wind speed of 2.5m/s, (e) Normalized droplet radial distance as a function wind vector azimuth for wind speed of 1.25m/s, and (f) Normalized droplet radial distance as a function wind vector azimuth for wind speed of 2.5m/s	83
Figure 15	A sketch of the layout of the single sprinkler indoor test apparatus: (a) plan view and (b) isometric view	87
Figure 16	A comparison of sprinkler radial application rates (obtained through indoor measurements, regression fit, and simulated) for sprinkler pressure head: (a) 28.1m (40.0psi), (b) 35.2m (50.0psi), (c) 42.2m (60.0psi), (d) 70.0m (49.2psi), and (e) Aggregate comparison of simulated radial application data with regression fit	91
Figure 17	A sketch of the layout of the single sprinkler field test apparatus (plan view)	96
Figure 18	Layout of the overlapped sprinkler set for model evaluation	103
Figure 19	Contours depicting the spatial distribution of sprinkler applied irrigation water (precipitation) that reached the irrigated field surface for sprinkler and lateral spacing's of 9.16m×10.67m: (a) Field-scale and (b) Plot-scale	107
Figure 20	Contours depicting the spatial distribution of sprinkler applied irrigation water (precipitation) that reached the irrigated field surface for sprinkler and lateral spacing's of 9.16m×13.67m: (a) Field-scale and (b) Plot-scale	109

List of tables

Table 1 Parameters of the fifth order Runge-Kutta formula with an embedded fourth order approximation	46
Table 2 Datasets used in the comparison of the numerical and analytical solutions and in the analysis of wind effects on droplet motion	74
Table 3 Datasets from indoor single sprinkler tests used in model evaluation	89
Table 4 Input data used in model evaluation, single-sprinkler indoor tests	93
Table 5 Measured data during single sprinkler field evaluations	98
Table 6 Input data used in numerical model evaluation, comparison with field data	100
Table 7 Irrigation uniformity and depths computed based on measured and simulated precipitation patterns of the overlapped sprinklers	104
Table 8 Field-scale irrigation application uniformity, maximum, minimum, and average depths	112

Executive Summary

Solid set sprinkler irrigation systems are increasingly used for season long vegetable production in the Yuma Valley Irrigation Districts. The main benefit of replacing furrow irrigation with sprinklers is a significant increase in irrigation performance, and hence reduced water and fertilizer use. Existing systems were configured primarily to provide supplementary irrigation during the early part of the vegetable crop growing season. However, with season long use efficient and uniform application of irrigation water has become a concern to growers. Improvements in the performance of irrigation systems can be realized through evaluation of existing systems and operational practices, identification of limitations, if any, and the development of design and management tools as well as guidelines for best practices.

With support from the Arizona Specialty Crops Council and the USBR, over the last couple of years, authors have conducted field and modeling studies of solid set sprinkler irrigation systems in the Yuma Valley Irrigation Districts (Zerihun et al., 2011; Zerihun and Sanchez, 2012). During the autumn-winter seasons of 2011-2013, field-scale sprinkler irrigation uniformity tests and hydraulic (pressure head and discharge) evaluations were undertaken in growers' fields. An important outcome of the field studies consists of the development of a procedure (materials and methods) for field-scale irrigation uniformity evaluations. Results of these studies suggest that for the system configuration and irrigation (operation and maintenance) practices common in the Yuma Valley Irrigation Districts, typical irrigation application uniformity levels are high: average field-scale Christiansen's uniformity coefficient (*UCC*) of about 0.85 and a low-quarter distribution uniformity (*DUI_q*) of about 0.75. However, a few of the irrigation systems evaluated so far exhibited field-wide irrigation uniformities that fell well below the level considered satisfactory for solid-set sprinkler systems. In addition, the results also showed that even when the field-scale irrigation uniformities are high, significant localized deviations from the field averages were observed within a field. This highlights the significance of proper setting and routine maintenance and replacement of system components. It also underlines the need for field-scale irrigation uniformity evaluations to be performed based on more than one plot-scale tests, suitably distributed through the field.

Field studies can provide a realistic evaluation of irrigation uniformity levels. However, mathematical models present a more flexible and inexpensive alternative for developing optimal sprinkler irrigation system design and management recommendations. A mathematical model that can fully characterize the performance (uniformity, adequacy, and efficiency) of a field sprinkler irrigation system should be based on the coupling of a field-scale hydraulic submodel with components for simulating precipitation pattern about a sprinkler and soil water flow processes. The development of a computationally efficient and robust field-scale sprinkler irrigation model with such a capability remains a challenge. However, as a step towards this goal, the authors have developed a hydraulic model that can simulate the spatial distribution of pressure heads and discharges of field-scale solid set sprinkler systems, given system hydraulic, geometric, and topographic characteristics (Zerihun et al., 2014 and Zerihun and Sanchez, 2014a). Limited evaluations of the hydraulic model, through a comparison of model output with measured data, suggest that the model is accurate. The model also has a functionality for computing field-scale irrigation performance based on measurements.

Modeling studies and measured field-scale hydraulic data show that the hydraulic design of typical sprinkler systems, in the Yuma Valley Irrigation Districts, is robust: system hydraulics exhibit low sensitivity to appreciable changes in pipe hydraulic resistance and field slopes. The implication is that field-scale irrigation uniformity should be virtually insensitive to variations in these factors within reasonable ranges, provided the system is well maintained, the sprinkler characteristics is fairly uniform, system is properly installed, and is operated under ambient weather conditions conducive for the attainment of high irrigation uniformities (especially sufficiently low wind speed). However, the studies have also noted that a sprinkler system with high irrigation application uniformity, or even efficiency, may not necessarily be optimal from the perspective of economic return. Hence, a more comprehensive field-scale sprinkler system evaluation may need to be based on economic criteria to compare existing system layouts, pipe diameters, pipe appurtenances, and sprinkler combinations with potential alternatives.

As part of the study reported here authors have worked on the development of a sprinkler irrigation precipitation pattern simulation model. Such models typically consist of two main components (Fukui et al., 1980; von Bernuth and Gilley, 1984; Seginer, et al., 1991; Carrion, et

al., 2001; Playan et al., 2006). Droplet population size and diameter ranges (factors related to the physical processes of droplet formation) along with droplet volumetric application rates are approximated with a semi-empirical procedure as a function of sprinkler design factors and nozzle pressure heads. A droplet dynamics model, that solves the equation of motion numerically, is used to simulate the trajectories (through the ambient air) and eventual landing coordinates on the irrigated surface of the individual droplets as dictated by gravitational, drag, and wind drift forces. Output of the droplet dynamics model can then be combined with the semi-empirically determined droplet volumetric application rate data to derive an estimate of the spatial distribution of precipitation about a sprinkler. Wind effects on droplet motion under sprinkler irrigated conditions are taken into account with empirical drag correction coefficients derived based on measured field data (Seginer, et al., 1991; Carrion, et al., 2001; Playan et al., 2009).

The sprinkler precipitation pattern simulation model developed here is capable of simulating the spatial distribution of irrigation about sprinklers taking into account sprinkler design factors, sprinkler riser pipe height, nozzle pressure heads, and wind effects. Following the pattern described above, the model consists of two main components. The combination of computational and experimental (indoor and field) methods used in this study to determine droplet population size, diameter ranges, and volumetric application rates and to estimate model parameters, related to wind effects on droplet motion, are largely based on the works of Fukui et al. (1980), Seginer, et al. (1991), and Carrion, et al. (2001). Derivation of the equations that forms the basis of the droplet dynamics modeling functionality developed here combines established ideas proposed in earlier studies, cited above, and also new concepts formulated as part of the current study in the accompanying document (Zerihun and Sanchez, 2014b). The set of nonlinear ordinary differential equations, governing droplet motion through the ambient air, derived as such are solved numerically with an embedded Runge-Kutta formulas consisting of a fourth-fifth order pair (Mathewes and Fink, 2004; Press et al., 1997; Burden et al., 1981). In addition, the physics of droplet dynamics as applied to sprinkler irrigation is reviewed in some detail and an alternative set of nonlinear differential equations, describing an impulsively started droplet motion through a viscous fluid (e.g., ambient air) that could be in a uniform horizontal motion itself, was derived in the accompanying document.

Evaluation of the sprinkler precipitation pattern simulation model, developed here, was undertaken at two levels. First, the output of the numerical droplet dynamics submodel was compared with a simplified analytical model, under applicable conditions. The results show that the numerical and analytical solutions are in good agreement, suggesting that the representation, in the numerical model, of the physics underlying droplet dynamics is sound. In addition, analyses of the numerical solutions of the equations governing droplet motion under wind conditions show that model predictions are largely consistent with intuitive physical reasoning. Model evaluation results also indicate that model predicted sprinkler radial precipitation patterns, for a range of nozzle pressure heads, compare reasonably well with measurements obtained under no-wind conditions. Furthermore, a limited functional evaluation of the model, based on a comparison of model predicted and field measured irrigation uniformity and precipitation depths, suggest that the accuracy of the model is satisfactory.

As part of the study reported here, the potential application of the precipitation pattern simulation model in field-scale irrigation performance (uniformity, application efficiency, and adequacy) evaluation was explored. Field wide spatial distribution of sprinkler pressure heads computed with the hydraulic model, cited above, was used as an input to the precipitation pattern simulation model. The results of the field-scale simulation study suggest that the development of a coupled hydraulic, precipitation pattern, and soil water flow simulation model for use in field wide irrigation performance evaluation is technically feasible. However, for the coupled field-scale irrigation model to be efficient and practically useful some significant limitations of the sprinkler irrigation precipitation pattern simulation model, pertaining to numerical efficiency and parameter estimation, need to be addressed prior to model coupling.

Additional field-scale irrigation uniformity evaluations were conducted in growers' fields in the Yuma Valley Irrigation Districts as part of the current study. Measured field-scale UCC and DU_{Iq} exceed 0.83 and 0.75, respectively, for two of the evaluation fields. However, the field-scale irrigation uniformities for two other fields, covered in the current study, fell appreciably short of what could be considered as satisfactory level for solid-set sprinkler systems (with $UCC < 0.75$ and $DU_{Iq} \leq 0.58$). Note that these results are largely in agreement with those obtained in earlier studies conducted by the authors. However, the poor irrigation performance in some of these fields points to the need for a follow up study, aimed at determining the

contributory factors, through evaluation of the current irrigation (maintenance and operational) practices and the hydraulics of the sprinkler systems.

The report documented here consists of eight chapters. Chapter 1 presents the introductory section. Process description, including formation of artificial precipitation as well as simplifications and assumptions needed to reduce process complexity to a level that is physically and mathematically tractable, is presented in Chapter 2. Chapter 3 presents a review of sprinkler irrigation droplet dynamics modeling along with a summary of the governing equations and numerical solutions implemented in the model described here. Chapter 4 discusses computational and experimental procedures used in the determination of droplet volumetric application rates, model calibration taking into account wind effects, and the steps involved in precipitation pattern simulation. Chapter 5 provides a concise description of the components of the sprinkler irrigation precipitation pattern simulation model. Results of model evaluation are presented in Chapter 6. Chapter 7 discusses measured field-scale irrigation uniformity evaluation data. Chapter 8 presents a summary of the report and lists recommendations for further studies.

Chapter 1 Introduction

The use of solid set sprinkler systems for season long vegetable production in the Yuma Valley Irrigation Districts is expanding. With season long operation, uniform and efficient application of irrigation water with sprinkler systems has become a prime concern for growers. Efficient irrigations can be realized through the evaluation of existing systems and current operational practices, identification of limitations if any, and the development of design and management tools as well as guidelines for best practices.

Over the last couple of years (2010-2013), the authors have conducted field and modeling studies of solid set sprinkler irrigation systems in the Yuma Valley Irrigation Districts (e.g., Zerihun et al., 2011; Zerihun and Sanchez, 2012). The field studies have led to the development of a procedure for field-scale irrigation uniformity evaluations. Results of these studies suggest that typical field wide irrigation application uniformities in the Yuma Valley could be high, with average field-scale UCC and DU_{lq} of about 0.85 and 0.75, respectively. However, measured

field-scale irrigation uniformities in a small fraction of the fields evaluated so far was appreciably lower than the levels considered satisfactory for solid-set sprinkler systems. The results of the field studies have also shown that, even when field-scale irrigation uniformities are high, significant variations in uniformity levels exist within a field.

Sound design and management of sprinkler systems is key to the efficient irrigation of crops. Mathematical models represent flexible and inexpensive irrigation system design and management tools. A sprinkler irrigation model that can be used for system design and management needs to have the following modeling components: a hydraulic component, a precipitation pattern simulation functionality, and an infiltration and soil water flow submodel. As a step towards the development of such a capability, a hydraulic model for simulating the field-scale spatial distribution of nozzle pressure head and discharge given the sprinkler system hydraulic, geometric, and topographic characteristics was developed (Zerihun et al., 2014; Zerihun and Sanchez, 2014a). A limited evaluation of the model with field data suggests that the model is accurate. The model also has a functionality for computing field-scale irrigation performance based on test-plot scale field measurements.

Results of the field and modeling studies suggest that a typical sprinkler system in the Yuma Valley Irrigation Districts has a robust hydraulic design. The implication is that system performance should show very low sensitivity to appreciable changes in pipe hydraulic resistance characteristics and field slopes, provided the systems are properly set, maintained, and operated under conducive weather condition. However, the studies have also noted that a system with high irrigation performance is not necessarily equivalent to a system with high economic return.

As a follow up to the modeling studies, described above, during 2013 authors have been working on the development of a sprinkler irrigation precipitation pattern simulation model. The model is based on a numerical solution of the governing equations of droplet dynamics, to simulate droplet motion through the ambient air, and a semi-empirical approximation of the droplet formation process and wind effects on droplet motion. It has the capability to compute the spatial distribution of irrigation about a sprinkler, as a function of sprinkler design characteristics (nozzle diameter and vertical tilt angle), sprinkler riser pipe height, nozzle pressure head, and wind velocity. The model was evaluated based on theoretical analyses and a

comparison of model output with measured data, obtained through single sprinkler indoor and field tests. The results suggest that the accuracy of model prediction is satisfactory.

Potential applications of the precipitation pattern modeling functionality in the simulation of field-scale spatial distribution of irrigation and performance characterization was explored. The result show that the development of a field-scale sprinkler irrigation design, management, and evaluation tool through the integration of the precipitation pattern modeling functionality with the sprinkler hydraulic submodule and a soil water balance computation component is technically feasible, once existing limitations as related to numerical efficiency and parameter estimation of the model described above are addressed.

The overall objective of the study reported here is to conduct additional field evaluations in the Yuma Valley Irrigation Districts and to develop, and evaluate through comparison with measured data, a sprinkler irrigation precipitation pattern simulation model. The specific objectives of the study documented here are: (1) To conduct additional field evaluations in the Yuma Valley Irrigation Districts aimed at a more complete characterization of the range of variation of irrigation performance in the area, (2) To develop a sprinkler irrigation precipitation pattern simulation model based on the physics of droplet dynamics and to conduct a limited evaluation of the model with measured data, (3) To explore the potential application of the precipitation pattern simulation model in field-scale sprinkler irrigation simulation and irrigation performance computation; and (4) To develop recommendations for further study.

Chapter 2 Process description

2.1 Formation of artificial precipitation under no-wind condition

A typical field-scale solid set sprinkler system consists of an open pipeline network of aluminum pipes consisting of a main and laterals operating under pressure. Each lateral is fitted with regularly spaced riser pipes supporting a sprinkler head, which distributes water over the irrigated field in the form of precipitation. The type of sprinklers commonly used with solid-set sprinkler systems in the Yuma Valley Irrigation Districts, and are of interest in the study reported here, are the low to medium capacity impact sprinklers (typically operated with pressure ranging

between about 40.0psi-90psi). Descriptions of the component parts and the mechanisms of operation of these sprinklers can be obtained from manufacturers' catalogue (e.g., *WeatherTech*: <http://www.weathertec.com> and *Rainbird*: <http://www.rainbird.com>). With these sprinklers, the sprinkler head is equipped with a spring loaded spoon like structure (known as the oscillating or impact arm) onto which the water jet emerging from the nozzle periodically impinges. The impact of the water jet on the oscillating arm provides the mechanical energy for rotating the sprinkler about its vertical axis. It also modifies the precipitation pattern about a sprinkler, mainly increasing the application rate at short and medium distances and reducing application rate at larger distances from the sprinkler (Bilanski and Kidder, 1958; Salvador et al., 2009) and reducing the wetted radius (Bilanski and Kidder, 1958; Burguete et al., 2007).

Under no-wind condition, the precipitation pattern about a sprinkler and the corresponding irrigation application rate are considered symmetrical about the sprinkler. Hence, the field-scale application of sprinklers generally requires the wetted areas of adjacent sprinklers to be overlapped in order to irrigate a continuous tract of cropland. The implication is that the radial application pattern of a single sprinkler (a point source of water) is not only inherently nonuniform, but it need not be uniform. It is, however, desirable for the application pattern about a sprinkler to be such that, when the wetted areas of adjacent sprinklers are overlapped, an acceptably high level of field-scale irrigation uniformity is produced.

Given a sprinkler, nozzle operating pressure, and ambient weather condition, the irrigation stream issuing from a sprinkler nozzle consists of a water jet of some degree of coherence. In the course of its motion through the ambient air, the water jet breakup into water droplets of varying sizes and reaches the surface of the irrigated field in the form of artificial precipitation (Kohl, 1974; Kincaid, et al., 1996; Salvador et al., 2009). The distribution of droplet sizes with distance from the sprinkler nozzle is the most important determinant of the resulting irrigation water distribution about a sprinkler.

A qualitative description of the sprinkler irrigation stream breakup process, in the absence of the oscillating arm of the sprinkler, is described by Kohl (1974) and Salvador et al. (2009). A more rigorous physical and analytical description of the mechanisms of liquid jet breakup is provided by others (e.g., Miesse, 1955). The actual mechanics of the breakup and disintegration of a water jet from a sprinkler nozzle is complex and a rigorous description of it is

outside the scope of this study. Overall as the liquid jet emerges from the nozzle into the atmosphere, the sudden change in the interaction of the forces acting on it introduces instability into the coherence and integrity of the stream (Kohl, 1974; Miesse, 1955), the progression of which eventually leads to the complete disintegration of the liquid jet into a range of droplet sizes. Both experimental (Kohl, 1974; Salvador et al., 2009) and theoretical observations (e.g., Miesse, 1955) suggest that at short and medium distances from the sprinkler nozzle the mechanisms responsible for the formation of finer droplets dominate the process and those leading to the formation of larger droplets takeover close to the far end of the sprinkler wetted radius. Finer droplets form at the surface of the liquid jet as a result of the interaction of turbulent eddies in the liquid column and drag at the water-air interface (Kohl, 1974; Miesse, 1955). On the other hand, finer droplets observed at the far end of the wetted diameter of the sprinkler can often be associated with the breakup of larger droplets into smaller ones. This phenomenon, also referred to as secondary atomization process, is discussed in the context of a theoretical analysis of liquid jet breakup processes by Miesse (1955). The processes responsible for the formation of smaller droplets occur at the liquid-air interface, and hence to a significant extent affected by the relative velocity of the liquid jet with respect to the ambient air (Kohl, 1974). However, close to the far end of the sprinkler wetted radius, the progressive roughening of the surface of the expanding liquid jet and the concomitant increase in drag results in a more rapid deceleration of, and increased air entrainment into, the liquid jet leading to its eventual disintegration, forming mainly larger water droplets. Note that observation of sprinkler operation suggests that the preceding description of distances from sprinkler, as related to the formation of different droplet diameters, is comparative and depends on nozzle pressure head and sprinkler design factors.

Overall droplet size distribution is a function of the average cross-sectional velocity of the water jet and its diameter (Miesse, 1955; Kohl, 1974), pertinent physical properties of water and the ambient air, the state of motion of the ambient air, and the nature and physical properties of the initial instabilities in the water jet (Miesse, 1955). In the context of sprinkler irrigation, the average cross-sectional velocity of the water jet and its diameter are directly related to sprinkler nozzle size and operating pressure. In addition, the nature and physical properties of the instabilities introduced into the water jet is, to a significant extent, related to the internal design of the sprinkle nozzle. For example, Bilanski and Kidder (1958) have shown through

experimental studies that differences in the internal configurations of the sprinkler nozzle (in terms of the shape, surface roughness, surface grooving, and size of nozzle elements) can have substantial effect on irrigation application patterns about a sprinkler (application rate and wetted radius). Bilanski and Kidder (1958) attributed the effect of the internal design of the sprinkler to the kind of turbulence structure that the nozzle elements impart to the emerging water jet.

The introduction of an impact arm to the sprinkler is known to result in a significant modification to the radial water distribution pattern about a sprinkler relative to the condition without an impact arm (Bilanski and Kidder, 1958). The change in the radial application rate about a sprinkler (increased application rate near and at medium distance from the sprinkler) could be attributed to a change in the range of droplet sizes formed in that distance range as a result of the mechanical action of the impact arm (Salvador et al., 2009). The reduction in sprinkler wetted radius noted by Bilanski and Kidder (1958) and Burguete et al. (2007), on the other hand, could be attributed to such factors as reduced energy of the water jet upon impact with the oscillating arm (von Bernuth and Gilley, 1984) and to differences in drag intensity under the two sets of conditions (Bilanski and Kidder, 1958; Seginer, 1991).

The preceding discussion shows that a range of droplet sizes are formed at any given distance along the trajectory of the sprinkler water jet. Smaller droplets account for a large fraction of the droplets formed at small to medium distances from a sprinkler, while larger size droplets dominate the population of droplets (statistically speaking) formed close to the distal end of the sprinkler wetted radius.

Measurement and characterization of droplet size distributions at preset radial distances from a sprinkler are key to the analyses and understanding of the relationship between sprinkler design factors and operating conditions, on the one hand, and associated irrigation application rates and precipitation patterns, on the other. A brief review of water droplet size distribution measurement and characterization approaches used in the context of sprinkler irrigation applications is presented in subsequent section.

2.2 Droplet size distribution measurement and characterization

Considering a sprinkler and an operating condition, the droplet size distribution at a given radial distance from the sprinkler, may consist of simple frequency histograms or

functional frequency distribution showing the frequency or cumulative frequency of droplet diameters. However, a useful form, often used in the context of sprinkler irrigation application, consist of one in which measured droplet size distribution at a preset radial distance from the sprinkler is presented in terms of volume percentage and cumulative volume percentage of applied water versus droplet diameter ranges (Kohl, 1974; von Bernuth and Gilley, 1984; Kincaid et al., 1996). The volume percentage associated with a droplet diameter range is the percent, by volume, of irrigation water applied at the location that is attributable to the droplet diameter range. The cumulative volume percentage associated with a given droplet diameter, represents the percent, by volume, of irrigation water applied at a given location by water droplets with diameters less than or equal to a specified value. At any given radial location from a sprinkler, the droplet size distributions expressed in terms of volume and cumulative volume percentages are derived by combining frequency distributions of measured droplet diameters and irrigation depth collected in a rain gage at the same location (Kohl, 1974; Von Bernuth and Gilley, 1984; Kincaid et al., 1996; Salvador et al., 2009).

Given a sprinkler model and nozzle size, droplet size measurements are typically conducted indoors (at zero wind velocity and often under atmospheric conditions that minimize evaporation losses: moderate temperature and high humidity), constant operating pressure head, and known sprinkler riser height. Note that measured droplet size distributions, at any given radial distance from the sprinkler, often refer to the distributions of the droplet sizes observed as the droplets approach the irrigated surface (Salvador, et al., 2009). Droplet size measurement methods used in sprinkler irrigation characterization have been discussed by Kincaid et al. (1996) and Salvador et al. (2009). These methods can broadly be categorized in two types:

(i) The indirect methods rely on the measurement and analysis of some signature left by droplets upon impact on a receiving medium to derive a droplet size frequency distribution at selected radial distances from the sprinkler. The receiving medium could be an absorbent paper in which case the individual stains left by impinging droplets is used to empirically estimate droplet diameters (stain method). It could also be a thin layer of flour in which case the size of the pellets formed by water droplets upon impact is used to derive the corresponding droplet diameters (pellet method, e.g., Kohl 1974).

(ii) The direct methods include those techniques that are based on the analysis of, images of droplets taken while in motion or, the changes that droplet motion through an imposed electromagnetic field induces on the field to estimate droplet diameters and/or velocities. Images of droplets obtained through high speed digital photography can be used to estimate water droplet size distributions and associated velocities at selected radial distance from the sprinkler (Salvador et al., 2009). In addition, the changes that water droplets induce in the properties of an imposed electromagnetic field, as they pass through it, can be analyzed by a detector to determine the droplet sizes (Kincaid et al., 1996). A comparative discussion on the advantages and limitations of some of these methods is provided by Kincaid, et al. (1996) and Salvador et al. (2009). Alternatively, photographs of water droplets trapped in oil can be used to derive droplet size distributions (oil immersion technique, e.g., Eigel and Moore, 1983).

Overall measured sprinkler droplet size distributions show that at each measurement station along the wetted radius a range of droplet diameters are collected (Kohl, 1974; Kincaid et al., 1996; and Slavador et al., 2009). The results also show that the population of finer droplet sizes dominates the droplet size frequency distributions in close vicinity of the sprinkler and at intermediate distances. On the other hand, the frequency of droplets in the smaller diameter range diminishes progressively with distance and at the far end the population of larger droplets dominates the droplet size frequency distribution. Although, as would be expected, the volume percentage of applied irrigation water at the far end of the sprinkler wetted radius is dominated by contributions from large droplet sizes, at short and medium distances from the sprinkler as well the contribution of relatively larger droplets is not insignificant (Kohl, 1974; Von Bernuth and Gilley, 1984; Kincaid et al., 1996; Salvador, et al., 2009). At short and medium distances from the sprinkler, the number of large droplets expressed as a fraction of the total number of droplets collected is small; however, the volumetric contribution of large diameter droplets is appreciable, because droplet volume increases as a cubic function of diameter.

2.3 Droplet motion, interaction among droplets and with the ambient air under field conditions

The process by which a coherent irrigation stream issuing from a sprinkler nozzle completely disintegrates into a range of droplet sizes, before it reaches the irrigated field surface in the form of precipitation, is further complicated by the changes that droplets may undergo during their motion through the ambient air. Water droplets that have already been separated from the water jet may collide with each other and breakup into smaller droplets. The forces exerted by the ambient air on a droplet are modified by the motion of adjacent droplets (Temkin and Kim, 1980; Seginer et al, 1991; Burguete et al., 2007). Larger droplets could undergo substantial deformation as they accelerate through the ambient air (Laws, 1941), which could significantly alter the nature and magnitude of the drag force acting on the droplet compared to an equivalent spherical shaped droplet. In addition, a water droplet of a given size accelerating through the ambient air can remain intact only if its velocity remains within the bounds of a threshold velocity. If this velocity is exceeded the inertial forces become sufficiently large to overcome the force that holds the droplet intact, surface tension (Miesse, 1955; Temkin and Kim, 1980). Hence the droplet can breakup into smaller diameter droplets. Furthermore, water droplets may change in size in the course of their motion due to evaporation (Goering, 1972; Silva and James, 1988; Kincaid and Longley, 1989). Time dependent droplet diameter implies time dependent droplet specific surface area, evaporative surface, and drag characteristics. Finally, the presence of wind which could be unsteady and nonuniform with a time varying direction introduces a substantial modification to the water jet and droplet relative velocities with respect to the ambient air. Noting that relative velocity is an important factor not only in droplet motion (trajectories and final destination) but also in their formation, the significance of wind in irrigation water distribution pattern about a sprinkler cannot be overemphasized.

2.4 Simplifying assumptions and process conceptualization for physical modeling

The preceding discussion highlights the complexity of the physical mechanisms involved in the irrigation stream breakup process, the formation of water droplets, and their subsequent motion through the ambient air and the changes they undergo through interactions among themselves and with the ambient air. A complete physics based simulation capability of the process presented above may require the coupling of a modeling component (describing the

formation and motion of a coherent water jet, its progressive breakup, and eventual disintegration into droplets) with a module for computing the trajectories of the individual water droplets from the point they depart the irrigation stream till they reach the soil surface. The development of such a model is evidently a formidable theoretical undertaking for any application and certainly impractical in the context of sprinkler irrigation modeling. Hence, a simplified conceptualization of the process is often made with the aim of reducing the problem into a mathematically and physical tractable form. With such an approach the intricacies of the physics of sprinkler irrigation stream breakup process is altogether ignored and is supplanted by a simplified conceptual and physical model that uses an empirically determined sprinkler irrigation application rate data. The objective being developing a modeling capability that can reproduce in an approximate sense the essential end result of an irrigation process: the distribution of applied water about a sprinkler, given a set of operating conditions.

At the center of any physics based modeling tool designed to simulate the distribution pattern of irrigation water about a sprinkler is a droplet dynamics model. A droplet dynamics model simulates the motion through the ambient air of individual droplets. The governing equation of droplet dynamics is Newton's second law of motion (Fukui et al., 1980; von Bernuth and Gilley, 1984; Seginer, et al., 1991; Carrion, et al., 2001; Playan et al., 2006). The equation of motion relates the net unbalanced force acting on a water droplet computed as the vector sum of the major forces of aerodynamic drag, droplet weight, and wind drift force with the acceleration of the particle. The resulting set of differential equations can then be solved numerically, given the initial velocity and location of the particle (droplet) as it breaks away from the water jet, to determine its destination and trajectory in a selected coordinate system. While a droplet dynamics model is capable of simulating the motion of individual droplets, the artificial precipitation about a sprinkler consists of countless number of droplets with highly variable droplet diameters and not very well defined initial conditions. Hence, the question is what realistic set of simplifications can be made in order to develop a sprinkler irrigation precipitation pattern simulation model with a physically based droplet dynamics sub-model at the core of it.

From the preceding discussion it is evident that the main sources of complexity in any attempt aimed physics based modeling of precipitation pattern about a sprinkler are:

(i) Uncertainty associated with the initial conditions (velocity and location) of droplets as they form; (ii) Complexity associated with modeling the time evolution of the diameter of individual droplets, in the course of their motion, as affected by evaporation; (iii) Complexity arising from the need to model the effects of changes in droplet shape and droplet-droplet interactions on drag (either directly or indirectly through the effects of droplet motion on the ambient air); and (iv) Complexity associated with modeling the effect of wind on droplet motion, especially taking into account the nonuniform and transient nature of wind. Sprinkler irrigation precipitation pattern simulation models (Fukui et al., 1980; Seginer et al., 1991; Carrion et al., 2001; Playan et al., 2009) are based on a set of simplifying assumptions mainly aimed at reducing these complex features of the actual process of droplet formation and motion to a level that is mathematically tractable, yet sufficiently rigorous to capture the essential features of the process pertinent to irrigation system design and management:

1. Irrigation stream disintegrates into a range of water droplet diameters at the sprinkler nozzle;
2. The initial velocity of the droplets is equal to the average cross-sectional stream velocity at the sprinkler nozzle (which can be computed as a function of nozzle diameter, pressure head, and sprinkler hydraulic characteristics);
3. The individual water droplets move through the ambient air independent of each other (without collision and the forces that the ambient air exert on droplets remain unaffected by the motion of adjacent droplets);
4. Individual water droplets assume spherical shapes at emergence from the nozzle and remain spherical throughout their motion;
5. The diameters of the individual water droplets remain invariant throughout their motion (note that this should not imply that evaporation is neglected. Instead it is a statement of the fact that evaporation is not computed with a mechanistic model per individual droplets basis)
6. Under wind conditions, the ambient air in which the water droplets are fully immersed in is considered to be in a steady uniform flow on a horizontal plane with no vertical component.

Overall the implications of these assumptions for sprinkler irrigation droplet dynamics are: the initial conditions for droplet motion are established, droplets are treated as rigid spheres with

constant diameter and shape throughout their motion. The dynamics of the complex process of the simultaneous motion of a system of particles (which involves direct interaction between particles and indirect interaction through their effect on the ambient air) can be reduced to the dynamics of an impulsively started motion of individual particles, with known diameters and initial conditions, through a viscous fluid. In which case the (physical) modeling objective reduces to that of determining the landing coordinates of the droplets only and not the volumetric water contents of the individual droplets. The volumetric application rates associated with each droplet is then empirically determined.

The preceding discussion shows that references to, and descriptions of, water droplets in the context of sprinkler irrigation droplet dynamics modeling should not imply actual water droplets stemming from the breakup and disintegration of an irrigation stream. In stead they refer to the “virtual” droplets derived in accordance with the assumptions described above. A question that may then arise is as to how the range of variation of the droplet diameters, used for modeling purposes, and the corresponding radial irrigation application rates can be determined. A concise description of the approach commonly used to determine droplet diameter ranges and associated volumetric application rates in sprinkler irrigation precipitation pattern simulation (e.g., Fukui et al., 1980; von Bernuth and Gilley, 1984; Vories et al., 1987; Seginer et al., 1991; Carrion et al., 2001, Playan et al., 2009) is presented in the following section with a more detailed computational procedure described in Chapter 4.

2.4.1 Precipitation pattern about a sprinkler under no-wind condition

Considering a condition in which all the assumptions listed above are met and where wind velocity is zero (implying symmetrical application rate about a sprinkler), the basics of mechanics suggest that for a given sprinkler and operating condition the trajectories and landing coordinates of individual droplets, referenced from the sprinkler location, are functions of droplet diameter only (Figure 1). With smaller diameter droplets falling close to the sprinkler and larger droplets further out. This implies that, for any given application, the maximum droplet diameter can be directly related to sprinkler wetted diameter, which in turn is a function of sprinkler

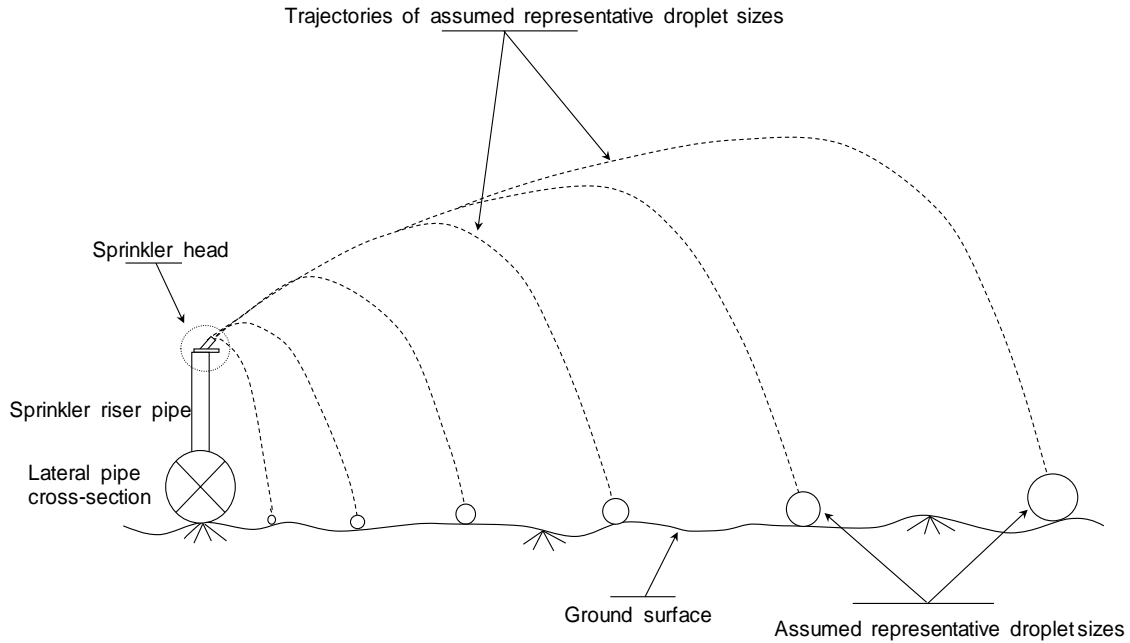


Figure 1. Schematics of the conceptualization of precipitation pattern about a sprinkler for droplet dynamics modeling

model, nozzle size, sprinkler riser height, and operating pressure and can be determined through measurements. The minimum droplet diameters can be determined based on numerical (efficiency and robustness) considerations. The resulting droplet size range can then be discretized into a convenient number of subintervals (droplet diameters), which for the most part is a function of computational time. A droplet dynamics model can then be used to determine the landing coordinates of each droplet size within the predefined range. However, as a direct consequence of the simplifying (limiting) assumptions listed above the volumetric application rates associated with individual droplet diameters, within the preset range, is different from the volumetric water content of the droplet and cannot be computed as part of the numerical solution of the droplet dynamics model. Instead the droplet volumetric application rates are determined by correlating radial water application rates measured under no-wind condition with the landing coordinates of the individual droplets. Hence, the basic notion that underlies the simplified sprinkler irrigation precipitation pattern modeling framework can be stated as: the landing coordinates of a suitably defined range of droplet diameters, computed with a physically based droplet dynamics model, coupled with a semi-empirically determined droplet volumetric

application rate data can be used to approximate irrigation water distribution pattern about a sprinkler or a set of sprinklers with satisfactory accuracy.

Considering a full-circle impact sprinkler (commonly used in solid set sprinkler systems), the water distribution pattern about a sprinkler can be computed by rotating the simulated radial application rate pattern about the sprinkler through 360° at preset angular discretization steps. The resulting application rate pattern about a sprinkler can then be integrated over the irrigation application duration to determine the spatial distribution of irrigation depth. Furthermore, assuming water droplets from different sprinklers do not interfere with each other's motion, water distribution patterns from adjacent sprinklers can be overlapped to compute field-scale irrigation distribution. Sprinkler radial application rate characterization measurements made at a given pressure head can be used for a set of sprinklers in an irrigated field with no significant pressure head variation. Assuming the same sprinkler model and nozzle size are used throughout an irrigated field (which is a common practice), in order to cover the pressure head variation over an irrigated field indoor sprinkler tests may need to be conducted at a couple of different pressure head levels spanning the pressure range in the field.

2.4.2 Precipitation pattern about a sprinkler under field conditions

The application of droplet dynamics models to simulate irrigation water distribution about a sprinkler under no-wind condition does not necessarily bring in new information to that obtained through measurements. However, sprinkler irrigation typically takes place under wind and the application of such a model is more useful in the context of simulating, wind distorted sprinkler irrigation application patterns (or the effects of wind speed and direction on precipitation pattern about a sprinkler). Note that the effect of wind on irrigation precipitation pattern operates at two levels. It distorts the trajectories and landing coordinates of individual droplets (compared to an equivalent no-wind condition) and also it affects the physical processes of liquid jet breakup and droplet size distributions (e.g., Kohl, 1974), by modifying the relative velocity of the water jet with respect to the ambient air. However, given the simplifications that have already been introduced, a rigorous and explicit accounting of these effects within the modeling framework described here for sprinkler applications is unwarranted. Hence, the

established approach for modeling wind effects on precipitation pattern about a sprinkler (Fukui et al., 1980; Vories et al., 1987; Seginer et al., 1991, Carrion et al., 2001) consists of:

(i) For a given sprinkler and nozzle operating pressure, the droplet sizes and associated volumetric application rates are assumed to remain the same as that derived for no-wind condition, and

(ii) The effect of wind on precipitation pattern is taken into account with empirical shape fitting parameters derived based on field measured irrigation water distribution under wind condition.

As will be discussed in subsequent sections, this is the approach used in the model developed in the study reported here. Apparently the predictive capability of such a model is limited. However, such limitations can be overcome if a database of the shape fitting parameters is developed as a function of sprinkler model, nozzle size, sprinkler pressure head range, and average wind speed.

The practical significance of a droplet dynamics model is to afford irrigation engineers with capability to simulate irrigation precipitation pattern about a sprinkler given sprinkler design factors, sprinkler pressure head, and ambient weather condition, mainly wind speed and direction, relative humidity, and temperature. Such a model, coupled with a sprinkler system hydraulic and soil water flow submodels, can eventually be used for field-scale irrigation system design, management, and evaluation. Evidently, sprinkler precipitation pattern simulation is more than droplet dynamics, however, the droplet dynamics modeling functionality forms the physical basis of a sprinkler precipitation pattern simulation model. Hence, much of the effort, as related to problem formulation and numerical solution of sprinkler precipitation pattern simulation model, is directed at developing the droplet dynamics submodel. Subsequent discussion reviews droplet dynamics modeling mainly in the context of sprinkler irrigation and then presents the form of the equation used in the numerical droplet dynamics submodel developed as part of the current study. A more detailed discussion on the theoretical basis and derivation of pertinent equations is presented in an accompanying document (Zerihun and Sanchez, 2014b).

Chapter 3 Sprinkler irrigation droplet dynamics modeling

3.1 Literature review

Early droplet dynamics models, developed in the context of sprinkler and spray applications, did not take into account wind effects on droplet motion, hence aerodynamic drag and gravity were considered as the only forces acting on droplets (Green, 1952; Bilanski and Kidder, 1958; Smith, 1970; and Goering et al., 1972). Some of these models assumed that drag force exerted on the droplet by the ambient air can be expressed as a linear function of droplet relative velocity (Green, 1952; Bilanski and Kidder, 1958). Seginer (1965) evaluated the form of the drag equation as related to the exponent of the droplet velocity vector, based on measured data from Laws (1940), and suggested that an equation that relates drag with the square of the droplet velocity can yield satisfactory results when applied to modeling droplet motion in sprinkler irrigation context. Smith (1970) and Goering et al. (1972) used an equation that relates drag with the square of the droplet velocity vector to model droplet motion, with the effect of evaporation taken into account. These early studies were limited to the formulation of the physics, which govern the motion of a droplet in a quiescent air and, pertinent numerical and analytical solutions.

Droplet dynamics in the context of sprinkler irrigation application concerns the unsteady motion of water droplets through the ambient air, which could be quiescent (no-wind condition) or under steady uniform smooth horizontal motion itself (e.g. Fukui et al., 1980; Vories et al., 1987; Seginer et al., 1991; Carrion et a, 2001; Playan et al., 2009). Individual droplets are considered to be of constant size and shape throughout their motion, hence can be treated as solid spheres as far as their drag characteristic is concerned. Droplet motion is treated as an impulsively started motion at the sprinkler nozzle with known initial condition. The motion is curvilinear on the vertical plane, because of gravity. On the other hand, droplet motion on the horizontal plane is rectilinear, if the ambient air is quiescent or, it can be curvilinear if there is wind.

A sprinkler irrigation droplet dynamics model simulates the motion through the ambient air of individual droplets. The governing equation of droplet dynamics is a mathematical description of Newton's second law of motion (Fukui et al., 1980; von Bernuth and Gilley, 1984;

Seginer, et al., 1991; Carrion, et al., 2001; Playan et al., 2009). The equation of motion relates the net unbalanced force acting on a water droplet, computed as the vector sum of the major forces acting on the droplet, with its acceleration. The resulting set of differential equations can then be solved numerically given the initial velocity and location of the particle (droplet) as it breaks away from the water jet, to determine its trajectory in a selected coordinate system and destination on the irrigated field surface.

A sprinkler irrigation precipitation pattern simulation model, with a droplet dynamics component that solves the equation of motion numerically, was developed by Fukui et al. (1980). The droplet dynamics submodel was developed based on the simplifying assumptions listed in a preceding section and has the following form:

$$\frac{dV_x}{dt} = -\xi C_{ds} |\mathbf{V}_r| (V_x - W_x) \quad (1)$$

$$\frac{dx}{dt} = V_x \quad (2)$$

$$\frac{dV_y}{dt} = -\xi C_{ds} |\mathbf{V}_r| (V_y - W_y) \quad (3)$$

$$\frac{dy}{dt} = V_y \quad (4)$$

$$\frac{dV_z}{dt} = -\xi C_{ds} |\mathbf{V}_r| V_z - g \quad (5)$$

$$\frac{dz}{dt} = V_z \quad (6)$$

Noting that the mass, m (M), and the projected area normal to the direction of motion, A (L^2), of a droplet of diameter d (L) are given as

$$m = \rho_w \frac{\pi}{6} d^3 \quad \text{and} \quad A = \frac{\pi}{4} d^2 \quad (7)$$

in Eqs. 1-6

$$\left. \begin{aligned} \xi &= \frac{3}{4} \left(\frac{\rho}{\rho_w} \right) \left(\frac{1}{d} \right), \quad \mathbf{V}_r = (V_x - W_x)\mathbf{i} + (V_y - W_y)\mathbf{j} + V_z\mathbf{k}, \quad \text{and} \\ \mathbf{W} &= W_x\mathbf{i} + W_y\mathbf{j} \end{aligned} \right\} \quad (8)$$

where $V_x [L/T]$, $V_y [L/T]$, and $V_z [L/T]$ = components of droplet absolute velocity vector, \mathbf{V} , along the three coordinate axes of x , y , and z , respectively; $W_x [L/T]$ and $W_y [L/T]$ = components of the wind velocity vector, \mathbf{W} , along the x and y coordinate axis; $t [T]$ = time; $x [L]$, $y [L]$, and $z [L]$ = coordinates of droplet location in a rectangular coordinate system; C_{ds} = steady state drag coefficient which is a function of the Reynolds number, $Re [-]$; \mathbf{i} , \mathbf{j} , and \mathbf{k} = unit vectors along the x , y and z coordinate axes, respectively; g = gravitational acceleration (L/T^2); ρ_w = density of water [M/L^3]; π = the ratio of the circumference of a circle to its diameter [-]; and ρ = density of the ambient air [M/L^3]. Equations 1-6 represent a coupled system of differential equations with six unknowns (V_x, V_y, V_z, x, y, z), which can be solved numerically after having been coupled with pertinent initial conditions (e.g., Fukui et al., 1980).

Note that in Eqs. 1-6, the forces that are explicitly considered are those of drag, $\mathbf{D} [ML/T^2]$, and droplet weight, $\mathbf{F}_w [ML/T^2]$, expressed as:

$$\mathbf{D} = -C_{ds} A \frac{\rho}{2} |\mathbf{V}_r| \mathbf{V}_r \quad (9)$$

and

$$\mathbf{F}_w = -mg\mathbf{k} \quad (10)$$

The above formulation implicitly assumes that wind effects on droplet motion can be encapsulated in the drag equation, expressed in terms of the droplet relative velocity vector. It can be noted that the equation of droplet dynamics presented above, Eqs. 1-6, is analogous in form to that derived for droplet motion under no-wind condition in the accompanying document. The approach proposed by Fukui et al. (1980), in terms of mathematical formulation of the physical problem and numerical solution, for the most part remained a pattern adopted by subsequent studies. von Bernuth and Gilley (1984) and Vories et al. (1987) developed a sprinkler

irrigation precipitation pattern simulation model with a droplet dynamics submodel, based on a numerical solution of Eqs. 1-6. While Fukui et al.'s model expressed the drag coefficient as a function of the droplet Reynolds number, von Bernuth and Gilley (1984) and Vories et al. (1987) expressed the drag coefficient as a function of the droplet diameter. Seginer et al. (1991) developed a numerical droplet dynamics model based on a solution of the equations of motion, with the form given in Eqs. 1-6. In order to take into account the effect of wind on sprinkler distribution pattern more effectively, Seginer et al. (1991) proposed a correction to the steady state drag coefficient

$$C_{dw} = C_{ds}(1 + k_f |\cos \Theta|) \quad (11)$$

where C_{dw} = corrected drag coefficient under wind condition [-], k_f = empirical fitting parameter [-], and Θ = angle between droplet relative velocity and wind velocity vectors (Figure 2). It can be noted from Eq. 9 that this formulation of the drag coefficient implies that the drag force exerted on the droplet would be the vector sum of two components. A component acting along the line of action of the droplet relative velocity vector and another in a direction collinear to the

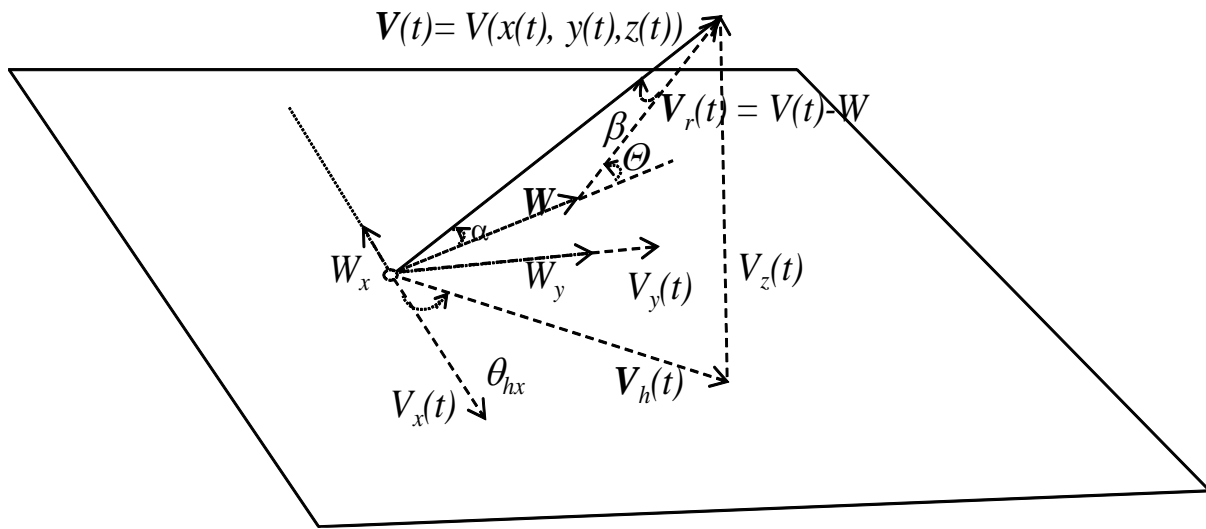


Figure 2 Velocity diagram depicting droplet absolute and relative velocity vectors, and wind velocity vector (where α = angle between wind velocity and droplet absolute velocity vector, β = angle between droplet absolute and relative velocity vectors, and Θ = angle between wind velocity and droplet relative velocity vector)

wind velocity vector. Carrion et al. (2001) and later on Playan et al (2009) published a sprinkler irrigation precipitation pattern simulation model with a droplet dynamics submodel based on a numerical solution of the equation of motion (Eqs. 1-6). They noted that the drag correction factor proposed by Seginer et al. (1991) can represent the effect of wind in the direction parallel to the prevailing wind. However, in order to account for the field observed reduction in sprinkler wetted radius in a direction normal to the prevailing wind satisfactorily, these authors introduced an additional correction to the drag coefficient and gave the following expression for C_{dw} :

$$C_{dw} = C_{ds}(1 + k_{f1} \sin \beta - k_{f2} \cos \Theta) \quad (12)$$

where $k_{f1} [-]$ and $k_{f2} [-]$ = empirical fitting parameters and β = the angle that the absolute velocity vector makes with the relative velocity vector (Figure 2). The numerical solution of the scalar differential equations of motion presented above (Eqs. 1-6) is based on some variant of the Runge-Kutta method (Fukui et al., 1980; Seginer et al., 1991; Carrion et al., 2001; and Playan et al., 2009).

3.2 Equations used in the numerical droplet dynamics model developed in the current study

Derivation of the equations that form the basis of the droplet dynamics model developed here combines established ideas developed in earlier studies and also new concepts formulated as part of the current study (Zerihun and Sanchez, 2014b). Sprinkler irrigation is typically undertaken under wind condition and droplet dynamics under no-wind condition is a special case of that occurring under wind. Hence, the general case of droplet motion under wind is considered here, which is unsteady and curvilinear. A discussion on the forces that the ambient air exerts on a droplet undergoing unsteady motion and the modification that needs to be made to the steady state drag coefficient in order to take into account the aggregate effects of these various forces in the drag equation is described in a companion document. In addition, these authors have also shown that the major forces acting on a droplet undergoing unsteady motion under wind consists of drag, droplet weight, and wind drift force. However, following the approach commonly used in sprinkler irrigation droplet dynamics (Fukui et al., 1980; Vories et al., 1987; Seginer et al., 1991; Carrion et al., 2001, Playan et al., 2009), as an initial approximation wind effects on drag and droplet drift are assumed to be encapsulated in the drag equation, Eq. 9. The expression for

drag is then resolved into a component collinear with the droplet absolute velocity vector, \mathbf{D}' , which represents the effect of wind on the unsteady drag force and a component normal to the droplet absolute velocity vector, \mathbf{F}_{WD}' , which approximates the effect of wind on droplet drift. In acknowledgement of the fact that the equations derived as such are not exact expressions for drag and wind drift forces, they are then multiplied by empirical scale factors. The resulting scalar differential equation describing droplet motion under wind can then be expressed as (Zerihun and Sanchez, 2014b):

$$\frac{dV_x}{dt} = \lambda_1(V_x - W_x) + \lambda_2 V_x \quad (13)$$

$$\frac{dx}{dt} = V_x \quad (14)$$

$$\frac{dV_y}{dt} = \lambda_1(V_y - W_y) + \lambda_2 V_y \quad (15)$$

$$\frac{dy}{dt} = V_y \quad (16)$$

$$\frac{dV_z}{dt} = \lambda_3 V_z - g \quad (17)$$

$$\frac{dz}{dt} = V_z \quad (18)$$

where

$$\lambda_1 = \zeta_2 \psi \psi_4, \quad \lambda_2 = \psi_2 \psi_4 (\zeta_1 - \zeta_2), \quad \text{and} \quad \lambda_3 = \psi_4 (\zeta_1 \psi_2 + \zeta_2 \psi_3) \quad (19)$$

$$\left. \begin{aligned} \psi &= -C_{du} A \frac{\rho}{2} |\mathbf{V}_r|, \quad \psi_1 = -C_{du} A \frac{\rho}{2} \frac{|\mathbf{V}_r|}{|\mathbf{V}|^2}, \\ \psi_2 &= \psi_1 \left(V_x(V_x - W_x) + V_y(V_y - W_y) + V_z^2 \right), \\ \psi_3 &= \psi - \psi_2, \quad \text{and} \quad \mathbf{V} = V_x \mathbf{i} + V_y \mathbf{j} + V_z \mathbf{k} \end{aligned} \right\} \quad (20)$$

ψ_4 = the reciprocal of droplet mass $[1/M]$, ζ_1 (-) and ζ_2 (-) = are scale factors related to wind effects on droplet drag and drift (a more detailed description of which is presented in the accompanying document), and C_{du} = unsteady drag coefficient [-]. An empirical expression for C_{du} is presented later. The average wind speed and wind vector azimuth (a measure of wind direction) for the duration of irrigation or hourly average wind velocity data can be obtained through measurements, based on which the components along the horizontal coordinate axes can be computed.

Equations 13-18 represent a coupled system of (six) ordinary differential equations with six variables, which constitute an initial value problem that can be solved numerically given the initial conditions. Considering the intersection of the centerlines of the lateral and the sprinkler riser pipe as the origin of the coordinate system, applicable initial conditions can be given as:

$$\left. \begin{aligned} x(t=0) &= 0.0, & y(t=0) &= 0.0, & z(t=0) &= z_0 \\ V_x(t=0) &= |V_0| \cos(\theta_{x0}), & V_y(t=0) &= |V_0| \cos(\theta_{y0}) \\ V_z(t=0) &= |V_0| \cos(\theta_{z0}) \end{aligned} \right\} \quad (21)$$

In Eq. 21, z_0 = sprinkler riser pipe height (L), $|V_0|$ = the magnitude of the droplet initial absolute velocity vector (L/T), and θ_{x0} , θ_{y0} , and θ_{z0} = the angles that the droplet initial absolute velocity vector makes with the x , y , and z coordinate axes, respectively.

The droplet initial absolute velocity vector can be computed based on measured pressure head, sprinkler hydraulic characteristics, and nozzle diameter. Considering a counter clockwise sprinkler rotation referenced from the positive x -axis (Figure 2), the sprinkler nozzle angular setting on the horizontal plane, θ_{hx0} , is known. The sprinkler vertical tilt angle, θ (*degree*), is also a known quantity for a given sprinkler model. Then the angles that the initial velocity vector makes with the coordinate axes (θ_{x0} , θ_{y0} , and θ_{z0}) can be computed with

$$\left. \begin{aligned}
&\theta_{x0} = a \cos[\cos(\theta) \cos(\theta_{hx0})], \quad \theta_{y0} = a \cos[\cos(\theta) \sin(\theta_{hx0})] \\
&\text{and} \\
&\theta_{z0} = \frac{\pi}{2} - \theta
\end{aligned} \right\} \quad (22)$$

The preceding discussion assumes that the expression for aerodynamic drag, given in Eq. 9, has the mathematical structure to encapsulate the effects of the major forces acting on the droplet, including wind effects on both drag and droplet drift, and produce the kind of motion resulting from the action of such forces on a droplet in some scaled fashion. Considering the alternative set of equations derived in the accompanying document, the similarity in form of the terms representing droplet drag and wind drift forces lends some support to this observation.

Temkin and Kim (1980) and Temkin and Mehta (1982) proposed an empirical expression for the unsteady drag coefficient, C_{du} , given as the sum of the steady state drag coefficient and a term representing some function of the droplet acceleration number. Their equation was developed based on laboratory experiments covering limited set of conditions in terms of droplet Re , droplet diameter ranges, and air flow velocity compared to those encountered in field sprinkler applications. Hence, its applicability to droplet motion, in the context of sprinkler irrigation modeling, is yet to be determined. In the model developed here the effect of acceleration is taken into account by introducing an empirical drag correction parameter for acceleration effects, ζ_3 (-), in a form given in Eq. 23

$$C_{du} = C_{ds}(Re) + \zeta_3 \quad (23)$$

3.3 Special cases and parameter values

The model parameters defined above, Eqs.13-18, are scale factors for wind effects on drag, ζ_1 , and droplet drift, ζ_2 , and the drag coefficient correction factor for acceleration effects, ζ_3 . These parameters can in theory be estimated through inverse modeling, if all the model inputs including initial conditions and wind velocity vector are known and the complete trajectory of a droplet is given. As described in the derivation of Eqs. 13-18, in the accompanying document,

some physical meaning can be attributed to these parameters when they are used in the context of simulating the motion of a droplet. However, when applied to the simulation of sprinkler irrigation precipitation pattern they represent shape fitting parameters. The range of variation of these parameters is not yet determined. In subsequent sections some tentative ranges, derived based on numerical simulations, will be presented (Section 6.3.2). Here, however, the values that these parameters assume under some special conditions are discussed:

(i) For steady state condition (water droplet relative velocity, V_r , is invariant with time), then the drag correction coefficient for acceleration effects is set at $\zeta_3 = 0.0$. Such a condition implies that the droplet has accelerated to the terminal velocity in the course of its motion.

(ii) For unsteady water droplet motion the parameter $\zeta_3 \neq 0.0$. In theory this should typically be the case in sprinkler droplet dynamics modeling.

(iii) For unsteady, but quiescent ambient air $\zeta_3 \neq 0.0$ and $W_x = W_y = 0.0$. In addition, setting the parameter $\zeta_1 = 1.0$ and $\zeta_2 = 0.0$, reduces Eqs. 13-18 to the form applicable to no-wind condition (Eqs. 22-27, in the accompanying document). Alternatively setting $\zeta_1 = 0.0$, $\zeta_2 = 1.0$, $\psi_2 = 0.0$, and $W_x = W_y = 0$ yields the same form, in the model described here this is the option implemented.

(iv) Considering that the initial conditions for all droplets are the same, it follows that at the sprinkler nozzle droplet kinetic energy per unit volume is also the same for all droplets. However, drag per unit volume increases with a decrease in droplet diameter, because of the associated increase in droplet specific surface area, which affects the empirically determined steady state drag coefficient. This implies that the initial kinetic energy of finer droplets can be dissipated by a relatively larger drag to such an extent that the horizontal component of the droplet absolute velocity vector becomes nearly zero at relatively short distances from the sprinkler. When this occurs under wind, one option is to assume a zero horizontal droplet velocity thereafter (e.g., Playan et al., 2009). An alternative approach used by Thompson et al. (1993a,1993b) and implemented in the computational framework of the model described here

(Section 3.5) assumes that the droplet is fully carried by the ambient air. In which case the direction of droplet motion is reversed and droplet assumes a horizontal velocity equal to the wind velocity. In such a scenario, $V_x = W_x$, $V_y = W_y$, and the parameters, ζ_2 , is set to 1.0.

3.4 Numerical solution

The system of equations describing sprinkler droplet dynamics for conditions involving unsteady droplet motion through the ambient air (Eqs. 13-18 and 20) represents an initial value problem. This system of equations can be solved numerically. Computation begins at the lower limit of the interval, over which the function is defined, based on known values of the function there and advances with time over suitably selected time steps, which could be constant or variable. For each subsequent step an approximation of the function is computed based on the solution from the preceding time step or steps. The process is repeated until the domain of the function is covered. The basic idea consists of assuming the numerical error introduced at each step is sufficiently small and remains bounded as the solution advances with time; the numerical solution yields an approximation that is sufficiently close to the exact/analytical solution. Although numerical errors have both rounding off and truncation error (resulting from numerical approximation of exact solutions) components, the rounding off errors are properties of the computing machine, hence are given. Thus the effort in improving accuracy of numerical approximations is mainly aimed at reducing the local truncation error. An array of numerical methods is available for solving initial value problems, which differ in the level of accuracy as well as numerical efficiency and robustness. The methods are described as single step (in which case an approximation of the function at any given time step is computed as a function of its value from the immediately preceding time step only) or multistep methods (where numerical approximations of the function computed in more than one of the preceding steps are used to compute the new value of the function). These methods can also be described as explicit or implicit, depending on whether the unknown function can be expressed as an explicit function of the already computed function values (explicit) or the functions have an implicit form and need to be evaluated through the solution of a coupled system of nonlinear equations (implicit). Explicit methods are relatively simpler than implicit methods, but have time step size restrictions. Subsequent discussion is limited to explicit numerical solution techniques.

A description of some of the well known single step and multistep explicit methods for a numerical solution of initial value problems is widely available in the literature (e.g., Mathews and Fink, 2004; Burden et al., 1981; and Dormand, 1996). Single step methods are relatively simpler, although less accurate and efficient compared to multistep methods (Mathews and Fink, 1999; Burden et al., 1981). However, some variations of the most widely used class of single step methods, higher order Runge-Kutta methods, can be robust, easy to implement, and of reasonable accuracy (Mathews and Fink, 2004; Dormand, 1996). In addition, single step methods have the advantage of being self-starting as opposed to the multistep methods which often use single step methods to initiate a numerical computation. In the current study, an explicit Runge-Kutta method is used to solve the initial value problem (Eqs. 13-18 and 20). Runge-Kutta methods were used to solve the equations of sprinkler droplet dynamics (Fukui et al., 1980; Vories et al., 1987; 1980; Seginer, et al., 1991, Carrion et al., 2001; Playan et al., 2009). In subsequent discussion, a brief description of the Runge–Kutta method and the basic principle on which it is based is presented. In order to simplify the presentation, first an initial value problem consisting of a single equation will be considered, and then the results will be generalized for a system of equations. Based on which the specific Runge-Kutta method used to solve the system of equations given in Eqs. 13-18 and 20 and the associated error measures will be described.

3.4.1 Runge-Kutta method, a review

Description: Consider an initial value problem of the form

$$\phi'(t) = f(t, \phi), \quad t \in [a, b], \quad \text{and} \quad \phi(a) = \phi_0 \quad (24)$$

where $\phi'(t)$ = the derivative of ϕ with respect to t ; ϕ = dependent variable of the function $\phi(t)$; t = independent variable of the function, $\phi(t)$, which is time here; $f(t, \phi)$ = some function of t and ϕ , which represents the slope of the function $\phi(t)$; a and b = real numbers representing the upper and lower limits, respectively, of the interval over which the function $\phi(t)$ is defined; ϕ_0 = the initial condition. Numerical approximation of the solution to this problem, at some point, t_{k+1} , in the interval $[a, b]$, with the Rung-Kutta method can be given as

$$\phi_{k+1} = \phi_k + \sum_{i=1}^I c_i \sigma_i \quad (25)$$

where

$$\sigma_i = hf(t + d_i h, \phi_k + \sum_{j=1}^{i-1} e_{ij} \sigma_j) \quad (26)$$

In Eqs. 25 and 26, ϕ_k = the numerical approximation of $\phi(t_k)$; $\phi(t_k)$ = exact value of ϕ at $t = t_k$; h = time step size ($t_{k+1} - t_k$); k = time step and data point index (0,1,2,...); c_i , d_i , and e_{ij} = are constant coefficients (parameters), that vary with the particular Runge-Kutta method; i = stage index; I = number of stages; and j = an index that vary between 1 and $i-1$, for the i th stage. In subsequent discussion, the term function will be used to refer to, $\phi(t)$, and $f(t, \phi)$ will be referenced as the slope function. For explicit Runge-Kutta methods $e_{ij} = 0$ for $i \leq j$ and the so called row sum condition states that for a given stage $d_i = \sum_{j=1}^{i-1} e_{ij}$ (Dormand, 1996), from which it

follows that for an explicit Runge-Kutta method $d_1 = 0$. The function σ_i , Eq. 26, for $i=1$ to $i=I$ can then be expressed as

$$\sigma_1 = hf(t_k, \phi_k) \quad (27)$$

$$\sigma_2 = hf(t_k + d_2 h, \phi_k + e_{2,1} \sigma_1) \quad (28)$$

$$\sigma_3 = hf(t_k + d_3 h, \phi_k + e_{3,1} \sigma_1 + e_{3,2} \sigma_2) \quad (29)$$

• • •
• • •

$$\sigma_I = hf(t_k + d_I h, \phi_k + e_{I,1} \sigma_1 + e_{I,2} \sigma_2 + e_{I,3} \sigma_3 + \dots + e_{I,(I-1)} \sigma_{(I-1)}) \quad (30)$$

Considering that the coefficient in Eq. 25 should meet the consistency condition $\sum_{i=1}^I c_i = 1$

(Dormand, 1996), it then follows that the summation term in Eq. 25 represents a linear combination of the slope functions (Eqs. 27-30) evaluated at suitably selected points over a time step. The number of those points and their location within a time step is a function of the number of stages and the parameters set. It then remains to determine the appropriate number of stages, I , and parameter combinations (c_i , d_i , and e_{ij}), in order to obtain a numerical approximation of the

function, ϕ , with a Runge-Kutta method of a certain accuracy. An array of explicit Runge-Kutta approximations exists with different levels of accuracy and robustness (Stroud, 1974; Dormand, 1996).

Taylor series approximations and Runge-Kutta methods: As is the case with many numerical techniques, the Runge-Kutta method as well is based on Taylor series expansion (Mathewes and Fink, 2004; Burden, 1981; Dormand, 1996). The basic idea of Taylor series approximation is that if a function, $\phi(t)$, is differentiable to any desired order within an interval $[a,b]$; then given the function value at some point in the interval, $\phi(t_k)$, its value at another point within the interval, $\phi(t_{k+1})$, can be approximated to a desired level of accuracy with the Taylor series, provided the step size, h , is sufficiently small. The Taylor series expansion of the function $\phi(t)$ about t_k is given as

$$\phi_{k+1} = \phi(t_k) + h\phi'_k + \frac{h^2}{2}\phi''_k + \frac{h^3}{6}\phi'''_k + \dots + \frac{h^n}{n!}\phi_k^{(n)} + \frac{h^{(n+1)}}{(n+1)!}\phi_k^{(n+1)} + \dots \quad (31)$$

where $\phi_k^{(n)}$ = the n th derivative of the function evaluated at $t = t_k$ and $n!$ = the factorial of n . Provided the conditions described above are met, the accuracy of the Taylor method increases with the number of terms retained in the approximating power series. Noting that $\phi'_k = f(t_k, \phi_k)$ (Eq. 24), the n th order Taylor series approximation to $\phi(t_{k+1})$, ϕ_{k+1} , can be given as:

$$\begin{aligned} \phi_{k+1} = \phi(t_k) + hf(t_k, \phi_k) + \frac{h^2}{2}f'(t_k, \phi_k) + \frac{h^3}{6}f''(t_k, \phi_k) + \dots \\ + \frac{h^n}{n!}f^{(n-1)}(t_k, \phi_k) + O(h^{(n+1)}) \end{aligned} \quad (32)$$

In Eq. 32 the term $O(h^{n+1})$ represents the approximation error inherent in a Taylor method of order n , due to the truncation of terms of order $n+1$ and greater. Although an estimate of the global error over the entire interval of integration $[a,b]$, Eq. 24) is desirable, in numerical computation a practically more useful quantity is the error from each time step. Hence, the approach commonly used is to make sure that the error from each step, the local truncation error, is small and remains small (bounded) as the solution advances ϕ with time. Note that during each time step of a numerical computation, ϕ_{k+1} is computed based on ϕ_k , which is only a numerical

approximation to $\phi(t_k)$. In which case the error term in Eq. 32, $O(h^{(n+1)})$, is not the same as the local truncation error, hence in subsequent discussions it is referred to as the local error instead of the local truncation error. Although the Taylor method is powerful, it is not often used in practice because of the requirement to compute and evaluate derivatives. Instead practically more useful methods like the Runge-Kutta, which do not require computation and evaluation of derivatives, are developed based on the Taylor series method.

The format of the Runge-Kutta method applied to the solution of an initial value problem consisting of a single differential equation is presented above in Eqs. 25 and 26. The basic idea of deriving a Runge-Kutta approximation of a given order consists of first expanding the right hand side of Eq. 25 with a Taylor method of an appropriate order about the point (t_k, ϕ_k) , which yields an expression for ϕ_{k+1} in terms of $f(t, \phi)$, its derivatives, h , and the coefficients of Eqs. 25 and 26. Then by matching the resulting expression with Eq. 32 (which is a Taylor series approximation to $\phi(t_{k+1})$, ϕ_{k+1} , of an appropriate order, obtained by expanding the function $\phi(t)$ about t_k) a system of equations relating the Runge-Kutta parameters (often termed as equations of condition) can be derived (Stroud, 1974; Cartwright and Piro, 1992). The solution of these equations (i.e., computation of the parameters) results in a Runge-Kutta approximation of the required order. It should be noted that a Runge-Kutta approximation of a given order is nonunique. However, some forms are practically more useful and hence commonly described in literature

The derivation of the equations of condition and the computation of Runge-Kutta parameters for a second order approximation is relatively straight forward and is widely available (e.g., Mathewes and Fink, 2004; Burden et al., 1981), however, for higher order Runge-Kutta methods the algebra is too involved hence its presentation is limited to advanced literature, a concise description of the equations of condition and solution leading to a widely used form of the fourth order Runge-Kutta method is presented by Mathewes and Fink (2004). For many of the practically useful Runge-Kutta approximations the number of stages and corresponding parameter sets are computed and tabulated by experts and are widely available in the literature (Mathewes and Fink, 2004; Dormand, 1996; Burden et al., 1981; Stroud, 1974). The order of approximation of a Runge-Kutta formula is related to the number of stages, which in turn determines the number of function evaluations, and hence to a certain extent

computational efficiency of the method as well. For a n th order explicit Runge-Kutta method with $n \leq 4$, the minimum number of stages required is equal to the order of approximation of the Runge-Kutta method (Cartwright and Piro, 1992), however, for higher order methods the order of approximation is less than the minimum required number of stages. Perhaps partly because of this feature the fourth order Runge-Kutta methods are more commonly used in practice (Press et al., 1997).

The main limitation in the Runge-Kutta method has been that it does not have an inherent local error estimation capability. The commonly used approach at error estimation and control is based on a comparison of two different Runge-Kutta estimates of the function over a time step. An earlier method consist of what is described as the step doubling approach, in which two function values computed by taking one full step and two half steps, within a given time steps size, are compared to produce a measure of the numerical error. However, the approach, for instance applied to a commonly used fourth order Runge-Kutta method, requires eleven stages as opposed to the four stages discussed above, hence computationally inefficient. A commonly used and more efficient alternative is the so called embedded Runge-Kutta formulas, in which Runge-Kutta formulas of two different orders can be obtained based on the same (slope) function evaluations (Press et al., 1997). Then the difference between the two approximations is used as a measure of the local error. Another feature of these methods is that within the framework of error estimation, they have the capability to provide an estimate of the optimal time step size, to be used in subsequent computation, taking into account function local behavior. Hence such a method uses variable step sizes and is also referred to as adaptive step-size method.

3.4.2 Adaptive step-size Runge -Kutta methods

Description: Among the widely described adaptive step size Runge-Kutta methods is those involving fourth-fifth order pair, discussed for instance by Press et al. (1997), Mathews and Fink (2004) and Burden et al. (1981). These particular approximations involve a fifth order Runge-Kutta formula with six function evaluations, where some combination of the six functions yields a fourth order (Press et al., 1997). The resulting Runge-Kutta pairs as applied to the numerical solution of Eq. 24, over the $(k+1)$ th time step, can be given as

$$\phi_{k+1} = \phi_k + \sum_{i=1}^6 c_i \sigma_i + O(h^6) \quad (33)$$

for the fifth order approximation, in which the local error, ε , is shown to be of order h^6 ($\propto h^6$), and

$$\phi_{k+1}^* = \phi_k + \sum_{i=1}^6 c_i^* \sigma_i + O(h^5) \quad (34)$$

for the fourth order approximation, where $\varepsilon \propto h^5$. In Eqs. 33 and 34, ϕ_{k+1} and ϕ_{k+1}^* = fifth order and fourth order function approximations, respectively, for the $(k+1)$ th time step, h = the time step size, and c_i and c_i^* = parameters of the fifth and fourth order formulas, respectively. The expressions for the functions, σ_i for $i = 1$ to 6 , is the same as that given in Eqs. 26-30. Note that estimates of the parameters d_i and e_{ij} (Eqs. 25 and 26) are the same for both Runge-Kutta approximations (Eq. 33 and 34).

Error and step size estimation and control: From the preceding discussion it can be noted that an estimate of the local error, δ , over the $(k+1)$ th time step can then be expressed as

$$\delta = \phi_{n+1} - \phi_{n+1}^* \quad (35)$$

It follows from the acceptance of a fourth order Runge-Kutta approximation that $O(h^6) \ll O(h^5)$ and hence $\delta \propto h^5$, then the error level over the current time step size is

$$\delta = \lambda h^5 \quad (36)$$

where λ = a constant. Although the step size, h , can in principle be kept constant, as described above an efficient method need to use variable steps in accord with local function behavior. If a local error tolerance, δ_t , is specified, then an equation of the form given in Eq. 36 can be used to relate δ_t with an approximation of the step size if the error level were to be exactly equal to δ_t , h_t . Combining the resulting expression for δ_t with Eq. 36 and rearranging yields an expression for h_t

$$h_t = h \left(\frac{\delta_t}{\delta} \right)^{0.2} \quad (37)$$

Equation 37 shows that if the ratio in the parenthesis exceeds 1.0, then the error level for the current time step is within the specified tolerance. Hence solution is acceptable. Furthermore, the

h_t value computed as such would be greater than the current time step size, h , which is an indication of the fact that the local function behavior is such that a larger time step size can be taken without exceeding the local error tolerance. In which case h_t can then be used as an approximation of the time step size. On the other hand, if the ratio on the right hand side is less than 1.0, it suggests that the error level exceeds the tolerance, hence solution is not acceptable. Once more h_t , which in this case is less than h , provides an approximation of the step size with which the numerical computation for the current time step needs to be repeated. However, the implementation of a procedure that uses variable step sizes implies that the error tolerance, δ_i , should also be variable as a function of step size, in order to keep the overall (global) error sufficiently small. An alternative is to scale δ_i by the current time step size, $h\delta_i$, which results in a more stringent local error and step size control criteria. It should then be evident that when the expression $h\delta_i$ is substituted, in Eq. 37, for δ_i ; the local error is no longer order five, hence the exponent 0.2 may not be exactly correct. However, Press et al., (1997) suggested the following practical modification to Eq. 37, which results in a more conservative estimate of the time step size

$$\left. \begin{aligned}
 h_t &= hS \left(\frac{h\delta_t}{\delta} \right)^{0.2} && \text{for } \delta \leq h\delta_t \\
 \text{or} &&& \\
 h_t &= hS \left(\frac{h\delta_t}{\delta} \right)^{0.25} && \text{for } \delta > h\delta_t
 \end{aligned} \right\} \quad (38)$$

where S = a safety factor which is sufficiently close to, but less than 1.0. As described in the preceding paragraph, at any given time step Eq. 38 can be used for time step size and error control for a fifth order Runge-Kutta method with an embedded fourth order. In the following section the application of the method, described above, to a system of equations of the form given in Eq. 13-18 and Eq. 21 is presented.

3.4.3 Applications to the solution of a system of equations

Problem description and numerical solution with an adaptive step size Runge-Kutta method:

A generalization of the application of a fourth order Runge-Kutta method to a system of first order ordinary differential equations is presented by Mathewes and Fink (1999) and Burden et al. (1981) and is adopted here for the Runge-Kutta fifth-fourth order pair described above. Using vector notations the initial value problem given in Eqs. 13-18 and 20 can be expressed as

$$\phi' = f, \quad 0 \leq t, \quad \text{and} \quad \phi(t=0) = \phi_0 \quad (39)$$

where

$$\phi' = \begin{pmatrix} \frac{dV_x}{dt} \\ \frac{dx}{dt} \\ \frac{dV_y}{dt} \\ \frac{dy}{dt} \\ \frac{dV_z}{dt} \\ \frac{dz}{dt} \end{pmatrix}, \quad f = \begin{pmatrix} f_1 \\ f_2 \\ f_3 \\ f_4 \\ f_5 \\ f_6 \end{pmatrix}, \quad \phi = \begin{pmatrix} V_x \\ x \\ V_y \\ y \\ V_z \\ z \end{pmatrix}, \quad \text{and} \quad \phi_0 = \begin{pmatrix} V_{x0} \\ x_0 \\ V_{y0} \\ y_0 \\ V_{z0} \\ z_0 \end{pmatrix}, \quad (40)$$

In Eq. 40, f_1, f_2, \dots, f_6 = the right hand side expressions in Eqs. 13-18, respectively, and can be given as:

$$\left. \begin{aligned} f_1 &= \lambda_1(V_x - W_x) + \lambda_2 V_x, & f_2 &= V_x, & f_3 &= \lambda_1(V_y - W_y) + \lambda_2 V_y, \\ f_4 &= V_y, & f_5 &= \lambda_3 V_z - g, & \text{and } f_6 &= V_z \end{aligned} \right\} \quad (41)$$

and it can be noted from Eq. 40 that the elements of ϕ_0 are the quantities defined in Eq 20. The explicit fifth order Runge-Kutta approximation of the solution to Eq. 39, for the $(k+1)th$ time level, can then be expressed in vector form as

$$\phi_{k+1} = \phi_k + F \quad (42)$$

and the corresponding embedded fourth order approximation is given as

$$\phi_{k+1}^* = \phi_k + F^* \quad (43)$$

where ϕ_{k+1} and ϕ_{k+1}^* = vectors of the fifth and fourth order approximations, respectively, of $\phi(t_{k+1})$; ϕ_k = a vector of the fifth order approximation to $\phi(t_k)$, Eq. 44. This implies that although the error is applicable to the fourth order approximation, the fifth order approximation is accepted as the solution for the $(k+1)th$ time step (Press et al., 1997). In Eqs. 42 and 43, F and F^* = vectors whose elements are

$$\phi_k = \begin{pmatrix} V_x \\ x \\ V_y \\ y \\ V_z \\ z \end{pmatrix}_k, \quad F = \begin{pmatrix} F_1 \\ F_2 \\ \cdot \\ \cdot \\ \cdot \\ F_6 \end{pmatrix}, \quad \text{and } F^* = \begin{pmatrix} F_1^* \\ F_2^* \\ \cdot \\ \cdot \\ \cdot \\ F_6^* \end{pmatrix} \quad (44)$$

In Eq. 44, the elements of the vectors F , (F_1, F_2, \dots, F_6) , and F^* , $(F_1^*, F_2^*, \dots, F_6^*)$, have the following form

$$F_p = \sum_{i=1}^6 c_i \sigma_{p,i} \quad \text{for } p = 1, 2, \dots, 6 \quad (45)$$

and

$$F_p^* = \sum_{i=1}^6 c_i^* \sigma_{p,i} \quad \text{for } p = 1, 2, \dots, 6 \quad (46)$$

In Eqs. 45 and 46, p = index of the differential equations (Eqs. 13-18), the sequence in which the index is used to identify the differential equations is given in Eq. 41. Noting that the number of stages for the Runge-Kutta fourth-fifth order pair is six, in Eqs. 45 and 46 I is set equal to 6.

At the i th stage, the $\sigma_{p,i}$ function (Eqs. 45 and 46) is given as

$$\sigma_{p,i} = h_{k+1} f_p(t_k + d_i h_{k+1}, A_i) \quad (47)$$

where h_{k+1} is the $(k+1)$ th time step size, Δ_i is a row vector whose elements are of the following form

$$\Delta_i = (\Delta_{q=1,i}, \Delta_{q=2,i}, \dots, \Delta_{q=6,i}) \quad (48)$$

where

$$\Delta_{q,i} = \phi_{k,q} + \sum_{j=1}^{i-1} e_{ij} \sigma_{q,j} \quad \text{for } q = 1, 2, \dots, 6 \quad (49)$$

where $\phi_{k,q}$ = value of the q th element of the vector ϕ_k (Eq. 44), and c_i , c_i^* , d_i , and e_{ij} are parameters of the Runge-Kutta fourth-fifth pair. In Eq. 47, $d_1 = 0$ and from Eq. 49 it can be noted that $\Delta_{q,1} = \phi_{k,q}$ for $q = 1$ to 6 ; in which case $\Delta_1 = (\phi_{k,1}, \phi_{k,2}, \dots, \phi_{k,6})$. Based on which the expression for $\sigma_{p,i}$, in Eq. 47, for $i = 1$ to 6 can be given as:

$$\sigma_{p,1} = h_{k+1} f_p(t_k, \phi_{k,1}, \phi_{k,2}, \phi_{k,3}, \phi_{k,4}, \phi_{k,5}, \phi_{k,6}) \quad \text{for } p = 1, 2, \dots, 6 \quad (50)$$

$$\left. \begin{aligned} \sigma_{p,2} = h_{k+1} f_p \left(\begin{array}{l} t_k + d_2 h_{k+1}, \phi_{k,1} + e_{21} \sigma_{1,1}, \phi_{k,2} + e_{21} \sigma_{2,1}, \phi_{k,3} + e_{21} \sigma_{3,1}, \\ \phi_{k,4} + e_{21} \sigma_{4,1}, \phi_{k,5} + e_{21} \sigma_{5,1}, \phi_{k,6} + e_{21} \sigma_{6,1} \end{array} \right) \\ \text{for } p = 1, 2, \dots, 6 \end{aligned} \right\} \quad (51)$$

$$\left. \begin{aligned} \sigma_{p,3} = h_{k+1} f_p \left(\begin{array}{l} t_k + d_3 h_{k+1}, \phi_{k,1} + e_{31} \sigma_{1,1} + e_{32} \sigma_{1,2}, \phi_{k,2} + e_{31} \sigma_{2,1} + e_{32} \sigma_{2,2}, \\ \phi_{k,3} + e_{31} \sigma_{3,1} + e_{32} \sigma_{3,2}, \phi_{k,4} + e_{31} \sigma_{4,1} + e_{3,2} \sigma_{4,2}, \\ \phi_{k,5} + e_{3,1} \sigma_{5,1} + e_{3,2} \sigma_{5,2}, \phi_{k,6} + e_{3,1} \sigma_{6,1} + e_{3,2} \sigma_{6,2} \end{array} \right) \\ \text{for } p = 1, 2, \dots, 6 \end{aligned} \right\} \quad (52)$$

• • •
• • •

$$\sigma_{p,6} = h_{k+1} f_p \left. \begin{array}{l} t_k + d_6 h_{k+1}, \phi_{k,1} + e_{6,1}\sigma_{1,1} + e_{6,2}\sigma_{1,2} + e_{6,3}\sigma_{1,3} + e_{6,4}\sigma_{1,4} \\ + e_{6,5}\sigma_{1,5}, \phi_{k,2} + e_{6,1}\sigma_{2,1} + e_{6,2}\sigma_{2,2} + e_{6,3}\sigma_{2,3} + e_{6,4}\sigma_{2,4} \\ + e_{6,5}\sigma_{2,5}, \phi_{k,3} + e_{6,1}\sigma_{3,1} + e_{6,2}\sigma_{3,2} + e_{6,3}\sigma_{3,3} + e_{6,4}\sigma_{3,4} \\ + e_{6,5}\sigma_{3,5}, \phi_{k,4} + e_{6,1}\sigma_{4,1} + e_{6,2}\sigma_{4,2} + e_{6,3}\sigma_{4,3} + e_{6,4}\sigma_{4,4} \\ + e_{6,5}\sigma_{4,5}, \phi_{k,5} + e_{6,1}\sigma_{5,1} + e_{6,2}\sigma_{5,2} + e_{6,3}\sigma_{5,3} + e_{3,4}\sigma_{5,4} \\ + e_{6,5}\sigma_{5,5}, \phi_{k,6} + e_{6,1}\sigma_{6,1} + e_{6,2}\sigma_{6,2} + e_{6,3}\sigma_{6,3} + e_{3,4}\sigma_{6,4} \\ + e_{6,5}\sigma_{6,5} \end{array} \right\} \quad (53)$$

for $p = 1, 2, \dots, 6$

Note that while the right hand side of Eqs. 47 and Eqs. 50-53 are more general and compact expressions, it is evident from Eqs. 13-18 only some of the ϕ 's are pertinent for any given function. Noting that $\phi_{k,1} = V_{xk}$; $\phi_{k,2} = x_k$; $\phi_{k,3} = V_{yk}$; $\phi_{k,4} = y_k$; $\phi_{k,5} = V_{zk}$ and $\phi_{k,6} = z_k$ and recognizing that for $p = 1, 3$, and 5 only $\phi_{k,1}$, $\phi_{k,3}$, and $\phi_{k,5}$ and for $p = 2$ only $\phi_{k,1}$, for $p = 4$ only $\phi_{k,3}$, and for $p = 6$ only $\phi_{k,5}$ are the pertinent variables in computing $\sigma_{p,i}$; equations 50 – 53 can be expressed in terms of the variables of Eqs.13-18. For instance for $i = 1$, the functions $\sigma_{p,1}$ can be given as

$$\left. \begin{array}{l} \sigma_{1,1} = h_{k+1} f_1(V_{xk}, V_{yk}, V_{zk}), \quad \sigma_{2,1} = h_{k+1} f_2(V_{xk}), \\ \sigma_{3,1} = h_{k+1} f_3(V_{xk}, V_{yk}, V_{zk}), \quad \sigma_{4,1} = h_{k+1} f_4(V_{yk}), \\ \sigma_{5,1} = h_{k+1} f_5(V_{xk}, V_{yk}, V_{zk}), \quad \text{and} \quad \sigma_{6,1} = h_{k+1} f_6(V_{zk}) \end{array} \right\} \quad (54)$$

The expressions for $\sigma_{p,2}$ can be obtained in terms of the functions given in Eq. 54, in accordance with Eq. 51, which can then be substituted in Eq. 52 to derive $\sigma_{p,3}$, and the recursive processes is repeated till $i = I$. Once the functions $\sigma_{p,i}$ for each p and i are computed per Eqs. 50-53, they can then be substituted in Eqs. 45 and 46 and the results can then be used to compute the fifth and fourth order approximations to $\phi(t_{k+1})$ with Eqs. 42 and 43. Based on which the error vector can be computed. The error estimation and step size control approach implemented in the model described here is presented in the following section.

As mentioned above the constant parameters, c_i , c_i^* , d_i , and e_{ij} , are derived based on Taylor series approximation of the appropriate order. Although the resulting parameter set for a Runge-Kutta approximation of a given order are not unique, some result in a more efficient numerical approximations and better behaved error properties. The fourth-fifth order Runge-Kutta pair used in the solution of the system of equations describing sprinkler droplet dynamics (Eqs. 13-18) are those described by Press et al. (1997) and pertinent parameters for the Runge-Kutta pair are given in Table 1.

Table 1 Parameters of the fifth order Runge-Kutta formula with an embedded fourth order approximation

$i =$	d_i	e_{ij}					c_i	c_i^*
1	0						$\frac{37}{378}$	$\frac{2825}{276488}$
2	$\frac{1}{5}$	$\frac{1}{5}$					0	0
3	$\frac{3}{10}$	$\frac{3}{40}$	$\frac{9}{40}$				$\frac{250}{621}$	$\frac{18575}{48384}$
4	$\frac{3}{5}$	$\frac{3}{10}$	$-\frac{9}{10}$	$\frac{6}{5}$			$\frac{125}{594}$	$\frac{13525}{55296}$
5	1	$-\frac{11}{54}$	$\frac{5}{2}$	$-\frac{70}{27}$	$-\frac{35}{27}$	0	$\frac{277}{14336}$	
6	$\frac{7}{8}$	$\frac{1631}{55296}$	$\frac{175}{512}$	$\frac{575}{13824}$	$\frac{44275}{110592}$	$\frac{253}{4096}$	$\frac{512}{1771}$	$\frac{1}{4}$
	$j =$	1	2	3	4	5		

Note that the parameters are given in fractions rather than being approximated with decimals in order to minimize computer rounding-off errors

Error estimation and step size control: Using vector notation the estimate of local error levels, δ , for the n th time level can be given as

$$\delta = \phi_{k+1} - \phi_{k+1}^* \quad (55)$$

In principle the error tolerance level for each function should be different so as to take into account scale differences, in which case it should also be expressed as a vector (Eq. 55).

However, in the current application the velocity and distance variables in Eqs. 13-18 are of the same order of magnitude, hence it is deemed that a single value of error tolerance, δ , would be sufficient for use in step size and local error control. In the model described here, the most

limiting (i.e., the largest) of the error estimates, δ_t , among those computed with Eq. 55 along with the preset error tolerance level, δ_t , is used to determine the acceptability of the numerical solution for the current time step and to compute the step size estimate for the subsequent time step with equations of the form given in Eq. 38:

$$\left. \begin{aligned} h_t &= h_{k+1} 0.84 \left(\frac{h_{k+1} \delta_t}{\delta_t} \right)^{0.2} & \text{for } \delta \leq h \delta_t \\ \text{or} & \\ h_t &= h_{k+1} 0.84 \left(\frac{h_{k+1} \delta_t}{\delta_t} \right)^{0.25} & \text{for } \delta > h \delta_t \end{aligned} \right\} \quad (56)$$

Note that based on literature data (e.g., Burden et al., 1981), in the model described here the safety factor, S , is set to 0.84. In order to avoid numerical problems associated with a large change in time step size (e.g., Dormann, 1996), the following constraint is imposed on the range of variations of h_t as a function of h_{k+1} : $h_t \in [0.1h_{k+1}, 10.0h_{k+1}]$. In the model described here the time step size is set to vary in the range $0.00005s$ to $0.1s$, the initial time step size, h_1 , is set equal to $0.001s$, and the error tolerance, δ_t , is set equal to 0.0025 . This implies that the allowable error at any given time step, say at the $(k+1)th$ time step, $h_{k+1} \delta_t$, vary in the range: 1.25×10^{-7} to 2.5×10^{-6} .

The sprinkler precipitation distribution pattern simulation model described here is based on a numerical solution of the dynamics of motion of tens of thousands of droplets ranging in diameter from sub-millimeter (about 0.2mm) scale to a few millimeters, each of which are undertaken over total number of time steps ranging from a few hundreds to a few thousands. This requires balancing the requirements of numerical accuracy with the need for having a robust model. In the model presented here this was accomplished as follows. First during the simulation of the motion of a droplet of a given diameter, if the error tolerance requirement is not met in a specified number of iterations the error tolerance is relaxed so long as the number of time steps that did not meet the requirement is within a preset percentage of the total number of time steps used in the simulation. Since time steps are variable and also the total time that a droplet, of a given diameter under a given set of conditions, requires to travel from the sprinkler nozzle to the field surface are unknowns, the number of time steps as well are not known a priori. However,

experience with the numerical solutions conducted with the model described here shows that the average time step size required for successful simulation decreases with the droplet size. Typically droplets with diameters in the order of one-fifth of a millimeter require a few thousand time steps, while those droplets with diameters in the order of a millimeter or larger require an order of magnitude lower number of time steps. Hence, in the model described here the number of time steps over which the error tolerance can be relaxed is internally set based on droplet diameters, in such a way that on average they remain approximately within 1.5% of the total number of time steps. In addition, the simulation of sprinkler precipitation distribution pattern requires simulating the dynamics of tens of thousands of droplets, in which case a few of the simulations would likely be incomplete. Discarding an entire simulation, because of a few incomplete simulations would severely restrict the robustness of the model. Hence, in the current model the requirement is that a solution is accepted if 0.1% of the total number of simulations (of droplet motion) is incomplete and if the number of unsuccessful consecutive simulations does not exceed five. When the simulation of the motion of a droplet is incomplete, its destination on the field surface is set to that of a preceding droplet whose motion is successfully simulated.

3.5 Flow chart and computational procedure

A simplified flow chart of the droplet dynamics component of the sprinkler precipitation pattern simulation model is presented in Figure 3. Considering the $(k+1)th$ time step and the i th stage, the first phase of computation concerns the determination of the elements of the row vector, Δ_i , with Eq. 49. It is then followed by the calculation of the slope functions $\sigma_{p,i}$ (for $p = 1$ through 6), with Eq.47. These steps are repeated for stages $i = 1$ through 6. Based on which the fifth and fourth order approximations to $\phi(t_{k+1})$, the associated local error estimate, and the adjusted step size are computed. If the computed local error exceeds the error tolerance, solution is unacceptable, hence a revised approximation to $\phi(t_{k+1})$ is computed based on the adjusted step size. On the other hand, if the computed local error is less than the error tolerance, then the fifth order approximation vector is accepted and the solution advances to the next time step. The same process is then repeated till the water droplet reaches the field surface. The following is a summary of the computational steps involved (given the initial conditions, droplet diameter, and error tolerance along with other pertinent data, presented in Section 6.1).

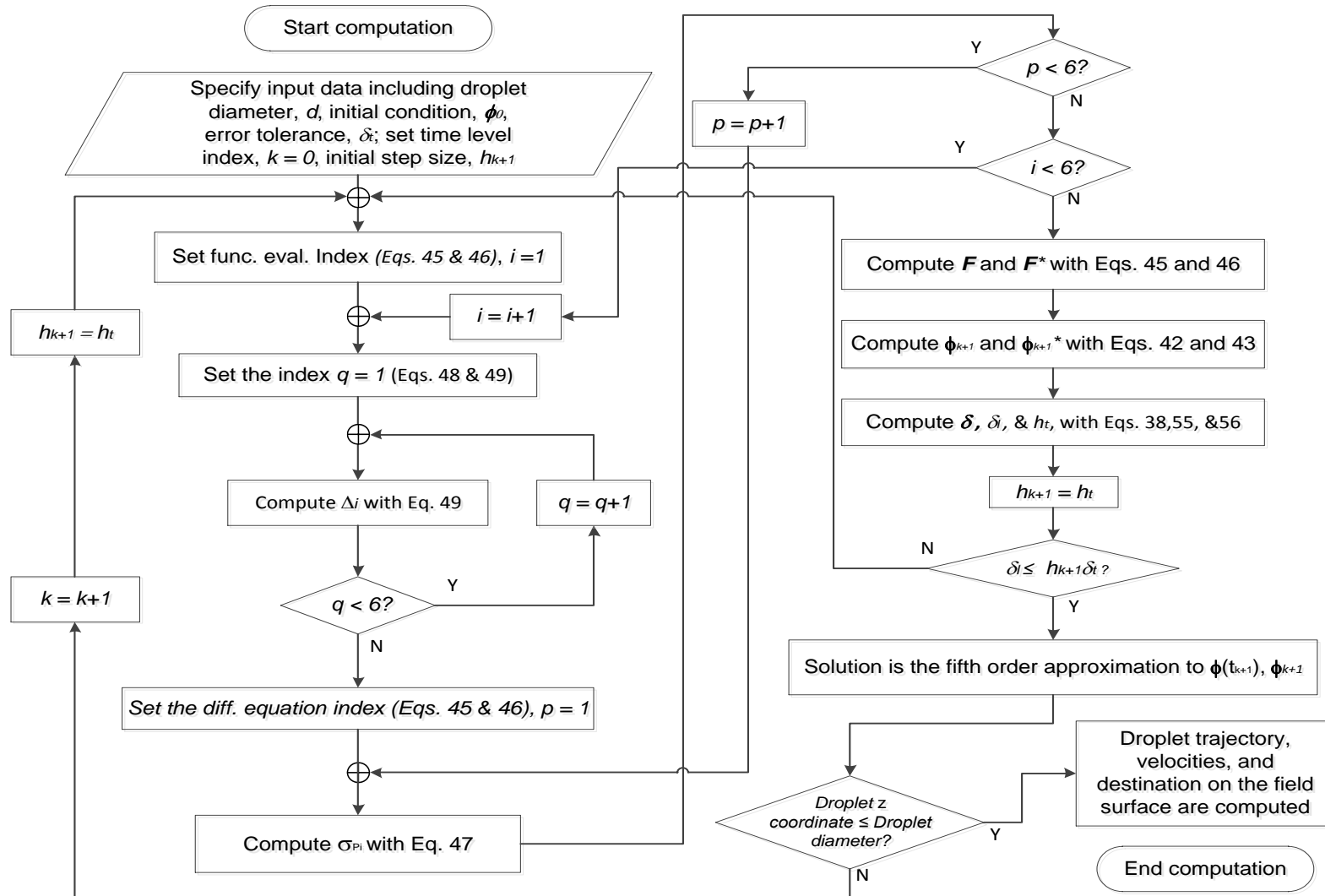


Figure 3 Simplified flow diagram for the droplet dynamics submodel (Runge-Kutta approximation)

- (1) Set time step index: $k = 0$;
- (2) Set stage index: $i=1$;
- (3) For $q=1$ to 6 Compute elements of Δ_i with Eq. 49;
- (4) For $p=1$ to 6 Compute $\sigma_{p,i}$ with Eq. 47;
- (5) If $i < 6$ then set $i = i+1$ and go through steps 3 and 4 above, if not then proceed to step 6;
- (6) Compute ϕ_{k+1} and ϕ_{k+1}^* with Eqs. 42-43 and determine δ_i and h_i (Eqs. 55 and 56) and proceed to step 7
- (7) If error tolerance requirement is met ($\delta_i \leq h_i \delta_i$), then solution for the $(k+1)$ th time step is obtained and it is ϕ_{k+1} ; proceed to the next step. If, on the other hand, $h_i \delta_i < \delta_i$ then solution is unacceptable, set $h_{k+1} = h_i$ and repeat steps 2 through 6 above;
- (8) If droplet coordinate along the z -axis (droplet height above the field surface) is less than droplet diameter, then droplet has reached the irrigated field surface, end computation. If, on the other hand, droplet height above field surface exceeds droplet diameter, then set $k = k+1$ and $h_{k+1}=h_i$ and proceed through steps 2 to 7 above;

For a droplet undergoing unsteady motion under wind, if the horizontal component of the droplet absolute velocity vector falls to or below a threshold value (taken here as 1% of the wind speed), then the horizontal component of the droplet absolute velocity is considered to have been completely dissipated and thereafter the droplet is assumed to be fully carried by the ambient air (i.e., no relative motion between droplet and ambient air on the horizontal plane). In which case the derivatives of the velocity vectors along the x - and y -axes are set to zero and the horizontal velocity components are given as $V_x = W_x$ and $V_y = W_y$. The incremental distances covered by a droplet in a given time step, along each axes, can then be computed as the product of the time step size and V_x and V_y . Vertical droplet motion, however, is computed in accordance with the procedure described above.

Chapter 4 Sprinkler droplet volumetric application rate computation and precipitation pattern simulation

4.1 Introduction

The precipitation pattern about a sprinkler can be emulated only with numerous droplets of known diameters and application rates. Given the droplet diameter, the initial conditions, pertinent physical properties of the ambient air, wind velocity, and model parameters (Section 3.3), the droplet dynamics model presented in the preceding sections can simulate the trajectory that a water droplet takes and its landing coordinate on the irrigated surface. However, because of the limiting assumptions inherent in the droplet dynamics modeling framework (Section 2.4), the output of such a model cannot provide answers to such questions as what is the droplet diameter range applicable to a given sprinkler, nozzle pressure head, and environmental condition combinations? What is the volumetric application rate associated with a given droplet diameter? How many droplets are needed to provide a satisfactorily accurate simulation of the spatial distribution of precipitation about a sprinkler? Evidently, a sprinkler irrigation precipitation pattern simulation model is more than a droplet dynamics model. Hence, additional numerical and empirical procedures need to be devised, and coupled with the droplet dynamics submodel, in order to transform it into a mathematical model capable of simulating irrigation precipitation pattern about a sprinkler.

The approach commonly used for constructing a sprinkler irrigation precipitation pattern simulation model, with a physically based droplet dynamics model at its core, consists of three main phases (Fukui et al. 1980; von Bernuth and Gilley. 1984; Vories et al., 1987; Seginer, et al. 1991; and Carrion et al., 2001; Playan et al., 2009): (i) *Computation of droplet volumetric application rates*: consisting of a semi-empirical procedure aimed at ascertaining droplet diameter range, number of droplets, and droplet volumetric application rates; (ii) *Model calibration*: model calibration concerns the estimation of model parameters based on a comparison of field measured precipitation distribution data about a test sprinkler with that obtained through simulation; and (iii) *Sprinkler precipitation pattern simulation*: based on results from steps *i* and *ii* above, precipitation distribution over an area irrigated by multiple overlapping sprinklers, under field condition, can be simulated. In subsequent sections, first a detailed discussion of the basic principles and assumptions underlying the approach described above is

presented, followed by a step by step account of the specific procedure implemented in the model presented here.

4.2 Assumptions and rationale

4.2.1 Droplet volumetric application rate based on indoor measurements

The application rate over the wetted area of a sprinkler can be considered constant with time (by the steady state flow assumption) and is equal to the sprinkler discharge. The procedure for computing droplet volumetric application rates then aims at answering the simple question of how to parcel out the sprinkler application rate over its wetted area among a finite number of droplets, the landing coordinates of which can be computed with the droplet dynamics model? Because of the simplifications inherent in the droplet dynamics model, consideration of the actual processes by which droplets form and spatially distribute about a sprinkler on real-time basis is not possible and the volumetric water content of individual droplets used in the simulation, *per se*, is not practically useful. Hence, droplet volumetric application rates are computed with a semi-empirical procedure based on data derived through a mix of modeling and measurements conducted under no-wind condition (typically indoors). The main steps consist of: *(i)* Determining the “optimal” number of droplets required to cover the sprinkler wetted area such that the resulting application rate data has sufficiently high spatial resolution to capture the nonuniformity inherent in the precipitation distribution about a sprinkler while at the same time keeping computational effort to a minimum; *(ii)* Computing the radial landing coordinates of droplets with the droplet dynamics model, and *(iii)* Correlating the droplet landing coordinates with measured radial irrigation application rate data to compute droplet volumetric application rates.

The radial application rate of a sprinkler (Figure 4a), expressed in depth per unit time, is obtained through measurements conducted in indoor settings in which a sprinkler, of given model and nozzle size, is operated at a preset pressure head for a selected duration under conditions that minimize spray evaporation (e.g., Carrion et al., 2001; Vories et al., 1987; von Bernuth and Gilley, 1984). Precipitation depths collected in rain gages placed at a regular spacing from the sprinkler along with the duration of irrigation is then used to compute the sprinkler radial application rate. The layout of the indoor radial application rate measurement

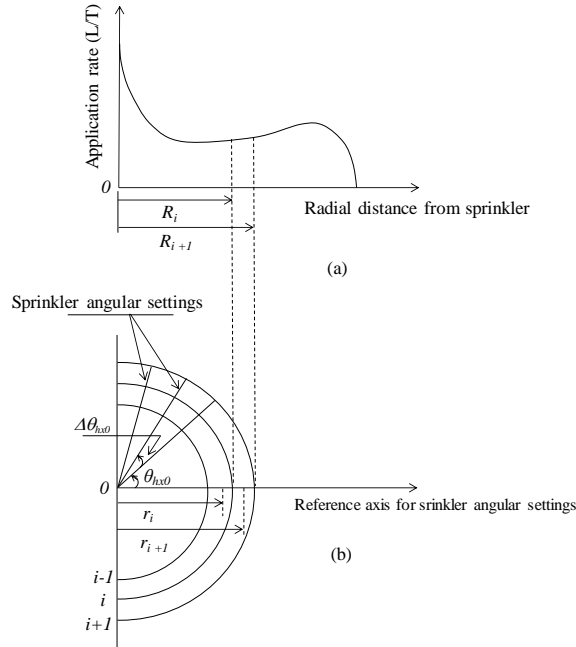


Figure 4 (a) Measured radial sprinkler application rate and (b) Annular ring of irrigated areas representing the radial discretization of the wetted area under the sprinkler (where r_i = the radial distance, measured from sprinkler location to, the landing point on the irrigated surface of the i th droplet diameter; R_i = the radius of the i th concentric circle delineating the i th annular ring of irrigated area from the $(i+1)$ th)

setup, used in the study reported here, is described in Section 6.3.1. A limitation that stems from this empirical approximation is that, in the strictest sense, the droplet volumetric application rates computed as such can only be applied to a condition in which the sprinkler model, nozzle size, and operating pressure head are the same as that used during the sprinkler radial application rate measurement. In practice, however, they can be applied to a set of overlapped sprinklers (of same model and nozzle size) with limited pressure head variation about that used in the application rate measurement.

Subsequent section discusses the steps listed above, for computing droplet volumetric application rate, in some detail.

Determination of number of droplets: Considering a full-circle impact sprinkler (commonly used in solid set sprinkler systems), determination of the number of droplets for precipitation pattern simulation requires discretization of the unit circle about the sprinkler into subintervals of equal

size with a suitably selected angular discretization step, $\Delta\theta_{hx0}$ (Figure 4b). Each angular discretization step corresponds to a sprinkler nozzle setting, which is specified in terms of the associated horizontal angular displacement of the centerline of the sprinkler nozzle from a reference axis, θ_{hx0} . In the model described here the positive x -axis is used as a reference axis to measure the angular setting of the sprinkler nozzle (Figure 5). For a given set of conditions and angular setting of the sprinkler nozzle, the measured radial application rate can be related to a range of droplet diameters. The upper bound of the droplet diameter range, d_{max} , can be computed, with the droplet dynamics model, as a function of the wetted radius of the sprinkler measured under no-wind condition. The minimum droplet diameter, d_{min} , is set based on computational considerations: numerical efficiency and robustness (Section 3.4.3). The droplet diameter range, $[d_{min}, d_{max}]$, defined for a given angular setting can then be discretized with a suitably selected step size, Δd , resulting in a finite number of droplet diameters. Noting that droplet application rate characterization measurements are conducted under no-wind condition, the measured radial application rate can be considered symmetrical about the sprinkler. In which case, the same set of droplet diameters can be used to represent the measured radial irrigation application rate, about the sprinkler, for each of the sprinkler nozzle angular settings which vary

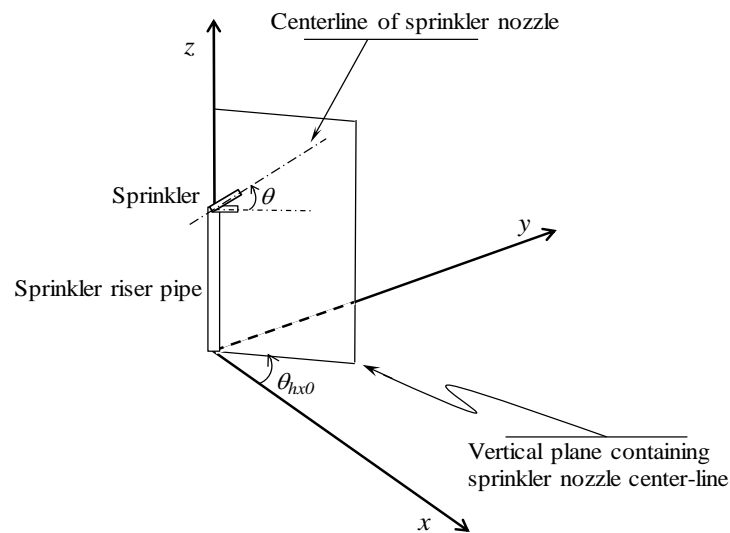


Figure 5 Angular setting of sprinkler nozzle from the reference axis, θ_{hx0} , and sprinkler vertical tilt angle, θ ,

in the range: $0^0 \leq \theta_{hx0} < 360^0$. The implication is that the number of droplets covering the full-circle about a sprinkler can be given as the product of the number of angular discretization steps and the number of droplet diameters in the range $[d_{min}, d_{max}]$. Note that this is the number of droplets used in simulating the precipitation pattern about a sprinkler under field condition. In selecting the appropriate step sizes for angular and droplet diameter discretization, computational considerations and the grid square size used to discretize the irrigated field surface (to be discussed in a subsequent section) need to be taken into account.

Computation of droplet landing coordinates and discretization of the wetted area about the sprinkler: Considering a given angular setting of the sprinkler nozzle, the radial landing distance of each droplet, in the range $[d_{min}, d_{max}]$, on the irrigated field surface can be computed with the droplet dynamics model. The wetted area about the sprinkler, which is a circle, can then be discretized radially into concentric annular rings of irrigated areas, such that each annular ring area contains the landing point of a droplet of given diameter (Figure 4b). Superimposing the sprinkler nozzle angular settings on the radially discretized sprinkler wetted area yields elemental wetted areas (henceforth referred to as grid units) into which the wetted area about the sprinkler is subdivided for droplet volumetric application characterization purpose. Note that the total number of droplets, applicable to any given set of conditions, is equal to the total number of grid units. In other words, each grid unit of wetted area can be associated with the landing point, in the irrigated field surface, of a water droplet. In which case, the determination of droplet volumetric application rates can be reduced to apportioning the sprinkler application rate among the individual grid units constituting the wetted area of the sprinkler. This is the basic rationale underlying the approach used for apportioning sprinkler application rates among droplets, however, recognition of the fact that the measured radial application rate is symmetrical about the sprinkler leads to a considerable simplification of the procedure used for computing droplet volumetric application rates.

Correlating droplet landing coordinates with a sprinkler radial application rate: Considering the symmetry of application rate about the test sprinkler, it can be reasoned that the computation of droplet volumetric application rate requires only correlating the measured radial application rate

of the sprinkler with the droplet radial landing distances, computed for any arbitrarily selected angular setting of the sprinkler nozzle. From the preceding discussion it can be noted that each annular ring of irrigated area about the sprinkler contains a droplet landing point, to which an application rate can be assigned. If the radial discretization of the sprinkler wetted area (Figure 4) is of sufficiently high spatial resolution, then the width of each annular ring of irrigated area can be assumed sufficiently small for the associated application rate to be considered a representative average. In which case the volumetric application rate for an annular ring of irrigated area can be computed as the product of the application rate, at the landing point of the associated droplet, and the area of the annular ring. Because the angular discretization step size is constant, it then follows that the grid units within each annular ring of irrigated area are of equal size. In which case the volumetric application rate associated with a droplet, of a given diameter, can be computed as the ratio of the volumetric application rate over the corresponding annular ring of area to the number of angular discretization steps.

4.2.2 Model calibration based on field measurements

Often sprinkler systems are operated under wind with velocities within a range considered conducive for the attainment of a satisfactory level of system performance. As described by Zerihun and Sanchez (2014b) wind is considered here as a steady uniform horizontal air flow. Hence, in effect the wind velocity is an average value over the duration of irrigation, or some fraction of it, in the surface layer of the atmosphere where water droplet motion takes place. Wind direction is defined here in terms of wind vector azimuth, an angle measured in the clockwise direction from the positive y-axis (Figure 5) to the wind velocity vector. The effect of wind on irrigation precipitation pattern operates at two levels (Section 2.4.2). It distorts the trajectories and landing coordinates of individual droplets (compared to an equivalent no wind condition) and also it affects the physical processes of liquid jet breakup and droplet size distributions (e.g., Kohl, 1974), by modifying the relative velocity of the water jet with respect to the ambient air. However, given the simplifications inherent in the droplet dynamics model, a rigorous and explicit accounting of these effects within the modeling framework described here for sprinkler applications is unwarranted. Hence, the established approach for modeling wind effects on precipitation pattern about a sprinkler assumes that: (i)

the droplet volumetric application rates derived based on measurements under no-wind condition are applicable to the test sprinkler under field conditions as well (Carrion et al., 2001; Seginer et al., 1991; Vories et al., 1987; Fukui et al., 1980) and (ii) the effect of wind on precipitation distribution can be taken into account with empirical shape fitting parameters derived based on field measured precipitation pattern about a test sprinkler (Playan et al., 2009; Carrion et al., 2001; Seginer et al., 1991). Note that this is in addition to wind effects on the relative velocity vector. The term test sprinkler refers here to a sprinkler of the same model, nozzle size, and operating pressure as that used in the (indoor) sprinkler radial application rate measurement. In the following section a description of the approaches used to quantify precipitation rates, depths, and estimation of model parameters is presented.

Discretization of irrigated area: In order for the computed droplet volumetric application rates to be practically useful (in the context of precipitation pattern simulation under field conditions) they need to be related with an elemental area (e.g., a grid square) of known coordinates on the irrigated field surface (e.g., Vories et al., 1987). In which case, the irrigated field needs to be discretized into grid units of appropriate size. The discretization scheme described above, in relation to the computation of droplet volumetric application rates, is difficult to work within the context of simulating the spatial distribution of sprinkler applied irrigation water, especially under conditions involving multiple overlapping sprinklers, hence will not be considered further. A simple discretization scheme amenable to such an application consists of subdividing the irrigated area into grid squares of constant size (Figure 6). Note that in the model described here the field surface is considered horizontal (based on the assumption of a nearly flat field surface).

For a given irrigated area, the grid square size used to discretize the irrigated field determines the spatial resolution with which precipitation distribution is computed. However, in selecting the grid square size, consideration needs to be given to the fact that smaller grid squares can yield precipitation distribution data with higher spatial resolution only if the droplet diameter and angular discretization steps as well are sufficiently small, which entails higher computational costs. On the other hand, too large a grid size may mask the nonuniformities inherent in the irrigation precipitation distribution, and perhaps result in a wasted computational effort if it is

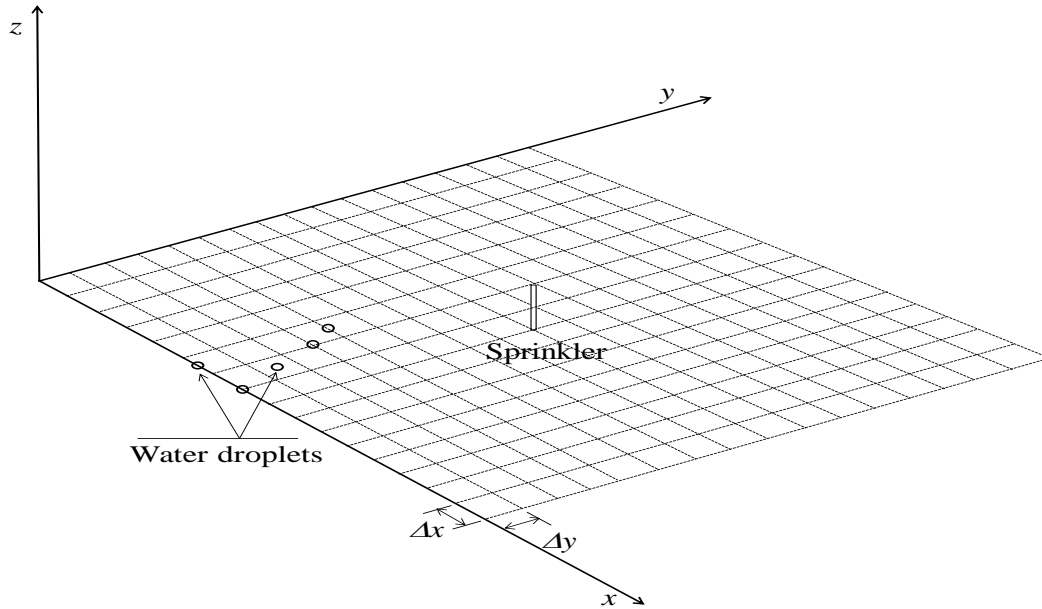


Figure 6 Discretization of the irrigated field surface for sprinkler irrigation precipitation distribution computation (x and y = horizontal coordinate axes which represent distances on the field surface and z = the vertical coordinate, which represents applied irrigation depth or precipitation rate, Δx and Δy = grid dimensions)

coupled with very fine droplet diameter and/or angular discretization. Hence, droplet diameter, angular, and field discretization steps should be selected with the view of balancing the need for computational efficiency with the need for adequate spatial resolution of the computed irrigation distribution.

In order to simulate the precipitation pattern about a sprinkler under field condition, the sprinkler nozzle is rotated through each of the preselected angular settings, which vary in the range: $0^\circ \leq \theta_{noz} < 360^\circ$, and for each nozzle setting the landing coordinates (as affected by wind) of the droplets ranging in diameters between d_{min} and d_{max} are computed. The application rate within a grid square (expressed in terms of depth per unit time) is then computed as the sum total of the contribution of each droplet that landed within or on the edges of the grid square.

Obviously, for practical computational purposes the motion of individual droplets is simulated separately and consecutively. However, it is important to note that the chronology of droplet motion in the droplet dynamics modeling framework does not in any way correspond to the actual process of droplet motion in real-time; hence it is impertinent to the computation of

application rates associated with grid squares. In other words, in so far as sprinkler precipitation pattern simulation is concerned, the significant output of the droplet dynamics simulation is the computed landing points of the droplets whose volumetric application rates are known. The practical implication of the preceding observations is that the aggregate contribution of water droplets that landed within or on the edge of a grid square, to the application rate over a grid square, is considered to have occurred within a suitably selected unit real-time scale, used for the quantification of application rates in the model (i.e., a second, a minute, etc.).

Wind drift and spray evaporation losses: Computed droplet volumetric application rates do not take into account spray evaporation losses and evidently wind drift losses are considered zero. However, simulation of sprinkler irrigation precipitation pattern under field conditions requires quantification of spray evaporation and wind drift losses, based on which the grid square application rates are to be adjusted. Wind drift and spray evaporation losses, often expressed as percentage of the sprinkler average application rate, can be computed as function of pertinent climatic factors (e.g., Playan et al., 2005). Alternative approaches for taking into account spray evaporation and wind drift losses in the context of a sprinkler irrigation precipitation pattern simulation model is described by Carrion et al. (2001). In the model described here spray evaporation and wind drift losses are considered separately. Spray evaporation loss is not explicitly computed within the model, instead it is specified at the input as a fraction of the irrigation application rate. In addition, an irrigation event is considered to take place within a defined field boundary specified at the input. Hence, droplets that fall outside the irrigate field or on the edge of the irrigated field are considered to contribute to wind drift loss. Evidently some of the water that becomes wind drift loss evaporates before it reaches the field surface, however, in this model no distinction is made between the wind drift loss and the fraction of it that becomes spray evaporation loss. Spray evaporation fraction of the irrigation application is estimated with a volume balance approach based on field measured data (Section 6.3.1). Eventually the application rates for each of the grid square, within the irrigated field, are corrected for spray evaporation losses.

Note that the preceding discussion implies that field data, applicable to the calibration of the model described here, should have a precipitation pattern (sprinkler wetted area) that is

entirely circumscribed by the boundary of the test-plot. Hence, the test-plot size and the location of the sprinkler within it should be defined taking this requirement into account.

Computation of irrigation depths reaching the irrigated field surface: The application rates computed for each grid square, after having been adjusted for spray evaporation losses, can then be integrated over the duration of irrigation to yield the irrigation depth reaching a grid square.

Estimation of model parameters: In the model described here pertinent parameters consist of scale factors for wind effects on drag, ζ_1 , and droplet drift, ζ_2 , and empirical drag correction parameter for acceleration effects, ζ_3 (Eqs. 13-18). Ideally the model parameters should be estimated through inverse modeling, such that the difference between the field measured and computed precipitation patterns about a test sprinkler, expressed in terms of some selected error measure, is minimized. Seginer et al. (1991) and Carrion et al (2001) have discussed applicable procedures for estimating pertinent parameters to their models. The model developed here has no inverse modeling functionality, hence model calibration is conducted through trial and error based on comparisons of model predicted and field measured precipitation patterns about a single sprinkler. The layout of the precipitation pattern measurement apparatus used in the single sprinkler field evaluations conducted in the current study is described in Section 5.3.2.

4.2.3 Sprinkler precipitation pattern simulation under field conditions

Sprinkler precipitation pattern simulation under field condition concerns the computation of the distribution of irrigation applied water over an area irrigated by a set of overlapped sprinklers. In which case, precipitation distribution computation requires overlapping the patterns from adjacent sprinklers whereby each grid square may receive water from more than one sprinklers. A simple approach involves applying the precipitation pattern obtained for a single sprinkler to all the sprinklers in a set. This is based on the assumption that the sprinklers are of the same model, nozzle size, and are operated at pressure heads not significantly different from that used in the sprinkler radial application rate measurement. The approach is computationally efficient, and in theory, rather consistent with the principle underlying the computational framework described above. An alternative procedure implemented in the current model,

because it does not require additional programming effort, involves the simulation of the precipitation pattern distribution about each sprinkler in the set based on the operating pressure head of the individual sprinklers, in which case the initial conditions would be slightly different from one sprinkler to another in the set. Both approaches should give more or less the same results so long as sprinkler pressure head variation within the set is limited to a narrow range about the pressure head used in the radial application rate measurement. Note that if the range of field-scale sprinkler pressure head variation is considered significant to be represented in terms of a single radial application rate dataset, then measurements need to be made at more than one sprinkler pressure heads, spanning the field-scale variation. Droplet volumetric application rates should then be derived for each one of them.

A detailed outline of the specific procedures implemented in the model described here is presented subsequently. Following the discussion above, the presentation is divided into two segments. The first segment outlines the steps for computing the droplet volumetric application rates based on sprinkler radial application rate patterns derived through indoor measurements (Figure 7). The second segment lists the steps used for simulating the spatial distribution of precipitation about a sprinkler or multiple overlapping sprinklers irrigating a field under a steady uniform horizontal wind (Figure 8).

4.3 Computational procedures

4.3.1 Droplet volumetric application rates

(1) Determine the sprinkler radial application rate. The radial application rate of a sprinkler is obtained through measurements conducted in indoors settings in which a sprinkler, of given model and nozzle size, is operated at a preset pressure head for a selected duration under conditions that minimize spray evaporation. Precipitation depths collected in rain gages placed at a regular spacing from the sprinkler along with the duration of irrigation is then used to compute the radial sprinkler application rate;

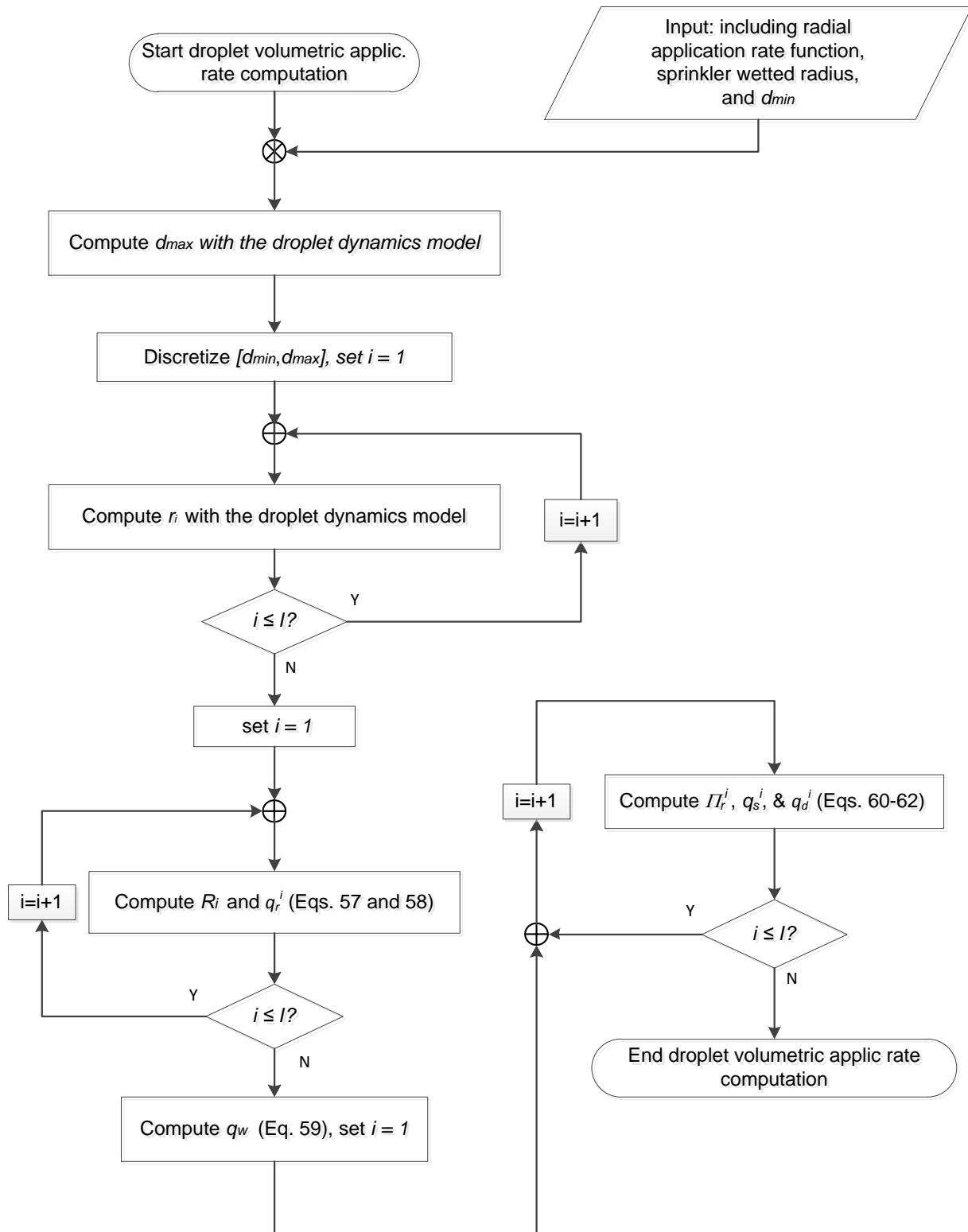


Figure 7 Flow diagram for droplet volumetric application rate computation

(2) *Determine droplet diameter range* [d_{min}, d_{max}]: The maximum droplet diameter, d_{max} , is computed with the droplet dynamics model as a function of the measured wetted radius and the minimum droplet diameter, d_{min} , is set based on computational considerations: numerical efficiency and robustness;

(3) *Discretize the droplet diameter range*: A suitably selected step size, $\Delta d = (d_{max} - d_{min})/I$ (where I = the number of subintervals into which the droplet diameter range is subdivided), is used to discretize the droplet diameter range into subintervals of constant size;

(4) *Radial distance of droplet landing point from sprinkler*: For each droplet diameter, d^i (for $i = 1, 2, \dots, I+1$), within the range [d_{min}, d_{max}], compute the horizontal distance, r_i , between the sprinkler and the point at which the droplet lands on the field surface (Figures 4) with the droplet dynamics model;

(5) *Radial discretization of the wetted area about the sprinkler*: Discretize the wetted area about the sprinkler into concentric annular rings of irrigated areas, such that each annular ring area contains a droplet landing point. In the model described here, the radius of the i th circle, R_i , which delineates the i th annular ring of irrigated area from the $(i+1)$ th is computed with

$$R_i = r_i + \frac{r_{i+1} - r_i}{2} \quad (57)$$

Note that radial discretization of the wetted area presumes that for a condition in which there is no-wind, precipitation distribution is symmetrical about the sprinkler;

(6) *Volumetric application rates for each annular ring area*: The volumetric application rate over the i th annular ring of irrigated area, q_r^i [L^3/T], based on the measured radial application rate, can then be computed with

$$q_r^i = \pi (R_i^2 - R_{i-1}^2) A_r^i \quad (58)$$

where A_r^i = irrigation application rate at the landing point of the i th droplet [L/T]. A_r^i can be interpolated from the measured radial application rate data or can be computed from a curve fitted to the measured data. In the current model it is computed from a radial irrigation

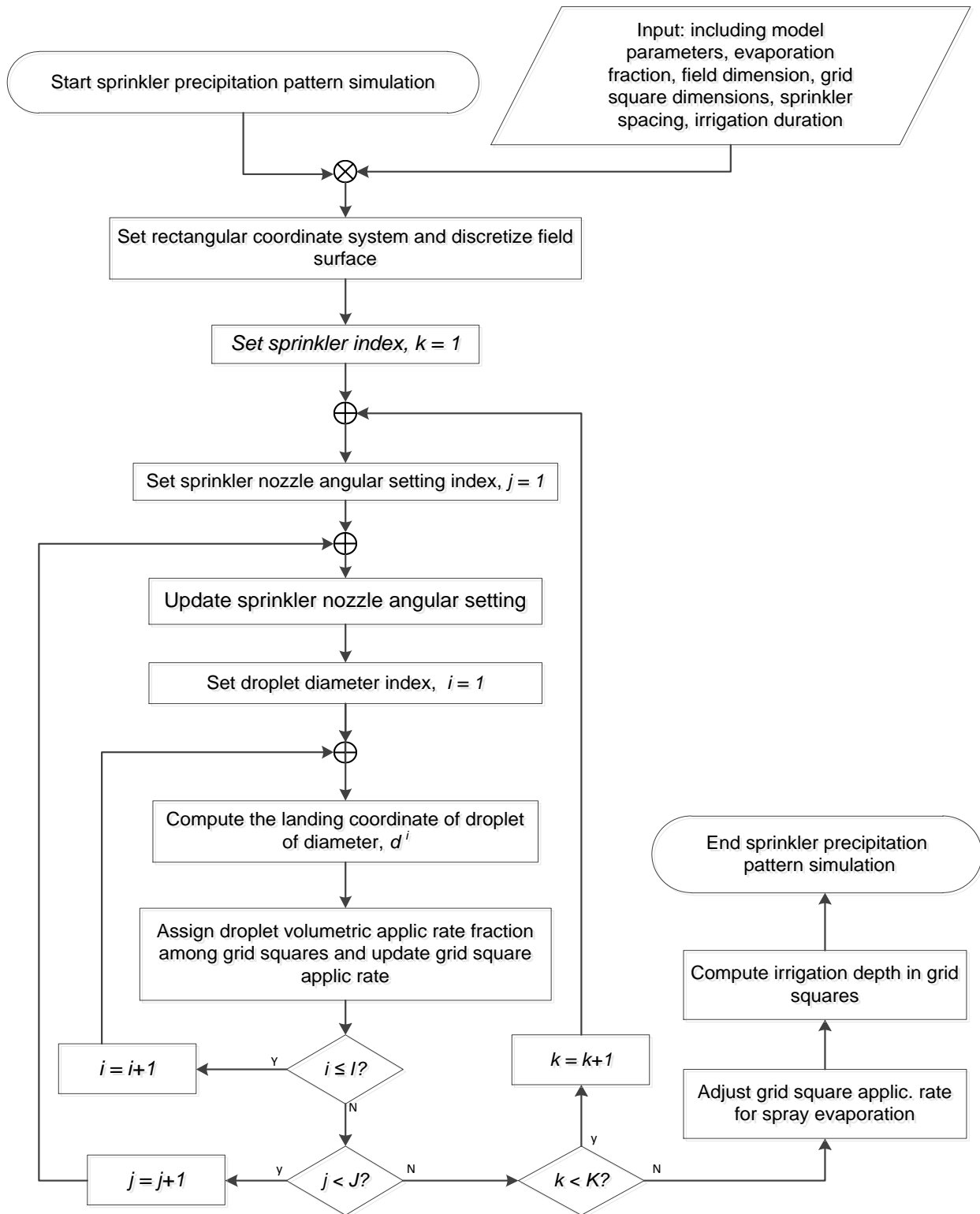


Figure 8 Sprinkler precipitation pattern simulation under field condition

application rate curve obtained through curve fitting. Note that Eq. 58 presumes that the radial discretization of the sprinkler wetted area is such that the width of each annular ring of irrigated area is sufficiently small for the associated q_r^i to be considered a representative average;

(7) *Volumetric application rate over the wetted area about the sprinkler*: The volumetric application rate over the wetted area about the sprinkler, $q_w [L^3/T]$, based on the measured radial application rate can be computed with

$$q_w = \sum_{i=1}^I q_r^i \quad (59)$$

(8) *Dimensionless radial distribution of volumetric application rate*: For the i th annular ring of irrigated area, the dimensionless radial distribution of volumetric application rate, normalized with q_w , $\Pi_r^i [-]$, can then be expressed as:

$$\Pi_r^i = \frac{q_r^i}{q_w} \quad (60)$$

(9) *Specific discharge*: The specific discharge, q_s^i , which is the fraction of the sprinkler discharge, q_s , that would be applied to the i th annular ring of irrigated area, if there was no evaporation, can be expressed as

$$q_s^i = \Pi_r^i q_s \quad (61)$$

Note that Eq. 61 assumes that the rate of spray evaporation loss is invariant with distance from sprinkler and is equal to the ratio of the evaporation depth to the total applied irrigation depth. Note that maintaining a condition that minimizes spray evaporation during the indoor sprinkler test would improve the accuracy of Eq. 61.

(10) *Compute droplet volumetric application rates*: In accordance with the discussion in the preceding section, the droplet volumetric application rate, q_d^i , for the i th droplet in the range $[d_{min}, d_{max}]$ can be computed with:

$$q_d^i = \frac{q_s^i}{\left(\frac{360^\circ}{\Delta\theta_{hx0}} \right)} \quad (62)$$

The droplet volumetric application rates computed with Eq. 62 can then be used to simulate the distribution of irrigation applied water over a wetted area about a sprinkler, or a set of overlapping sprinklers, under field conditions.

4.3.2 Spatial distribution of sprinkler irrigation

(1) Model calibration: As mentioned above, model calibration here concerns the estimation of parameters of the droplet dynamics model, consisting of scale factor for wind effects on drag, ζ_1 , and droplet drift, ζ_2 , and an empirical drag correction parameter for acceleration effects, ζ_3 . The model described here has no inverse modeling functionality, hence model calibration is conducted through trial and error. Model calibration is based on precipitation distribution data collected through a single sprinkler field test. The field evaluation uses the same sprinkler and operating pressure as that used in the indoor tests. In the model described here, wind velocity vector can be specified in terms of hourly average data during the course of the irrigation event or as an average value over the entire irrigation application period. The advantage of using hourly average wind speed and direction is that wind effects on precipitation pattern can be specified at much higher temporal resolution. However, when hourly average wind velocity data is used the parameter sets for each hour of the irrigation duration may not be the same. Hence, the increase in the number of model parameters will lead to increased complexity in parameter estimation. In addition, precipitation distribution for each hour of the irrigation duration need to be simulated separately, resulting in increased computational time by a factor equal to the number of hours in a test irrigation.

(2) Set a rectangular coordinate system: The coordinate system should be selected such that the sprinkler (in case of single sprinkler simulation) or the field (in case of overlapped sprinkler simulation) is located in the first quadrant of the horizontal plane of the coordinate system (e.g., Figure 6). This is not necessary, but it is a simple setup implemented in the current model;

(3) *Discretize the irrigated field surface into grid squares of equal size:* Select a suitable grid square size for irrigation application rate and depth computations and discretize the field surface as shown in Figure 6. Factors that need to be considered in selecting grid square dimension are discussed in the preceding section;

(4) *Compute droplet landing points:* For a given angular setting of the sprinkler nozzle compute the landing coordinate of each droplet diameter, d^i , with the droplet dynamics model (for $i = 1, 2, \dots, I+1$, where $I =$ the number of subintervals into which the droplet diameter range, $[d_{min}, d_{max}]$, is discretized);

(5) *Assigning droplet volumetric application rates to grid squares:* Considering the same sprinkler nozzle setting as that used in step 4 above, the volumetric application rate, q_d^i , of the i th droplet diameter, d^i (for $i=1, 2, \dots, I+1$), is apportioned between grid squares as follows (e.g., Carrion et al., 2001): (i) If a droplet lands within a grid square (Figure 6), the entire application rate it represents is assigned to that grid square; (ii) If the droplet lands on a line separating two adjacent grid squares then, half the application rate associated with the droplet will be assigned to each of the respective grid square; (iii) If the droplet lands on a corner shared by four adjacent grid squares, then each quarter of the application rate associated with the droplet will be assigned to each of the respective grid squares; (iv) If a droplet lands outside the edge of a field specified at the input, then its considered to be part of the wind drift losses; (v) If a droplet lands on the edge of the field, then the droplet volumetric application rate is divided between the respective grid squares and the wind drift loss following the procedure described in steps ii through iv above;

(6) *Updating the application rate in a grid square:* Considering a droplet of diameter, d^i , which contributes some fraction of its volumetric application rate to a grid square, the application rate for the grid square is then updated as follows: add the fraction of the droplet volumetric application rate applicable to the grid square to the antecedent application rate in the grid square. The antecedent application rate in a grid square is the sum total of the contributions of droplets, whose motion was simulated a priori, to the irrigation application rate in the grid square;

(7) *Change sprinkler nozzle setting and repeat preceding steps:* Rotate the sprinkler to the desired angular setting with respect to a reference axis (given as $((j-1)\Delta\theta_{hx0})^o$ for $j = 1, 2, \dots, J$, where $J =$ the number of angular discretization steps, $J = 360^o/\Delta\theta_{hx0}$) and repeat steps 4 through 6 above. Note that the direction of rotation of the sprinkler used in the current model is counter clockwise;

(8) *For a set of overlapping sprinklers repeat preceding steps:* The contribution of each sprinkler, in the overlapped set, to the spatial distribution of irrigation application rate over the irrigated area is computed by repeating steps 4 through 7 above. Computation in the preceding steps is based on a single droplet volumetric application rate dataset, hence consideration of overlapped sprinklers here presumes that sprinkler pressure heads in the set are not significantly different from the pressure head used in the indoors sprinkler test.

(9) *Evaporation rate adjustment:* In the model presented here evaporation rate is specified at the input as a fraction of the irrigation application rate. For each grid square the application rate computed above is adjusted by subtracting an amount equal to the evaporation fraction specified at the (model) input. Determination of spray evaporation losses based on field measured data is described in Section 6.3.2.

(10) *Wind drift losses:* Droplets that fall outside the field or on the edge of the field contribute to the wind drift losses. However, it should be noted that such losses can occur, even when wind velocity is zero, if sprinklers are placed sufficiently close to the edge of the field. In the model described here no distinction is made between the wind drift loss and the fraction of it that contributes to the overall spray evaporation loss. Note that for computational purposes the entire wind drift loss is considered to be contributing to a single grid square of the same size as that used to discretize the irrigated field. This implies that the model does not keep track of the spatial distribution of wind drift losses;

(11) *Compute applied irrigation depth for a grid square:* Noting that irrigation application is considered steady, for each grid square applied irrigation depth is computed by multiplying the duration of irrigation with the application rate for the grid square;

The sprinkler precipitation pattern simulation model described here is not yet coupled with a field-scale hydraulic model. However, it is capable of simulating the distribution of irrigation application resulting from multiple overlapped sprinklers over a limited area, if the pressure heads for each of the sprinkler in the set is specified at the input. In its current form the model can only utilize a single measured radial irrigation application rate data, hence sprinkler pressure heads cannot be significantly different from the pressure head used in the single sprinkler indoors test. In any case it should be noted that this model functionality is designed only to explore the potential application of the precipitation pattern simulation model in field-scale solid set sprinkler irrigation system performance evaluation. Assuming sprinkler application rates are less than the soil intake rate, a simple root-zone water balance functionality (based on the field capacity approach) is incorporated into the model to allow field-scale performance computation. The main computational phases of the sprinkler irrigation precipitation pattern simulation model described here are depicted in Figure 9. Figure 9 also provides a list of the model inputs, consisting of model parameters as well as environmental, sprinkler, and field datasets. It also shows how the input data sets relate to the computational phases.

5. Description of the components of the sprinkler irrigation precipitation pattern simulation model

The sprinkler irrigation precipitation pattern simulation model described here is a C++ program developed based on the object oriented programming approach. The model has six classes (user defined data types and member functions): *CSprinklerPrecipitationModel*, *CInput*, *CWaterDropletDynamics*, *CComputeIrrigationPrecipitationPattern*, *CIrrigationPerformance*, and *COutput*. Each of these classes consist of a pair of files: a header file for the declaration of member functions with the extension (.h) and an implementation file with extension (.cpp). The header files are those in which the member functions and variables of a class are declared and their attributes defined: *SprinklerPrecipitationModel.h*, *Input.h*, *WaterDropletDynamics.h*,

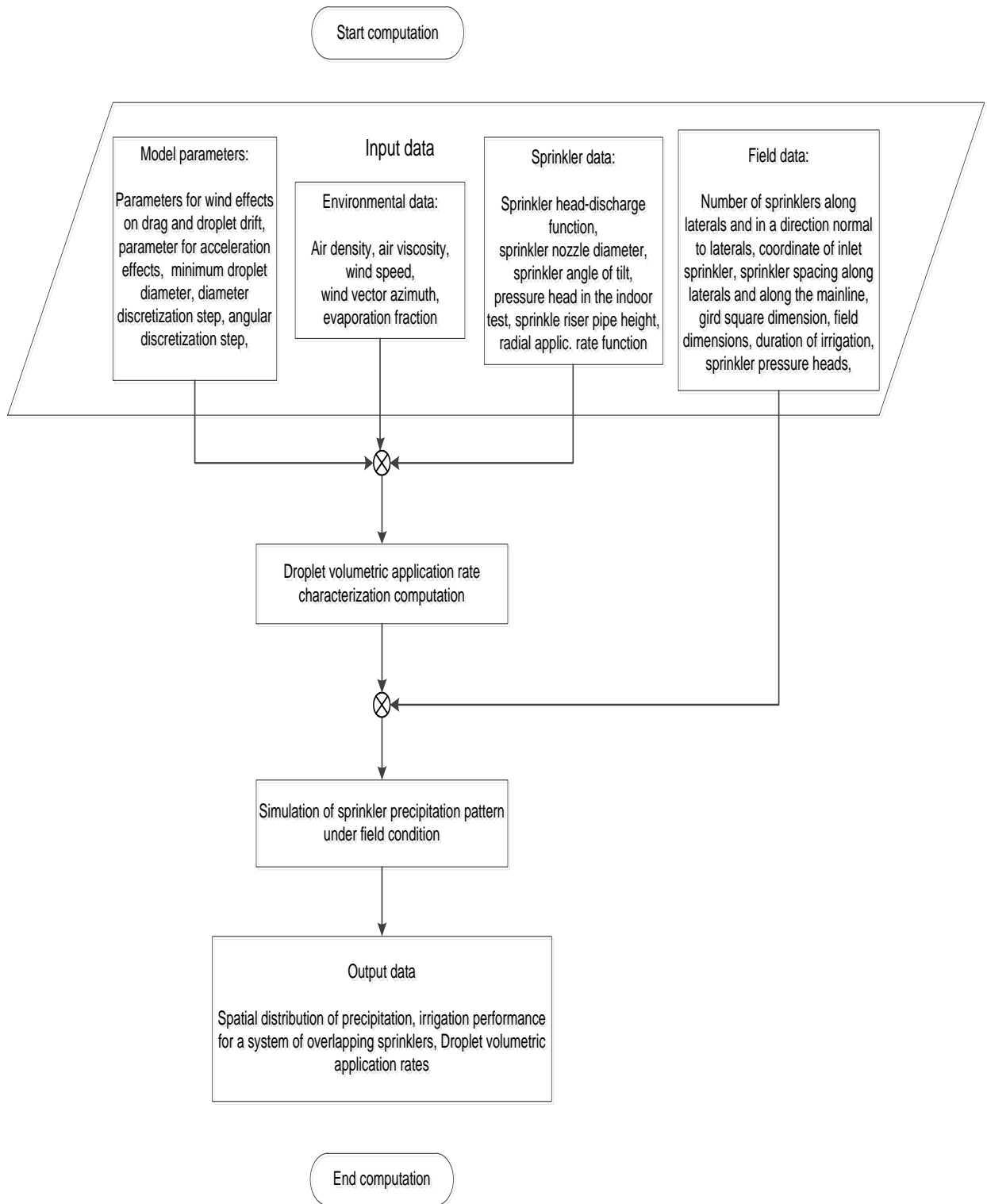


Figure 9 Input data sets and their relationship with the main computational phases of a sprinkler irrigation precipitation pattern simulation model

ComputeIrrigationPrecipitationPattern.h, *IrrigationPerformance.h*, and *Output.h*. The implementation files are those in which functions declared in the header files are implemented: *SprinklerPrecipitationModel.cpp*, *Input.cpp*, *WaterDropletDynamics.cpp*, *ComputeIrrigationPrecipitationPattern.cpp*, *IrrigationPerformance.cpp*, and *Output.cpp*. An additional file *SIPSM.cpp* (*Sprinkler Irrigation Precipitation Simulation Model*) contains the main function of the program.

The class *CSprinklerPrecipitationModel* has one member function with a public scope called *Run*, which is invoked by a function call from the *SIPSM.cpp* file. It also has a number of member functions that are private to the class and are designed to compute sprinkler wetted diameter, droplet diameter range and discretization steps, and droplet volumetric application rates based on measured sprinkler radial application rates. In addition it is in this class where program variables with global scope are declared and function calls to the main member functions of the *CInput*, *CWaterDropletDynamics*, *CIrrigationPerformance*, and *COutput* classes are made.

The *CInput* class has several member functions declared in the header file, *CInput.h*. The functions in the *CInput* class create the folder, in which input and output data files are stored, during run time and read input data from files. There are two input data files used by the model: (i) *SprIrrigPrecSimulation.Inp* file contains input data used as an input to the precipitation pattern simulation model. This include pertinent physical properties of the ambient air, hourly average wind speed and direction, model parameters, geometric data (as related to field layout, sprinkler spacing's, field dimensions, and field discretization step size for numerical simulation), and irrigation management related factors such as irrigation application duration and required depth of application; and (ii) *SprRadialApplicRate.Inp* file contains input data mainly used in droplet volumetric application rate characterization computation. The data in this file consists of minimum droplet diameter, angular discretization steps for numerical computation, sprinkler design factors (nozzle diameter, pressure head-discharge relationships, and vertical tilt angle), sprinkler riser pipe height, nozzle pressure head during sprinkler tests, an array of sprinkler pressure head data for field-scale simulation, and parameters of a cubic polynomial obtained through regression fit to measured sprinkler radial application rate data.

The *CWaterDropletDynamics* class has several member functions designed to initialize pertinent variables of the droplet dynamics model and compute the trajectories and landing coordinates of individual droplets on the irrigated field surface with a Runge-Kutta numerical method (Section 3.4). This is also the class from which member functions of the *CComputeIrrigationPrecipitationPattern* class are accessed.

The *CComputeIrrigationPrecipitationPattern* class has member functions, declared in the header file, that have both public scope and are private to the class. Based on the landing coordinates of individual droplets computed in the *CWaterDropletDynamics* class, the functions in this class apportion the volumetric application rates associated with a droplet among grid squares in the irrigated field and compute grid square application rates (Sections 4.2.2 and 4.2.3).

The *CIrrigationPerformance* class contains member functions that compute field-scale irrigation performance (application efficiency, uniformity, and irrigation requirement index), based on computed grid square application rates, spray evaporation fraction, and irrigation requirement specified at the input (assuming a scenario in which sprinkler precipitation rates are less than soil intake rate).

The *COutput* class has several member functions both with public and private scope. These functions save output data files into a subfolder created by the program during runtime. The model output is saved in three text files: (i) *DepthOfIrrigation.Out* file contains computed precipitation depths in each of the grid squares, in an irrigated field, arranged in a tabular format; (ii) *DepthOfIrrigationForContour.Out* has the same content as the *DepthOfIrrigation.Out* file, but the data is arranged in a format that it can readily be opened and processed by a contouring software such as *SURFR*; and (iii) *DrpsVolumetricApplicRate.Out* file contains an array of droplet diameters and associated droplet volumetric application rates used in a precipitation pattern simulation.

Chapter 6 Model evaluation

Model evaluation is conducted at two different levels. First the droplet dynamics submodel that forms the physical basis of the sprinkler precipitation pattern simulation model is evaluated

through a comparison of its outputs with a simplified analytical model and based on intuitive physical reasoning. This is then followed by model evaluation based on a comparison of measured and simulated data.

6.1 Comparison of the numerical model with analytical solutions

Considering a spherical droplet of constant diameter undergoing an impulsively started motion, with known initial conditions, through a static frictionless fluid (aerodynamic drag is zero), the equation that describes its motion reduces to the simple two dimensional form:

$$\frac{d^2x}{dt^2} = 0 \quad (63)$$

$$\frac{d^2z}{dt^2} = -g \quad (64)$$

With the initial condition

$$\left. \begin{aligned} x(t=0) = 0.0 \text{ and } z(t=0) = z_0 \\ V_x(t=0) = |\mathbf{V}_0| \cos(\theta) \text{ and } V_z(t=0) = |\mathbf{V}_0| \sin(\theta) \end{aligned} \right\} \quad (65)$$

The analytical solution for Eqs. 63 and 64 is

$$V_x(t) = |\mathbf{V}_0| \cos(\theta) \quad (66)$$

$$x(t) = |\mathbf{V}_0| \cos(\theta) t \quad (67)$$

$$V_z(t) = |\mathbf{V}_0| \sin(\theta) - gt \quad (68)$$

$$z(t) = z_0 + |\mathbf{V}_0| \sin(\theta) t - \frac{gt^2}{2} \quad (69)$$

The variables in Eqs. 63-69 are defined in relation to Eqs. 13-18. Assuming a horizontal field surface, the origin of the coordinate system is set at the bottom of the sprinkler riser pipe, which is considered to be vertical. The input data sets used for comparing the numerical model with the analytical solution (Eqs. 66-69) is given in Table 2 (dataset I). Dataset I represents a scenario in which a droplet with a diameter of 3.0mm is released from a sprinkler nozzle, with a vertical tilt

angle of 25°, set at a height of 1.2m above the field surface. Five different initial velocities, specified in terms of nozzle pressure heads ranging between 25.0m-45.0m in intervals of 5.0m, are considered (Table 2). Noting that in sprinkler droplet dynamics modeling the droplet initial velocity vector is assumed to be equal to the average stream cross-sectional velocity at the sprinkler nozzle (Section 2.4), in the model described here the modulus of the droplet initial velocity vector is computed with Eq. 70 as a function of nozzle pressure head:

$$|V_0| = C_d \sqrt{2gh_s} \quad (70)$$

Table 2 Datasets used in the comparison of the numerical and analytical solutions and in the analysis of wind effects on droplet motion

Variables	Unit	<i>Dataset I</i>	<i>Dataset II</i>	<i>Dataset III</i>
¹ Density of air	(kg/m ³)	-	-	1.205
² Kinematic viscosity of air	m ² /s	-	-	0.0000151
Water droplet diameter	(m)	0.003	0.004	0.0002-0.003
Drag correction parameter for droplet acceleration effects	(-)	0.0	0.0	-0.025
Scale factor for wind effects on drag	(-)	0.0	0.0	0.75
Scale factor for wind effects on droplet drift	(-)	1.0	1.0	2.5
Sprinkler pressure head	(m)	25.0-45.0	30.0	35.0
Sprinkler discharge coefficient	(-)	0.5	0.5	0.918
Sprinkler nozzle height above field surface	(m)	1.2	0.45	0.45
Sprinkler vertical angle of tilt (θ)	(deg)	25	7-60	23
Sprinkler angular setting	(deg)	0.0	45	0
Wind speed	(m/s)	0.0	0.0	1.25/2.5
Wind vector azimuth	(deg)	-	-	0-270

^{1,2} Density and kinematic viscosity of air at standard condition (20°C , 1.0atm, dry air), The lower limit of the nozzle vertical tilt angle is set based on data from sprinkler manufacturers catalogue (*WeatherTec*: <http://weathertec.com>) and the upper limit of the range is set with the view of having a few data points above 45°

In Eq. 70 C_d = discharge coefficient of sprinkler nozzle (-), g = gravitational acceleration (m/s²), and h_s = sprinkler pressure head (m). Note that the discharge coefficient of the sprinkler is set at a lower value of 0.5 in order to constrain the computed distances and velocities within realistic

ranges. As can be noted from Figure 10 the droplet trajectories computed with the numerical model compare very well with those obtained with the analytical model.

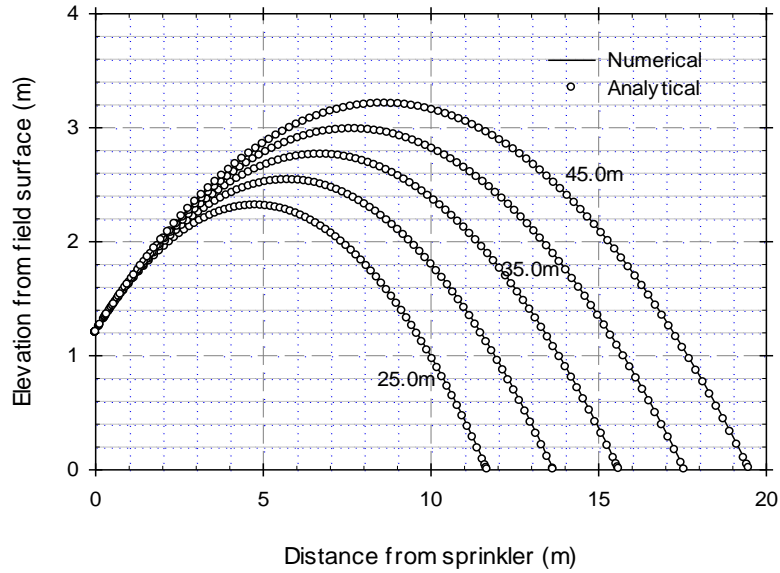


Figure 10 Comparison of droplet trajectories computed with the numerical and analytical models for different initial conditions

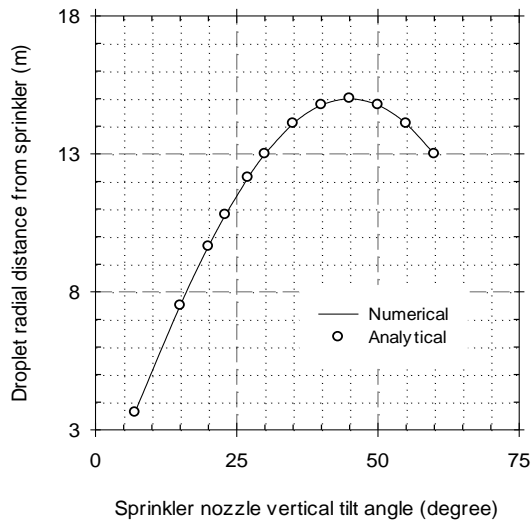
Furthermore, it can be shown from Eqs. 65, 67 and 69 that the radial distance, x , between the sprinkler nozzle and a point, on the same horizontal plane as the droplet exit point from the nozzle, through which the droplet passes during its downward motion is given as

$$x = \frac{|\mathbf{V}_0|^2}{g} \sin(2\theta) \quad (71)$$

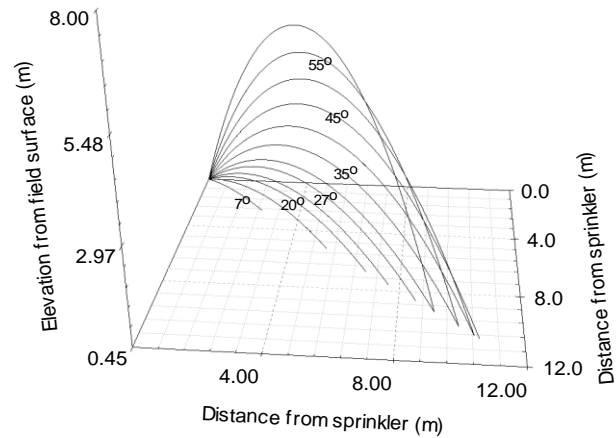
This distance will henceforth be simply referred to as droplet radial distance from the sprinkler. From Eq. 71 it follows that for a given droplet diameter and initial condition (nozzle pressure head), the nozzle vertical tilt angle that yields maximum radial distance, x_{max} , is 45.0° (i.e., when the droplet initial velocity vector is equally divided between its horizontal and vertical components). The equation for x_{max} can then be expressed as

$$x_{max} = \frac{|V_0|^2}{g} \quad (72)$$

Droplet radial distances, from the sprinkler nozzle, computed with the analytical and numerical models, as a function of sprinkler nozzle vertical tilt angle, are shown in Figure 11a. The dataset used for model evaluation is presented in Table 2 (dataset II). Computed droplet radial distances with the numerical model are in good agreement with those obtained with the analytical solution, Eq. 71. The analytical solution predicts that the maximum droplet radial distance from the sprinkler nozzle occurs at $\theta = 45^\circ$ and from Eq. 72 the corresponding distance for the specified initial condition (pressure head) is 15.0m. For the condition in which aerodynamic drag is zero, the numerical model as well computes a maximum droplet radial distance of 15.0m, which occurs at $\theta = 45^\circ$ (Figure 11a). The corresponding droplet trajectories computed with the numerical model as a function of the nozzle vertical tilt angles are depicted in Figure 11b.



(a)



(b)

Figure 11 (a) Comparison of droplet radial distances computed, with the numerical and analytical models, as a function of sprinkler nozzle vertical tilt angle and (b) droplet trajectories as a function sprinkler vertical tilt angle

It can be noted that the maximum elevation that the droplet reaches increases with the vertical tilt angle, but the radial distance initially increases with the tilt angle, attains it maximum at 45° and

then decreases. Although the nozzle vertical tilt angle of impact sprinklers is typically less than 27° (e.g., von Bernuth, 1988) and that the scenario of droplet motion considered here represents a simpler problem than that occurring under field conditions, the fact that the numerical and analytical solutions for different sets of conditions compare well suggests that the representation, in the numerical model, of the physics underlying droplet dynamics is sound.

6.2 Wind effects on droplet motion, simulation based analysis

Given a droplet diameter, set of initial conditions, pertinent physical parameters of the ambient air, and wind velocity vector, accurate prediction of droplet trajectories and radial landing distances requires that the scale factors (model parameters), introduced to take into account the effect of wind on droplet drag and drift (Section 3.2), be known. The determination of these parameters, for a droplet, based on measurements is unrealistic in the context of this study. Hence, the objective here is limited to drawing qualitative inferences on model performance based on comparisons of simulated patterns of droplet motion, as affected by wind, with expectations stemming from physical and intuitive reasoning.

Simulations were conducted for combinations of five droplet diameters (in the range 0.2mm to 3.0mm), wind speeds of 1.25m/s and 2.5m/s, and six levels of wind vector azimuth (in the range 0° to 270°). This results in five simulations for each wind velocity vector and a total of sixty simulations in all (Figure 12 and 13). The input dataset used in the simulation examples is summarized in Table 2 (dataset III). For all the simulation examples, the initial conditions and pertinent physical parameters of the ambient air are set at the same level. The angular setting of the sprinkler nozzle is 0° from the reference axis, which is taken to be the longer axis of the horizontal plane (Figures 12 and 13). The wind vector azimuth is measured with respect to the shorter axis of the horizontal plane. The parameter set used in the simulation examples are arbitrary, in the sense that they are not the product of a model calibration process, although they are within the range considered realistic (Section 6.3.2). Two yardsticks considered here for measuring the effect of wind on droplet motion are droplet wind drift and radial distance of droplet landing point from the sprinkler. Droplet radial distance from a sprinkler can easily be calculated given the droplet landing coordinates. On the other hand, wind drift effect in the context of sprinkler irrigation is often described as wind induced distortions on sprinkler

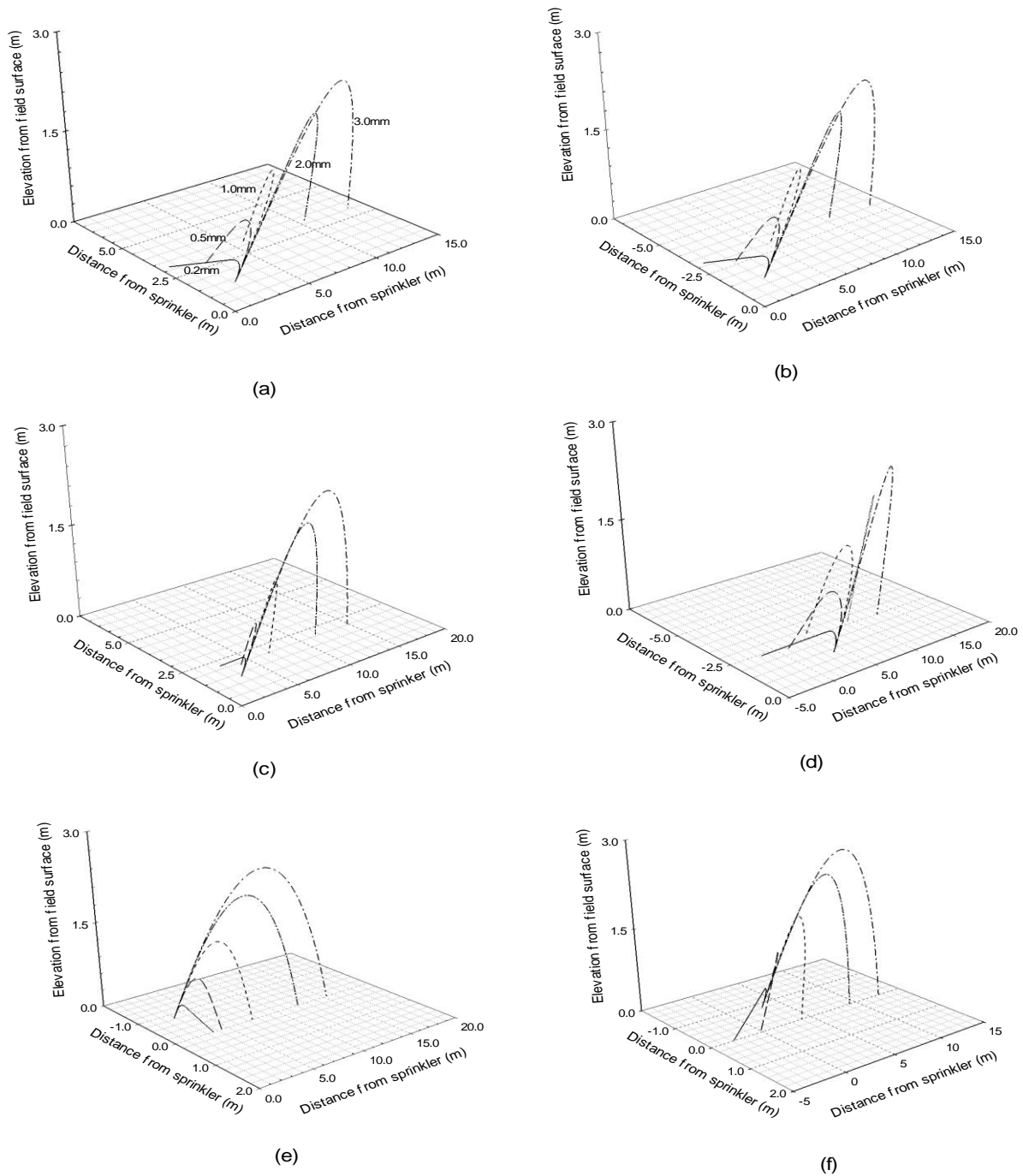
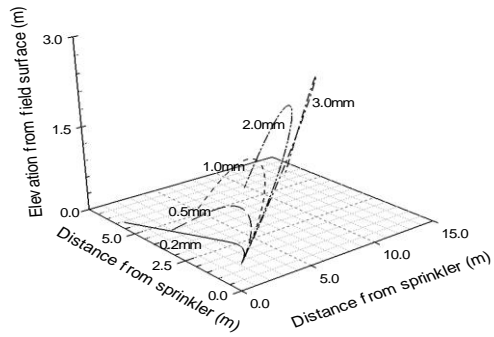


Figure 12 Droplet trajectories for wind speed of 1.25m/s and wind vector azimuth of: (a) 0° , (b) 180° , (c) 45° , (d) 225° , (e) 90° , and (f) 270° (The reference axis for measuring the angular setting of the sprinkler nozzle is the longer horizontal axis, note that the positive and negative algebraic signs in axis labels are meant to emphasize that distance measurement were made in opposite spatial direction from the origin of the coordinate system)

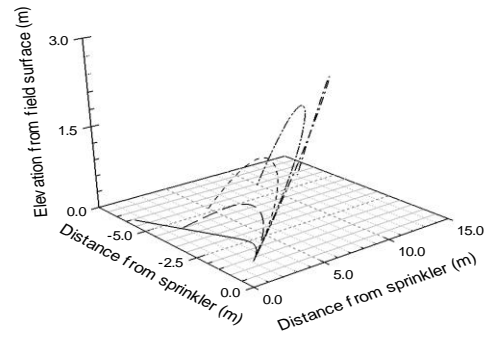
irrigation precipitation pattern relative to that associated with an equivalent no-wind condition. However, the concept of droplet wind drift can be more subtle. In principle, any wind induced deviation in droplet trajectory, which could have both horizontal and vertical components, from an equivalent no-wind condition can be considered droplet wind drift (Zerihun and Sanchez, 2014b). In order to simplify the concept for practical application, here droplet wind drift is quantified simply as the perpendicular distance on the horizontal plane between droplet landing point and the projection on horizontal plane of the sprinkler nozzle centerline. Hence, for the current simulation examples, in which the angular setting of the sprinkler nozzle is 0° from the reference axis, droplet drift is then equal to the coordinate of the droplet landing point on the shorter axis.

Values of wind vector azimuth considered in the simulation examples include 0° and 180° , which represent conditions whereby the projection on the horizontal plane of the droplet initial absolute velocity vector is orthogonal to the wind velocity vector. All things being equal, for a given droplet diameter these values of wind vector azimuth should result in maximum drift. At the opposite end of the range is a scenario with a wind vector azimuth of 90° and 270° , which represent conditions where the projection on the horizontal plane of the droplet initial absolute velocity vector is collinear with the wind velocity vector, hence droplet drift as defined above should be zero. Considering the relatively small vertical tilt angle of sprinklers, for a given droplet diameter the scenario with wind vector azimuth of 90° should result in minimum drag, hence maximum droplet radial landing distance from the sprinkler and the opposite should be true for a condition in which the wind vector azimuth is 270° . An intermediate scenario consists of wind vector azimuth of 45° and 225° . This represents two wind velocity vectors, with the same line of action but opposite sense, making a 45° angle with the horizontal component of the droplet initial absolute velocity vector. It can be noted that for wind vector azimuth of 45° and 225° , during the initial phase of droplet motion wind effects on droplet motion are nearly equally divided between drag and drift. As will be discussed in subsequent sections this has an effect on the relative magnitudes of droplet drift and radial landing distances from the sprinkler.

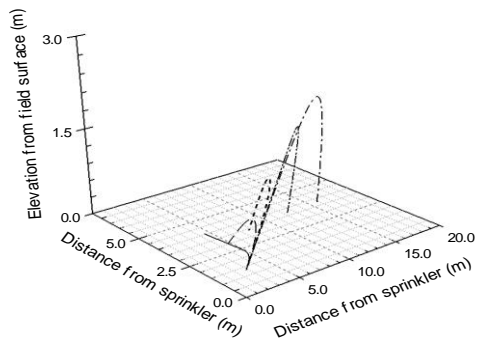
Evidently, the direction and magnitude of the component of the wind velocity vector normal to the droplet absolute velocity vector changes continuously with time (may note discussion on this in the accompanying document). However, droplet wind drift should have the



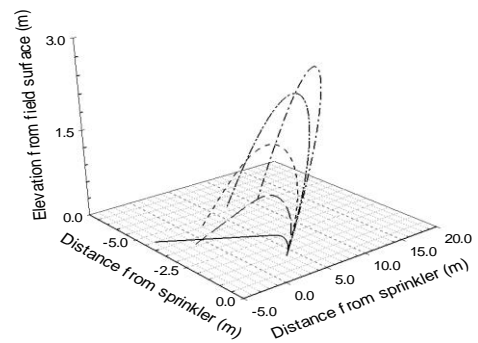
(a)



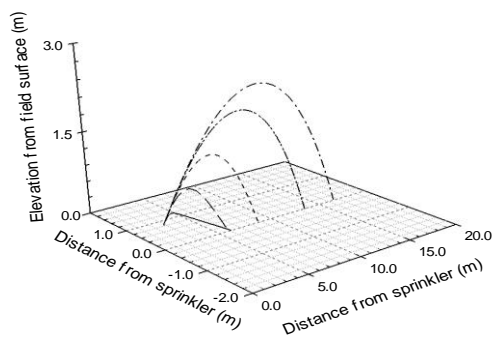
(b)



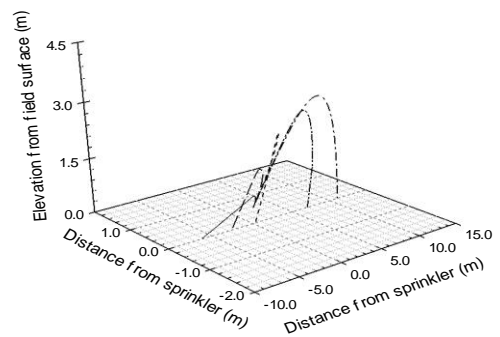
(c)



(d)



(e)



(f)

Figure 13 Droplet motion for wind speed of 2.5m/s and wind vector azimuth of: (a) 0° , (b) 180° , (c) 45° , (d) 225° , (e) 90° , and (f) 270° (The reference axis for measuring the angular setting of the sprinkler nozzle is the longer horizontal axis, note that the positive and negative algebraic signs in axis labels are meant to emphasize that distance measurement were made in opposite spatial direction from the origin of the coordinate system)

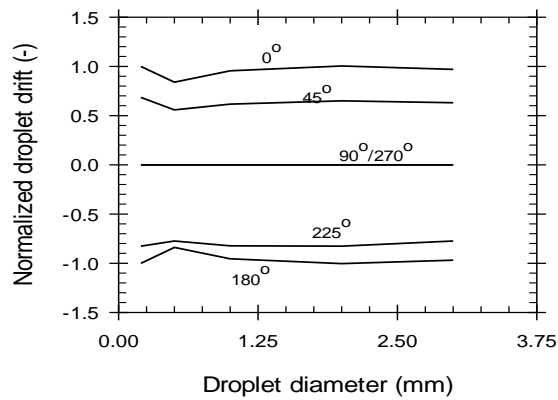
same general direction as the component of the wind velocity vector normal to the projection on the horizontal plane of the droplet initial absolute velocity. Hence considering wind vector azimuths of 0° , 45° , 180° , and 225° and the angular setting of the sprinkler nozzle, it can be noted from the simulation results summarized in Figures 12 and 13 that droplet wind drift directions for all the scenarios is consistent with physical reasoning. For wind vector azimuths of 90° and 270° (Figures 12e, 12f, 3e, and 13f), the model prediction shows that droplet wind drift is zero and droplet motion is (planar) confined to the vertical plane containing the centerline of the sprinkler nozzle, which is in line with expectations stemming from physical reasoning. It can be noted from Figures 12 and 13 that for any given droplet diameter the wind drift produced by 2.5m/s wind speed is invariably larger than that produced by the smaller wind speed of 1.25m/s, which is consistent with expectation based on intuitive physical reasoning.

It can be noted from Figures 12f and 13f that the finer droplets (0.2mm and 0.5mm) move backwards with respect to the initial droplet velocity vector. Considering that initial conditions for all droplets are the same, it follows that at the sprinkler nozzle droplet kinetic energy per unit volume is also the same for all droplets. However, drag per unit volume increases with a decrease in droplet diameter, because of the associated increase in droplet specific surface area, which affects the empirically determined steady state drag coefficient. This implies that the initial kinetic energy of finer droplets can be dissipated by a larger drag to such an extent that the droplet horizontal velocity component becomes nearly zero at relatively short distances from the sprinkler. Hence, in accordance with the computational framework implemented in the model described here (Section 3.5), once the horizontal component of droplet absolute velocity falls to zero, droplet is assumed to be fully carried by the ambient air. In which case the direction of droplet motion is reversed and droplet assumes a horizontal velocity equal to the wind velocity. To the extent that droplet motion is confined to the vertical plane containing the nozzle centerline, considering the description given above for droplet wind drift, this form of droplet motion is not considered here as wind drift.

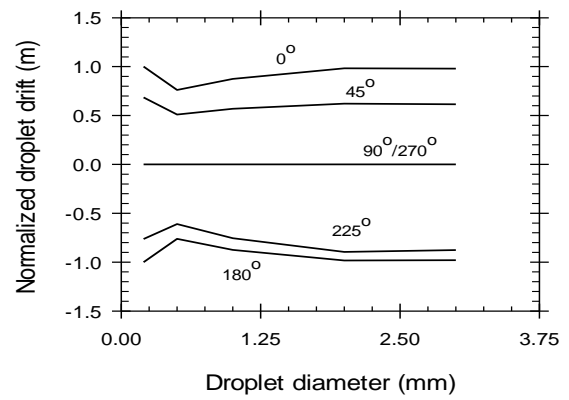
In order to further examine patterns of droplet motion, as affected by wind, on quantitative basis, droplet wind drift and droplet radial landing distance from the sprinkler are expressed in terms of three dimensionless parameters and the results are summarized in Figure 14. The dimensionless

parameters are defined as follows: (i) *Normalized droplet drift*: for a given wind velocity vector and droplet diameter combination, the normalized droplet drift is computed as the ratio of the droplet wind drift to the maximum droplet drift associated with the given wind speed (Figure 14a and 14b). Given wind speed and droplet diameter, this parameter is considered here to be particularly useful in evaluating the sensitivity of droplet drift to wind vector azimuth; (ii) *Drift ratio*: for a given wind velocity vector and droplet diameter, the drift ratio is computed as the quotient of droplet drift and droplet radial landing distance from the sprinkler (Figure 14c and 14d). Considering a given wind velocity vector, this parameter is considered here to be useful in quantifying the sensitivity of wind drift to droplet diameter; and (iii) *Normalized droplet radial distance*: for a given droplet diameter and wind velocity vector, the normalized droplet radial distance is calculated as the ratio of the droplet radial landing distance from the sprinkler to the maximum droplet radial distance associated with the given wind speed (Figure 14e and 14f). Given a droplet diameter, this parameter is useful in quantifying the sensitivity of droplet radial distances from the sprinkler to wind velocity vector.

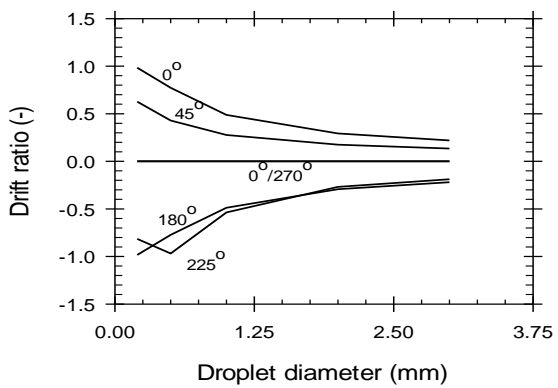
Graphs of the normalized droplet drift versus droplet diameter are shown in Figures 14a and 14b for wind speeds of 1.25m/s and 2.5m/s, respectively. For a given droplet diameter and wind speed, maximum wind drift (defined in terms of the normalized droplet drift) occurs when the wind velocity vector makes a 90° angle with the horizontal component of the droplet initial absolute velocity. Note that this corresponds with 0° and 180° wind vector azimuth. On the other hand, when the wind velocity vector is collinear with the projection on the horizontal plane of the droplet initial absolute velocity (wind vector azimuth of 90° and 270°) droplet drift becomes zero (Figures 14a and 14b). When the acute angle between the horizontal component of the droplet initial absolute velocity vector and the wind velocity vector is 45° (which correspond to wind vector azimuths of 45° and 225°), the normalized droplet drift curves fall between those obtained for 0° and 180° wind vector azimuths (Figures 14a and 14b). Note that these observations are consistent with intuitive physical reasoning. As would be expected, the normalized droplet drift curves associated with wind vector azimuths of 0° and 180° are mirror image of each other (they exhibit symmetry about the zero drift line, Figures 14a and 14b). This,



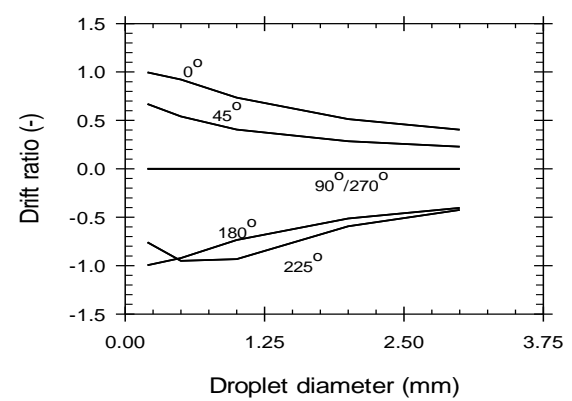
(a)



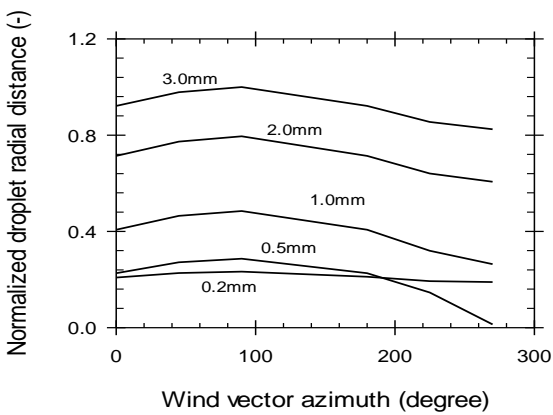
(b)



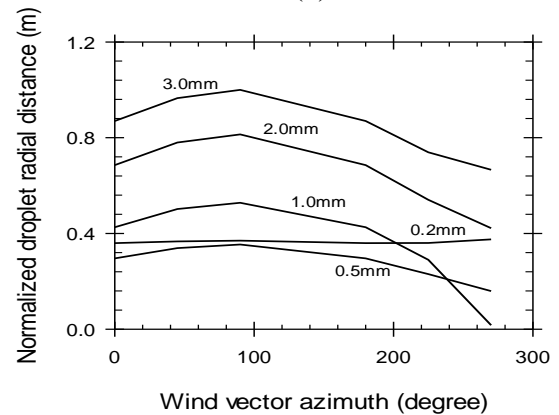
(c)



(d)



(e)



(f)

Figure 14 Droplet drift and radial landing distances: (a) Normalized droplet wind drift as a function of droplet diameter for wind speed of 1.25m/s, (b) Normalized droplet drift as a function droplet diameter for wind speed of 2.5m/s, (c) Drift ratio as a function of droplet diameter for wind speed of 1.25m/s, (d) Drift ratio as a function of droplet diameter for wind speed of 2.5m/s, (e) Normalized droplet radial distance as a function wind vector azimuth for wind speed of 1.25m/s, and (f) Normalized droplet radial distance as a function wind vector azimuth for wind speed of 2.5m/s

however, is not the case for azimuths of 45° and 225° . Instead droplet drift for wind vector azimuth of 225° is larger than that observed for 45° . It can be shown that in both cases the effect of wind during the initial part of droplet motion is nearly equally split between drag and wind drift. However, for wind vector azimuth of 45° the effect of wind on drag is to diminish it, whereas the opposite is true when the wind vector azimuth is 225° . Although the direct effect of this is to reduce droplet radial distance for the case in which wind vector azimuth is 225° , a review of the droplet trajectory data shows that it also has an effect on droplet velocity and duration of droplet motion. Droplet velocity remains higher and the corresponding duration of droplet motion shorter for the scenario in which wind vector azimuth is 45° compared to that of 225° . The implication is that for a given wind speed a droplet of given diameter will be subjected to wind drift effects for a longer duration when wind vector azimuth is 225° than is the case for 45° , which may, to a certain extent, explain the observed difference in the normalized droplet drift for these wind vector azimuths.

Considering Figures 14a and 14b, it can be noted that for each value of the wind vector azimuth there are two segments, a segment ranging from 0.2mm droplet diameter to 0.5mm in which the normalized droplet drift shows a slight decrease from the maximum value and a second segment for droplet diameters varying between 0.5mm and 3.0mm, where droplet drift rises slightly and then levels-off. The difference in slope in the two segments of the curves is related to the different physical mechanisms driving droplet motion and their mathematical representation in the model (Section 3.5). For both 1.25m/s and 2.5 m/s wind speeds, the motion of the droplet with 0.2mm diameter is dominated by a mechanism in which droplet is fully carried by wind. As will be discussed subsequently, that in fact is the case for the droplet with 0.5mm diameter as well under a wind velocity vector of 2.5 m/s and 270° azimuth.

The droplet drift ratio expressed as a function of wind vector azimuth and droplet diameter is depicted in Figures 14c and Figure 14d for wind speeds of 1.25m/s and 2.5m/s, respectively. It can be noted that for a given wind velocity vector, drift ratio is generally inversely related to droplet diameter. This implies that wind drift relative to droplet radial distance decreases as droplet diameter increases, which is a physically reasonable result. An interesting result is that the drift ratio curves for the different wind vector azimuths converge asymptotically to the zero

drift line with increases in droplet diameters (Figure 14c and 14d). However, the rate of convergence of the curves, with increase in droplet diameter, is lower for the scenario in which wind speed is 2.5m/s compared to that of 1.25m/s. The implication is that, all things being equal, wind drift effects attenuate at a faster rate, with increases in droplet diameter, for the lower wind speed than is the case for the higher wind speed, which is a physically plausible observation. Note that the relatively larger drift ratio associated with wind vector azimuth of 225° compared to that of 180° , does not imply that wind drift associated with wind vector azimuth of 225° is larger than that of 180° . Instead it indicates that the ratio of droplet drift to droplet radial landing distance is larger for the case in which wind vector azimuth is 225° . This could possibly be explained by the fact that, for the case in which wind vector azimuth is 225° , wind effects are at least initially, nearly equally, divided between drag and drift and that the effect of wind on drag is to increase it – which leads to a decrease in droplet radial distance from sprinkler. The net result being a relatively larger droplet drift ratio.

The graphs showing the normalized droplet radial distance, expressed in terms of droplet diameter and wind vector azimuth, are given in Figure 14e and Figure 14f for wind speeds of 1.25m/s and 2.5m/s, respectively. For a given droplet diameter and wind speed the maximum droplet radial distance corresponds to wind vector azimuth of 90° and the minimum droplet radial distance corresponds to a wind vector azimuth of 270° . Noting that the wind velocity and the horizontal component of the droplet initial absolute velocity vectors are collinear and have the same sense (for 90° azimuth) and opposite sense (for 270° azimuth), it becomes evident that these results are consistent with physical reasoning. The normalized droplet radial distance decreases, with increases in the wind vector azimuth in the range 90° to 270° and, it increases in the range 0° to 90° azimuth. Note that these observations are consistent with the changes in the relative magnitudes of the components of the wind velocity vector associated with the variations in the wind vector azimuth. The rate with which normalized droplet radial distance decreases, with increases in wind vector azimuth between 90° and 270° , is faster for wind speed of 2.5m/s than is the case for 1.25m/s.

Considering a droplet motion entirely driven by the initial impulse at the sprinkler nozzle, for any given wind vector azimuth the normalized droplet radial distance should be

monotonically decreasing function of droplet diameter. It can be noted from Figures 14e and 14f that in fact is the case for droplet diameters ranging between 0.5mm-3.0mm under wind speed of 1.25m/s. For a wind speed of 2.5m/s the same pattern can be noted for droplet diameters of 1.0, 2.0, and 3.0mm over the entire wind vector azimuth range and for droplet diameter of 0.5mm in the wind vector azimuth range of 0°-225°. As described above for the finer droplets the dominant form of droplet motion consists of one in which droplets were fully carried by wind, hence the radial curves for these droplets deviate from the pattern observed for the larger droplets.

6.3 Model evaluation with measured data and potential field-scale application

This section presents an evaluation of the numerical model through comparisons with measured data. Two groups of datasets collected during single sprinkler tests conducted (1) in indoor settings and (2) under field conditions were used in the evaluation. Description of the layouts of the sprinkler apparatuses used in the indoor and field evaluations, data collected, and results of model calibration and evaluation are presented subsequently.

6.3.1 Indoor single sprinkler tests, datasets, and model evaluation

A series of single sprinkler tests were conducted in an indoor facility in the Maricopa Agricultural Center (MAC) of the University of Arizona. The goal of the indoor tests was to determine the sprinkler radial application rate patterns, based on which droplet diameter ranges, droplet size discretization steps, corresponding droplet volumetric application rates, and sprinkler wetted radius are estimated (Sections 4.2.1 and 4.3.1).

Description of the apparatus used in the single-sprinkler indoor tests

The layout of the indoor test apparatus and its components are depicted in Figure 15. The main elements of the system consist of a buffering tank, a suction pipe, a pump, a discharge pipe, a sprinkler mounted on a riser pipe, a return flow pipe, a flow meter, and pressure gages. The sprinkler used in the indoor irrigation evaluations is a WeatherTec 10-20 model with nozzle diameter of 3/32". It is mounted on a 0.53m riser pipe, which in turn is installed at the downstream end of a 15.2m long pipe, on the discharge side of a high head low capacity booster

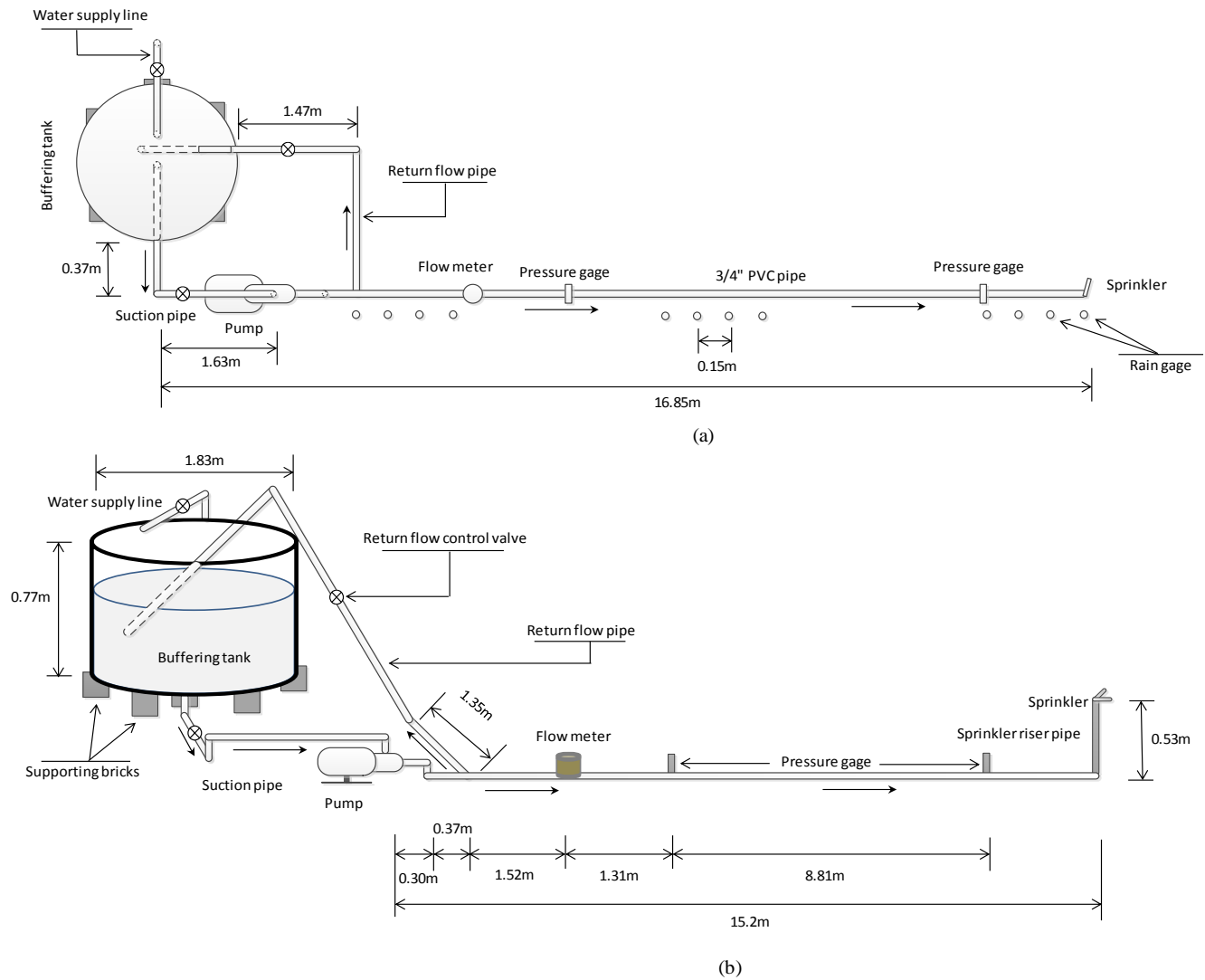


Figure 15 A sketch of the layout of the single sprinkler indoor test apparatus: (a) plan view and (b) isometric view

pump. The pump obtains its supply from a buffering tank through the suction pipe, the offtake point of which is at the bottom of the tank (Figure 15). The tank in turn is supplied from a local water system. A 3/4" diameter PVC pipe was used on the suction and discharge side of the pump as well as for the return flow section. The steady state sprinkler discharge was measured with a flow meter (0.1Gallon precision) installed on the discharge pipe (Figure 15). In addition, two pressure gages with a precision of 2.0psi (1.406m water column) were installed between the pump and the sprinkler. The return flow pipe section connects the discharge pipe with the buffering tank and is equipped with a return flow control valve. It provides the mechanism for controlling the sprinkler discharge, and hence pressure head, which is accomplished by throttling the return flow control valve as desired. The dimensions of the system components are shown in Figure 15.

Precipitation depths along a wetted radius of the sprinkler are measured with 50 rain gages installed along the discharge pipe at 0.3m spacing (Figure15). The rain gages were obtained from the Irrigation Training & Research Center of the California Polytechnic State University, San Luis Obispo, CA. The rain gages have a catchment area of 104.84cm² and are graduated in 5.0ml increments up to a 100.0ml volume. Assuming a volumetric reading error of ± 1.0 ml, the corresponding measurement precision in depth units would be about 0.1mm. For volumetric measurements ranging between 100.0ml and 200.0ml, the rain gages are graduated in 25.0ml increments. Considering ± 5.0 ml volumetric reading error, the corresponding precision in depth units is about 0.5mm. Considering that more than 95.0% percent of the measurements for the indoor single tests and all of the measurements for the field tests are smaller than 100.0ml, a measurement precision of 0.1mm can be assumed in subsequent discussion.

Data description

Measured radial application rate: Each of the single-sprinkler indoor tests were conducted for a duration of 3.0h. During an evaluation the test sprinkler was operated under a steady nozzle pressure head of 40.0psi (28.1m), 50.0psi (35.2m), 60.0psi (42.2m), or 70.0psi (49.2m), Table 3. Note that these pressure head levels span much of the recommended range for the sprinkler used in the study: WeatherTec 10-20, nozzle size 3/32". In addition to pressure heads the steady state

nozzle discharges were also measured during each evaluation. At the end of an evaluation, depths collected in the rain gages were recorded and sprinkler radial application rates were computed based on the measured depths and irrigation duration.

Four of the datasets from the indoor tests were used in model evaluation. The measured radial application rates for these datasets are depicted in Figure 16. The measured wetted radius vary between about 10.5m for sprinkler pressure head of 49.2m and 11.7m for sprinkler pressure head of 42.2m, with the wetted radius for sprinkler pressure heads of 28.1m and 35.2m being about 11.4m. The cutoff value, in terms of precipitation depth collected in rain gages, used for the determination of sprinkler wetted radius is 0.1mm (assumed precision of the rain gage). This implies that rain gages with precipitation depths less than 0.1mm are considered to have received no precipitation.

Table 3 Datasets from indoor single sprinkler tests used in model evaluation

<i>Variables</i>		<i>Unit</i>	<i>Dataset IV</i>	<i>Dataset V</i>	<i>Dataset VI</i>	<i>Dataset VII</i>
Time of irrigation evaluation	Date	-	11/05/2013	10/30/2013	11/02/2013	11/04/2013
	Time of day	Start	2:20PM	11:00AM	9:42AM	10:50AM
		End	5:20PM	2:00PM	12:42PM	1:50PM
	Duration	<i>H</i>	3.0	3.0	3.0	3.0
Sprinkler pressure head		<i>m (psi)</i>	28.1 (40.0)	35.2 (50.0)	42.2 (60.0)	49.2 (70.0)
Average temp		<i>°F</i>	72.1	68.9	75.5	75.3
Average dew point temp		<i>°F</i>	42.0	35.4	30.8	44.3
Average relative humidity		<i>%</i>	33.8	29.2	19.9	33.3
Av. vapor pressure deficit		<i>kPa</i>	1.8	1.7	2.5	2.0
Wetted radius		<i>M</i>	11.4	11.4	11.7	10.5
Spray evaporation fraction		-	0.36	0.34	0.3	0.33
Cubic polynomial parameters (curve fit)	Constant	<i>Mm/h</i>	2.887	2.8217	3.4593	3.3013
	Linear term	<i>mm/m/h</i>	-1.3612	-1.3181	-1.5127	-1.3208
	Quadratic term	<i>mm/m²/h</i>	0.2084	0.2092	0.2341	0.2197
	Cubic term	<i>mm/m³/h</i>	-0.0095	-0.01	-0.0112	-0.0117

Sprinkler nozzle height = 0.53m, sprinkler vertical tilt angle = 23°; sprinkler nozzle diameter 2.381mm; the coefficient and exponent of sprinkler head-discharge function are 0.0000157 and 0.522, respectively.

Overall based on the datasets presented here and those not used in model evaluation, two distinct radial application patterns can be discerned for the sprinkler used in the study (Figure 16). For all the datasets the maximum application rate occurs at the sprinkler location and then it decreases rapidly with distance from sprinkler. However, when the sprinkler is operated at the relatively lower and intermediate pressure heads (28.1m and 35.2m), the middle section of the radial application rate curve initially continues to decrease with distance from sprinkler, but at a decreasing rate. It attains its minimum about half-way through the sprinkler wetted radius, referenced from the sprinkler location, and then begins to increase. Near the edge of the sprinkler wetted area the curve levels-off and then falls rapidly to zero. For the larger pressure heads (42.2m and 49.2m) the application rate patterns near the sprinkler and at the far end, close to the edge of the wetted area, are similar to those for the relatively lower pressure heads. On the other hand, the middle sections of the radial application rate curves for pressure heads of 42.2m and 49.2m are relatively flat compared to those obtained for lower pressure heads (28.1m and 35.2m). The dip in the middle section of the application rate curves, for the lower sprinkler pressure heads (which increases with a decrease in pressure head, Figures 16a and 16b), is consistent with the so-called donut shaped application pattern described in the literature for sprinklers operated at relatively lower pressure heads than is optimal (Keller and Bliesner, 1990).

Figures 16a-16d depict two additional curves superimposed on the measured radial precipitation pattern. The dashed lines represents a cubic polynomial fit to the measured sprinkler radial application rate data with a coefficient of determination, r^2 , greater than 0.91 (Table 3). As will be discussed in subsequent sections, the regression functions are used as model input to specify sprinkler radial application pattern at a given nozzle pressure head and the dashed lines, on the other hand, represent simulated application rate curves.

Computation of spray evaporation losses: Weather data pertinent to spray evaporation losses, representing outdoor conditions, during the irrigation evaluations were obtained from a nearby AZMET station: <http://ag.arizona.edu/azmet>. The data consists of average temperature, dew point temperature, relative humidity, and vapor pressure deficit (Table 3). Evidently temperature in the indoor test facility could be slightly higher than the outdoor condition, while humidity should be appreciably higher; nonetheless, the outdoor weather data can be indicative of the

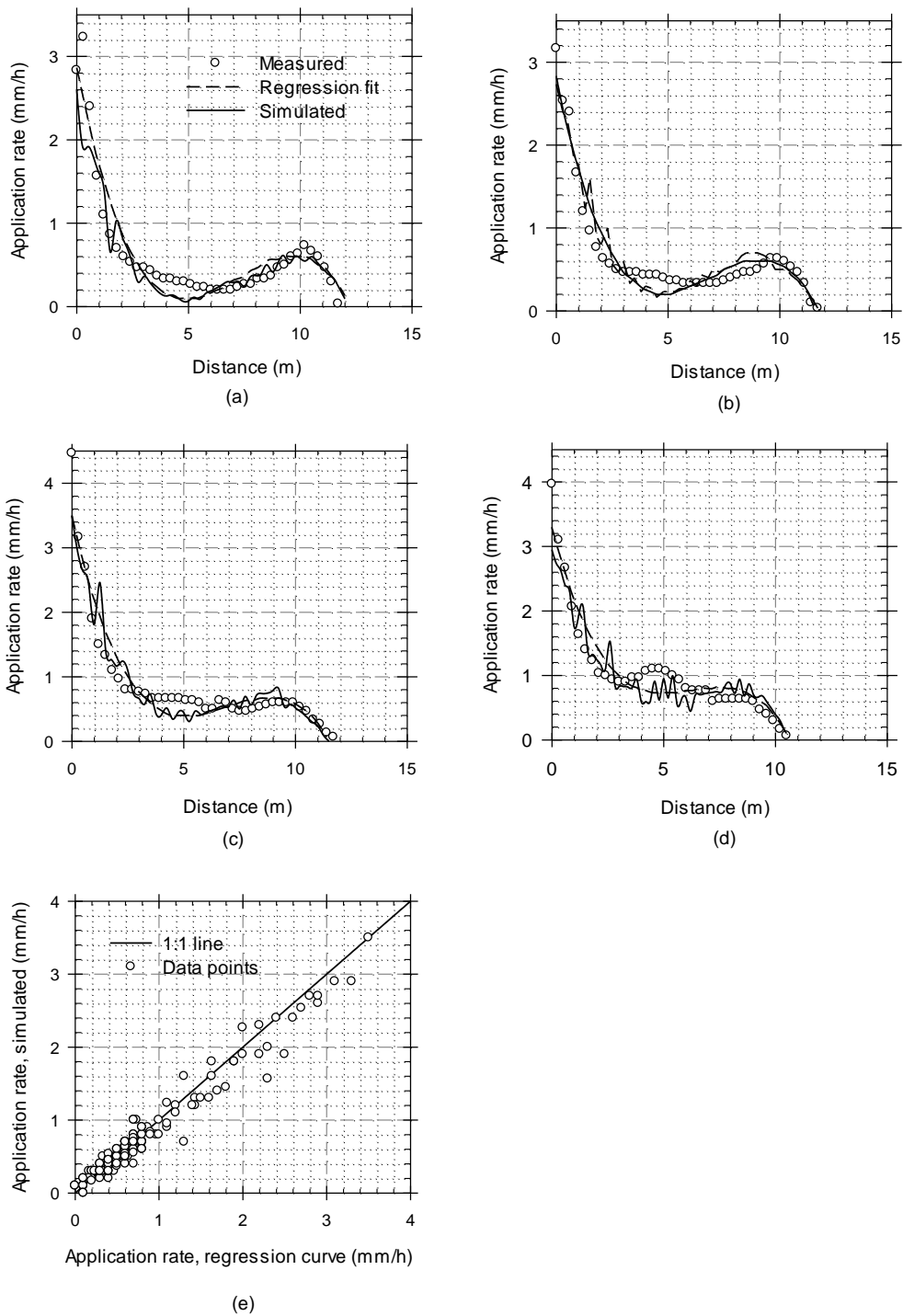


Figure 16 A comparison of sprinkler radial application rates (obtained through indoor measurements, regression fit, and simulated) for sprinkler pressure head: (a) 28.1m (40.0psi), (b) 35.2m (50.0psi), (c) 42.2m (60.0psi), (d) 70.0m (49.2psi), and (e) Aggregate comparison of simulated radial application data with regression fit

conditions under which the tests were conducted. Noting that the tests were conducted indoors, wind drift losses are considered zero. Spray evaporation losses can then be computed through mass balance calculations as a function of volume applied and volume collected. Volume applied can be computed as a function of sprinkler steady state discharge and duration of test. Volume collected over the wetted area of the sprinkler can be computed as a function of depths collected in each rain gage and the corresponding annular ring of irrigated area (Section 4.2.1).

As can be noted from Table 3, on average about a third of the applied volume was lost to spray evaporation, with a range of variation about the mean being $\pm 3.0\%$. Minimum spray evaporation loss fraction of 0.30 is obtained for dataset VI and a maximum fraction of 0.36 is computed for dataset IV (Table 3). With spray evaporation loss fraction of 0.34 and 0.33 each obtained for datasets V and VII, respectively. These results suggest that the prevailing microclimate in the indoor facility may not have been significantly different between the tests as the outdoor weather data suggests. The fact that spray evaporation losses computed for outdoor evaluations closely follow trends in the measured outdoor weather data (Section 6.3.2), lends some credence to the preceding observation on the temperature and humidity conditions under which the indoor tests were conducted. It should also be noted that other factors such as variations in droplet size distribution associated with different nozzle pressure heads as well as flow measurement and sampling errors may, to a certain extent, contribute to the variations in the computed spray evaporation fractions in manners not considered here. Note that the reference to sampling errors here relates to the question of: Is the spacing between rain gages sufficiently small for the depth collected in a rain gage to be considered a representative average sample of precipitation over the entire area of the corresponding annular ring (Section 4.3.1)?

Model evaluation under no-wind condition

Model evaluation under no-wind condition is based on a comparison of the simulated and measured sprinkler radial application rate patterns. Such a comparison allows us to test an important hypothesis on which the numerical algorithm of the sprinkler precipitation pattern simulation model is based, which can be summarized as: given sprinkler radial application rate data measured under no-wind condition, sprinkler specification, nozzle coordinate in a selected

coordinate system, and nozzle pressure head; the model can generate a symmetric precipitation pattern about a sprinkler with a radial application rate that closely matches measurement.

As mentioned above the measured radial application rate pattern, associated with a given nozzle pressure head, is specified at the input in terms of the parameters of the regression functions given in Table 3. Additional model inputs consist of physical properties of air pertinent to droplet dynamics modeling (air density and viscosity), model parameters relating to wind condition and unsteady motion of droplets, sprinkler design factors, sprinkler pressure head-discharge relationship, minimum droplet size, spray evaporation rate, and numerical discretization parameters (Table 4). Air density vary as a function of temperature, atmospheric pressure (related to altitude), and humidity. Kinematic viscosity of air increases with temperature and could conceivably be a function of humidity as well. However, in the study reported here density and viscosity parameters used in model evaluation are those of standard condition (20°C and 1.0atm, and dry air). Considering the low altitude of the evaluation site (about 350.0m above mean sea level) and the mean air temperatures during the irrigation evaluations (Table 3), which were sufficiently close to the standard temperature (20°C or 68°F), such an approximation is deemed acceptable here. Future studies may explore the sensitivity of model output to the

Table 4 Input data used in model evaluation, single-sprinkler indoor tests

<i>Variables</i>	<i>Unit</i>	<i>Dataset IV</i>	<i>Dataset V</i>	<i>Dataset VI</i>	<i>Dataset VII</i>
Density of air	kg/m^3	1.205	1.205	1.205	1.205
Kinematic viscosity of air	m^2/s	0.0000151	0.0000151	0.0000151	0.0000151
Scale factor for wind effects on drag	-	0	0	0	0
Scale factor for wind effects on droplet drift	-	1.0	1.0	1.0	1.0
Drag correction parameter for acceleration effects	-	0.0	0.0	0.0	0.0
Minimum droplet diameter	m	0.0001	0.0001	0.0001	0.0001
Angular discretization step size	deg	0.5	0.5	0.5	0.5
Grid square size, model	m	0.25	0.25	0.25	0.2
Spray evaporation fraction	-	0.36	0.34	0.3	0.33
Sprinkler pressure head	$m (psi)$	28.1	35.2	42.2	49.9

Density and kinematic viscosity of air at standard conditions (20°C, 1.0atm, and dry air); sprinkler pipe rise height and specification are listed in Table 3

interactive effects of nonstandard atmospheric conditions, through their effect on air viscosity and density. In addition, the pressure head-discharge function of the sprinkler, used in model evaluation computations, relates measured nozzle pressure heads with corresponding discharges. The minimum droplet diameters were set based on computational considerations (Section 3.4.3), while keeping in view its effect on the simulated sprinkler radial application rate. Model parameters, relating to wind effects on droplet drag and drift, were set to appropriate values for no-wind condition. The drag correction parameter for droplet acceleration effects were those found to yield a good fit between simulated and measured radial application rates.

As described above, the simulated sprinkler radial application rates (dashed lines) are depicted in Figures 16a-16d, superimposed on the regression curves and measured datasets. The results show that the simulated data closely fit the respective regression curves. An aggregate comparison of the simulated radial application rate data with those of the regression curves, depicted in Figure 16e, also suggests a good agreement between the simulated data and data from the regression fit, with slight under prediction by the model close to the upper limit of the data range. The simulated sprinkler wetted radii are within 4.0% of the measured values and within 2.0% of the estimates obtained based on the regression curve. Considering that the measured radial application rate patterns are specified at the (model) input in terms regression curves (Table 3), the fact that the simulated patterns compare well with the regression curves suggest the model performance is satisfactory. It can be reasoned that a better fit can be obtained if the sprinkler radial application rate, used in the numerical computation, is directly interpolated from the measured data. Such a functionality will be implemented in the model in a follow up study.

The simulated radial application rate curves represent plots of the average grid square precipitation rates along a sprinkler wetted radius, hence may not necessarily be smooth (Figures 16a-16d). Experience with simulated data suggest that larger grid square sizes (about 0.5m and above) result in smooth application rate curve that fits well with the corresponding regression function in the distal half of the sprinkler wetted radius. However, computed radial application rates obtained with larger grid squares do not predict the high application rates near the sprinkler as well as those obtained with smaller grid squares. Note that this is consistent with the fact that the rate averaging is done over larger areas (grid squares), hence localized peaks and troughs are

smoothed out. At the same time the larger grid squares do not have the spatial resolution to capture the rapid increase in application rates near the sprinkler, hence resulting in under estimations of application rates there compared to grids with finer spatial resolutions. On the other hand, smaller grid square sizes (about 0.375m and lower) have the spatial resolution to yield radial application rate curves that track the regression functions well over the entire wetted radius of the sprinkler, hence used in the model evaluation computations performed here. The resulting curves, however, are more wiggly than those obtained with larger grid square dimensions (Figure 16).

6.3.2 Single sprinkler evaluations under field condition

Description of the apparatus used in the field tests

A replica of the apparatus used in the indoor sprinkler evaluations (Figure 15) was constructed for the field study conducted in the research farm of the Maricopa Agricultural Center of the University of Arizona. The layout of the system and its components are depicted in Figure 17 and are described in the preceding section. The major components of the system, including the sprinkler head, riser pipe, and pump were the same as those used in the indoor study. The objective of the field evaluation is to collect data on precipitation pattern about the sprinkler under field conditions, which (along with data from indoor sprinkler tests) will then be used in model calibration and evaluation. Precipitation pattern under wind is nonsymmetrical about the sprinkler, hence single sprinkler field evaluations require setting up a two-dimensional test-plot, with the test sprinkler placed at the geometric center of the evaluation plot. Figure 17 depicts the test-plot used in the field evaluation, covering a square area of 29.6m×29.6m, further subdivided into 324 grid units of 1.65m×1.65m each. A rain gage placed at the center of each grid square is used to measure the average precipitation depth in a grid square. The specifications of the rain gages used in the field study are described in Section 6.3.1.

Data description

A series of single-sprinkler field tests were conducted, with each test spanning a duration of 3.0h. Following the indoor evaluations, the test sprinkler was operated at four different

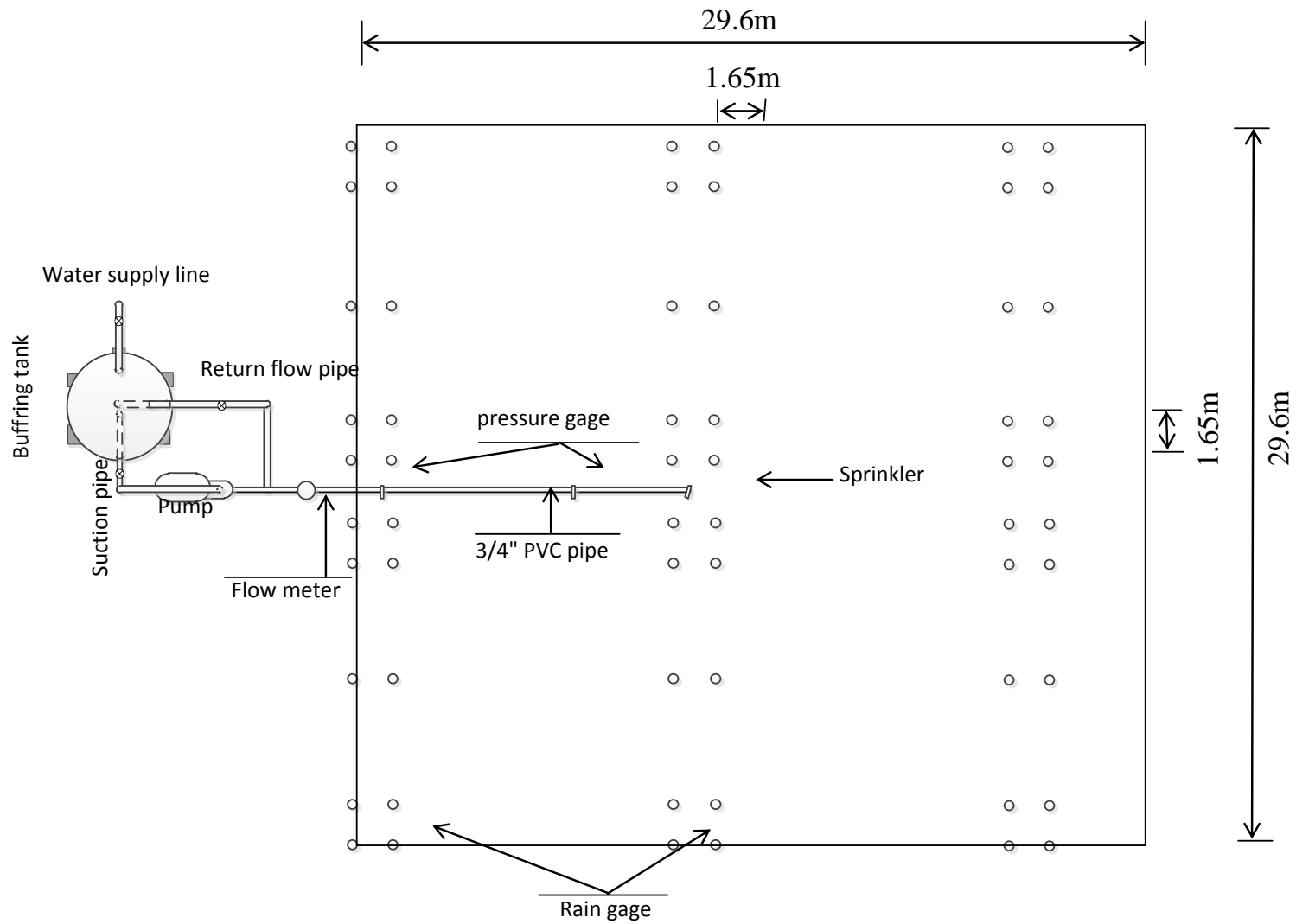


Figure 17 A sketch of the layout of the single sprinkler field test apparatus (plan view)

pressure heads: 28.1m, 35.2m, 42.2m, and 49.2m. During each irrigation evaluation the steady state pressure heads and discharges were measured. At the end an irrigation evaluation depths collected in the rain gages were recorded. A volume balance based approach is used to compute an estimate of the spray evaporation losses, as a function of applied volume and volume that reached the irrigated field surface.

The basic volume balance procedure used in the current study to compute spray evaporation losses consist of: *(i)* assuming the precipitation depth collected in a rain gage is a representative average of the corresponding grid square, an estimate of the volume of precipitation that fell in a grid square is computed as the product of the collected depth and the grid square area; *(ii)* aggregation of the volume collected in grid squares over the test-plot yields precipitation volume that reached the irrigated field surface, and *(iii)* an estimate of the spray evaporation loss is then computed as the difference between applied volume and the precipitation volume that reached the irrigated field surface. It is generally considered that a single sprinkler operating under field conditions exert a lower influence on the microclimate of the irrigation evaluation plot and its surrounding than a field-scale sprinkler system does over the irrigated field. This suggests that there may be a limitation to the transferability of spray evaporation estimates, derived based on single sprinkler field test, to field-scale applications. However, the significance of this limitation need to be established through further study. If the limitation of the approach is found to be significant, spray evaporation loss estimation based measured meteorological data may need to be explored.

Wind drift losses, defined here as a fraction of the applied volume that fell outside the test-plot, have occurred during some of the field evaluations conducted as part of this study. However, the datasets used in model evaluation are those with precipitation patterns completely contained within the test-plot. Hence, wind drift losses are considered negligible for these datasets.

Four of the datasets collected in the field tests are used in model calibration and evaluation. Wind velocity and related climatic data measured during the field evaluations are summarized in Table 5. Each dataset correspond to one of the four sprinkler nozzle pressure heads listed above. Pertinent weather data during the field tests were obtained from the local AZMET station, which include air temperature, dew point temperature, relative humidity, and

Table 5 Measured data during single sprinkler field evaluations

<i>Variables</i>		<i>Unit</i>	<i>Dataset VIII</i>	<i>Dataset IX</i>	<i>Dataset X</i>	<i>Dataset XI</i>
Time of irrigation evaluation	Date	-	11/12/2013	11/14/2013	11/19/2013	11/26/2013
	Time of day	Start	10:55AM	12:28PM	11:15AM	9:57AM
		End	-	1:55PM	3:28PM	2:15PM
	Duration		<i>h</i>	3.0	3.0	3.0
Hourly average wind speed	1 st hour	<i>m/s</i>	1.91	1.24	0.89	1.51
	2 nd hour		2.80	1.04	1.51	1.91
	3 rd hour		4.49	1.09	1.69	3.07
Hourly average wind vector azimuth	1 st hour	<i>deg</i>	170.0	316.0	108.0	160.0
	2 nd hour		218.0	259.0	132.0	178.0
	3 rd hour		245.0	217.0	137.0	243.0
Evaporation fraction		-	0.58	0.46	0.35	0.2
Average temp		<i>°F</i>	85.3	80.2	72.7	60.8
Average dew point temp		<i>°F</i>	35.5	43.5	46.4	44.8
Average relative humidity		<i>%</i>	17.2	27.4	39.3	56.8
Av. vapor pressure deficit		<i>kPa</i>	3.5	2.5	1.7	0.8

The steady state pressure heads under which the sprinkler was operated during each test and the sprinkler riser pipe height and specification are summarized in Table 3, the grid square size used in the field evaluations is 1.65m×1.65m.

vapor pressure deficit and the hourly average wind speed and direction. Considering the average air temperature, dew point temperature, relative humidity, and vapor pressure deficit during the irrigation evaluation, maximum spray evaporation should occur in the irrigation evaluation event in which dataset VIII was collected, while the weather data for dataset XI should represent the least favorable condition for spray evaporation. Datasets IX and X fall in between, with dataset IX representing a more favorable condition for evaporation compared to that of dataset X. It can be observed from Table 5 that the computed spray evaporation follows the pattern noted above based on weather data. In addition, it should also be mentioned that the wind speed for dataset VIII is significantly higher than the wind speeds associated the other datasets, which could have some impact on spray evaporation losses. Considering that spray evaporation is computed here with a volume balance approach, data on air temperature, dew point temperature, relative humidity, and vapor pressure deficit are included in Table 5 only to explain the observed spray evaporation pattern and for sake of data completeness. On the other hand, measured wind speed

and direction are essential inputs to the precipitation pattern simulation model. The hourly average wind data was used in model calibration and evaluation, instead of the average value for the duration of the test irrigation. This allows for wind effect on precipitation pattern to be specified with a high degree of temporal resolution. However, it also entails a requirement that wind related model parameters be specified for each wind speed and direction pair, resulting in increased complexity of parameter estimation. It also increases the computational time, because separate simulations need to be conducted for each hourly average wind velocity.

Model calibration

Model calibration here refers to estimation of pertinent model parameters: scale factor for wind effects on drag, ζ_1 , and droplet drift, ζ_2 , and empirical drag correction parameter for acceleration effects, ζ_3 (Eqs. 13-18). As highlighted in Section 4.2.2 model calibration is conducted through trial and error. The approach involves repeated runs of the model with different parameter sets and visual comparison of the simulated and measured precipitation depth contours and the corresponding three dimensional surfaces. Measured precipitation depths were obtained as part of the field evaluations described in the preceding section. The qualitative criteria used in comparing measured and simulated precipitation contours and surfaces are: resemblance of the patterns and areal extents of the simulated and measured precipitation contours and corresponding three dimensional surfaces as well as differences between the measured and computed maximum precipitation depths.

For each of the dataset used in model evaluation, the parameter sets (ζ_1 , ζ_2 , and ζ_3) that resulted in acceptable comparisons between the measured and computed precipitation patterns are summarized in Table 6. The values of the scale factor for wind effects on drag, ζ_1 , vary between the range 1.75, obtained for dataset IX, to 4.5 for Data set VIII. On the other hand, the scale factor for droplet drift, ζ_2 , varies between 0.2 and 3.5, obtained for datasets X and XI, respectively. The drag correction parameter for acceleration effects, ζ_3 , varies in the narrow range of -0.275 to -0.15. Experience with results of numerical simulation suggests that the effects of ζ_1 and ζ_2 on precipitation distribution about the sprinkler are correlated (see also Eq. 19). The

Table 6 Input data used in numerical model evaluation, comparison with field data

<i>Variables</i>		<i>Unit</i>	<i>Dataset VIII</i>	<i>Dataset IX</i>	<i>Dataset X</i>	<i>Dataset XI</i>
Density of air		kg/m^3	1.205	1.205	1.205	1.205
Kinematic viscosity of air		m^2/s	0.0000151	0.0000151	0.0000151	0.0000151
Scale factor for wind effects on drag (ζ_1)	1 st hour	-	4.5	4.0	2.0	2.5
	2 nd hour	-	4.5	1.75	2.0	3.0
	3 rd hour	-	4.5	1.75	3.0	4.5
Scale factor for wind effects on droplet drift (ζ_2)	1 st hour	-	1.75	1.5	0.2	1.5
	2 nd hour	-	2.0	0.3	0.25	2.5
	3 rd hour	-	3.0	0.3	0.5	3.5
Drag correction parameter for acceleration effects (ζ_3)		-	-0.275	-0.175	-0.15	-0.275
Minimum water droplet		m	0.0003	0.00068	0.0008	0.0006
Angular discretization step		deg	1.5	1.5	1.5	1.5
Grid square size, model		m	1.5	1.5	1.5	1.5
Evaporation fraction		-	0.58	0.46	0.35	0.2

Density and kinematic viscosity of air at standard conditions (20°C, 1.0atm, and dry air) and other pertinent data are given in Table 5

fact that these parameters are scale factors implies that they should generally be greater than zero. Preliminary results suggest that maximum values of both ζ_1 and ζ_2 may not exceed 5.0 and realistic precipitation patterns compatible with the predominant wind directions, during the evaluations, were obtained when $\zeta_2 < \zeta_1$. The exact relationship between droplet acceleration and unsteady drag in moderate to high Reynolds numbers, which include the range common in sprinkler droplet dynamics modeling, seem to be not well established (Temkin and Kim, 1980; Aggarwal and Peng, 1995). Hence, in principle there is no constraint in the algebraic sign of ζ_3 . As can be noted from Eq. 23, $\zeta_3 > 0$ implies the effect of droplet acceleration on the steady state drag coefficient is to increase it, while $\zeta_3 < 0$ results in reduced drag compared to an equivalent steady state condition. Simulation results have consistently shown that increasing ζ_3 , while keeping all other factors constant, results in a reduction in the areal extent of the precipitation pattern and a slight concomitant increase in the peak precipitation depth. On the other hand, decreasing ζ_3 has the opposite effect on precipitation distribution. Note that these observations are consistent with the effect of ζ_3 on the steady state drag coefficient described above. As can be

noted from Table 6, the ζ_3 values that yield computed precipitation patterns that compare favorably with the measured data are all negative. Although some physical meaning can be attributed to these parameters when they are used in the context of droplet dynamics, it ought to be stressed that, when considered in the context of precipitation pattern simulation about a sprinkler, the parameters are basically shape fitting constants.

For numerical simulation purposes, the test-plot is discretized into grid squares of $1.5\text{m} \times 1.5\text{m}$ matching closely the spatial resolution with which the field evaluation plot was discretized ($1.65\text{m} \times 1.65\text{m}$). Note that the droplet volumetric application rate is computed here based on the angular discretization steps given in Table 6. The minimum droplet diameters (Table 6) were set such that the resulting maximum precipitation depths were close to the field observed values. The minimum droplet diameters used for datasets IX, X, and XI are on the high side. Overall simulated maximum precipitation depths were significantly larger than field observed values, when the minimum droplet sizes are set to significantly smaller values than those given in Table 6. Field experience shows that even at moderate wind speeds (about 2.0m/s and lower) some fraction of the precipitation is carried by wind to considerable distances outside the irrigation evaluation plot in the form of mist. It is likely that finer droplets (perhaps those in the sub-millimeter scale) originating from the irrigation stream or formed through secondary atomization may account for much of this water. This might have contributed to the much more diminished peak and diffused precipitation distribution observed with the measured data compared to simulation results. The physical mechanism for this may not entirely be spray evaporation and it is possible that processes other than those considered within the current modeling framework are contributing factors. On the other hand, considering the calibration procedure used here (a trial and error approach to estimate seven parameters) the parameter estimates are evidently suboptimal. Hence, if model calibration is performed with optimization based inverse modeling functionality a more acceptable fit between simulated and measured precipitation patterns can be obtained, without the need to use a relatively higher minimum droplet diameters mentioned above. In any case, additional study is required to ascertain this.

Model evaluation

At the scale of an irrigated field a sprinkler irrigation system precipitation pattern represents the aggregate effects of sprinkler head design factors, system hydraulics, topographic and geometric factors as well as the ambient weather condition, including wind speed and direction. Assuming a precipitation rate less than irrigation application rate, ultimately it is this pattern that determines the field-scale irrigation performance: irrigation uniformity, efficiency, and the degree to which irrigation requirement is satisfied in any given irrigation event. Hence, a modeling capability for a field-scale sprinkler irrigation performance characterization (with potential applications in irrigation system design, management, and evaluation) requires coupling a field-scale sprinkler irrigation hydraulic modeling component with a submodule for sprinkler irrigation precipitation pattern simulation and a root-zone soil water balance subroutine. This implies that a functional evaluation of the sprinkler irrigation precipitation pattern simulation model, developed here, can be conducted by comparing measured and simulated field-scale irrigation performance, obtained for a system of overlapping sprinklers. Given the sprinkler layout and spacing, the field-scale precipitation pattern corresponding to a measured data can be generated by overlapping the single sprinkler precipitation distribution derived through field evaluation. For a given set of model parameters (Table 6) as well as sprinkler layout and spacing, the field-scale precipitation pattern and corresponding performance can be computed with the sprinkler precipitation pattern simulation model presented here.

A substantial simplification of the model evaluation process can be achieved if the following conditions are assumed: *(i)* nozzle pressure head is the same, throughout the irrigated field, as that used in the single sprinkler field tests and *(ii)* weather condition is the same as that of the field tests. With these simplifications in place model evaluation can be conducted on the basis of a single completely overlapped field-plot. A completely overlapped field-plot is, defined here, as a rectangular area circumscribed by four inner and twelve outer sprinklers arranged in the spatial configuration depicted in Figure 18, with an assumed sprinkler spacing of 10.0m×10.0m. Note that any given point within a completely overlapped plot receives precipitation from all the sprinklers it can potentially receive if it were situated in an irrigated field. Irrigation water distribution within such a field-plot is generally considered representative

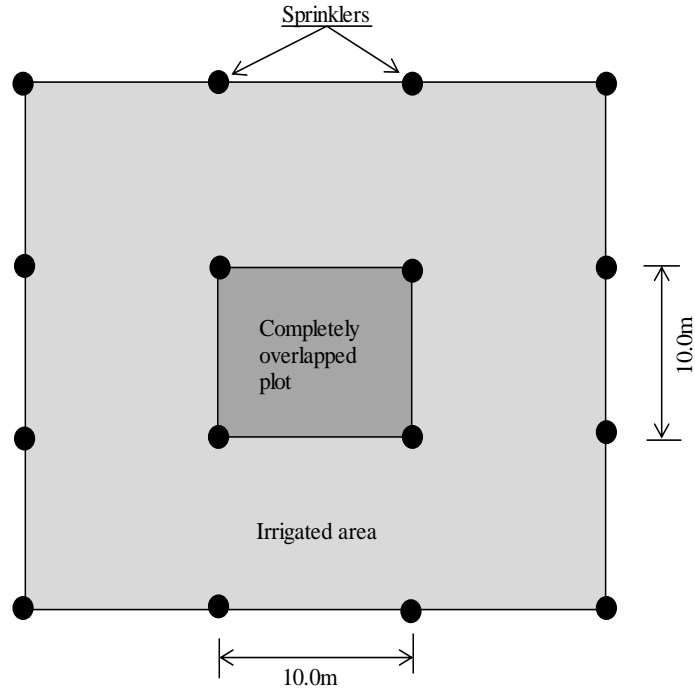


Figure 18 Layout of the overlapped sprinkler set used for model evaluation purposes

of a large fraction of a sprinkler irrigated field, except a narrow strip of land around the edges of the field. A similar sprinkler layout configuration was described by Playan et al. (2006) in the context of model evaluation. The irrigation performance index commonly used in such a context, and is used in the current study, is irrigation uniformity defined in terms of Christiansen's uniformity coefficient and low-quarter distribution uniformity. Hence, a comparison of irrigation uniformity along with average, minimum, and maximum collected depths over the completely overlapped plot, derived on the basis of the simulated and measured precipitation patterns, is used to evaluate the performance of the model developed as part of the current study.

The irrigation uniformity indices and irrigation depths for the completely overlapped plot (Figure 18) computed based on the measured and simulated precipitation patterns are summarized in Table 7. Note that the measured precipitation patterns used in model evaluation correspond to the datasets summarized in Table 6. For all the datasets the model predicted Christiansen's uniformity coefficient is within 4.7% of the *UCC* computed on the basis of the measured precipitation data, with the average error being 2.5% of the measured value. The maximum error between the simulated and measured low-quarter distribution uniformity is 7.2%

Table 7 Irrigation uniformity and depths computed based on measured and simulated precipitation patterns of the overlapped sprinklers

Data description		Parameters				
		UCC	DU_{lq}	D_{max}	D_{min}	D_{av}
		-	-	mm	Mm	mm
Dataset VIII	Measured	0.845	0.747	5.3	2.6	3.8
	Simulated	0.805	0.693	5.1	1.9	3.5
	Error (%)	4.7	7.2	3.8	26.9	7.9
Dataset IX	Measured	0.892	0.848	7	4.5	5.5
	Simulated	0.9	0.837	6.6	3.6	5.0
	Error (%)	0.9	1.3	5.7	20.0	9.1
Dataset X	Measured	0.864	0.782	8.7	4.5	6.9
	Simulated	0.829	0.737	9.8	1.5	7.0
	Error (%)	4.1	5.8	12.6	66.7	1.5
Dataset XI	Measured	0.86	0.77	12.4	6.6	9.4
	Simulated	0.862	0.795	13.5	5.4	8.9
	Error (%)	0.2	3.2	8.9	18.2	5.3
Average error	%	2.5	4.4	7.8	33.0	6.0

UCC = Christiansen's uniformity coefficient, and DU_{lq} = Low-quarter distribution uniformity; D_{max} = maximum depth collected, D_{min} = minimum depth collected, D_{av} = average depth collected, and

$$Error = \frac{|Measured - Simulated|}{Simulated} 100$$

of the measured value, while the average error is 4.4% of the measured DU_{lq} . The model was able to predict the maximum (D_{max}) and average (D_{av}) collected precipitation depths, for all the datasets, with maximum errors of 12.6% and 9.1%, respectively, of the measured depths. Average deviations of the simulated D_{max} and D_{av} from the measured values are 7.8% and 6.0%, respectively. The largest error between model prediction and field observation was obtained for the minimum collected precipitation depths, with a maximum of 66.7% for dataset X and an overall average of 32.9%. Overall the simulated irrigation uniformity as well as the average and maximum collected precipitation depths are in very good agreement with those computed based on field measurements. Model's prediction of minimum collected precipitation depths is rather poor. However, a close observation of the simulated precipitation depth data for dataset X, the data with the largest error between the simulated and measured D_{min} (66.7%), shows that if the collected precipitation depth data is arranged in ascending order the next larger value to the

minimum (1.5mm) is 4.8mm, which is within 6.7% of the measured D_{min} (4.5mm). This represents a tenfold reduction in error, which clearly illustrates that the minimum collected depth, being an extremum point in the data, is not necessarily indicative of the larger trend in the precipitation pattern, hence not as significant as the other parameters: uniformity indices and the average depth.

6.3.3 Potential application to field-scale sprinkler irrigation simulation and performance evaluation

The sprinkler irrigation precipitation pattern simulation model developed as part of the study reported here requires significant further development in terms of inverse modeling, numerical efficiency, a more specific definition of parameter ranges, development of modeling/field approaches that accounts for differences in microclimatic effects of irrigation under single sprinkler and field-scale conditions. In addition, improvements in the predictive accuracy of the droplet dynamics model that can potentially be realized by implementing a numerical solution of a form of the governing equation with a more rigorous physical basis, derived as part of this study (Zerihun and Sanchez, 2014b), may need to be examined. Evidently, these are outstanding issues that require further research. Nonetheless, results stemming from the limited study presented here (Section 6.3.2) and past studies (e.g., Vories et al., 1987; Playa et al., 2006) suggest that sprinkler irrigation precipitation pattern simulation models can estimate irrigation performance for a system of overlapping sprinklers with reasonable accuracy.

In order to highlight the potential application of the simulation model, developed here, in the determination of field-scale irrigation performance, a hypothetical scenario in which a solid set sprinkler irrigation system irrigates a rectangular field of 96.0m×174.0m is considered. The sprinkler system consists of a 5'' (127.0mm) mainline supplying water to ten equally spaced 2.5'' (63.5mm) laterals. The spacing between laterals is 10.67m (35.0ft). Twenty sprinklers mounted on riser pipes (0.53m high) are placed along each lateral at a regular spacing of 9.16m (30.0ft). The mainline is laid at a slope of 0.01% and the laterals are installed along a slope of 0.055%. Considering the same sprinkler as that used in the single sprinkler field evaluations and assuming a weather condition comparable to that observed for dataset XI (Table 5), it can be noted that pertinent (precipitation pattern simulation) model parameters are those derived for nozzle pressure head of 49.2m, which will henceforth be referred to as the calibration pressure head.

Given the field-scale spatial distribution of sprinkler pressure heads at the input, the precipitation pattern simulation model can generate the corresponding field-scale spatial distribution of irrigation depths (Section 4.3.2). A solid-set sprinkler irrigation hydraulic model, developed by the authors (Zerihun and Sanchez, 2014a), was used to simulate the field-scale spatial distribution of nozzle pressure heads. With a total dynamic head at the system inlet set at 150.75m, and an assumed elevation of 100.0m, the simulated maximum, minimum, and average nozzle pressure heads over the field are 50.0m, 48.8m, and 49.1m, respectively. This represents a maximum absolute deviation of 0.8m from the calibration pressure head (49.2m). The precipitation pattern simulation model parameters derived for the calibration pressure head are used for all the sprinklers in the field. The assumption is that field-scale variation in pressure head from the calibration pressure head is sufficiently small to induce appreciable deviation in sprinkler precipitation pattern from that obtained for the calibration pressure head.

The model output consists of a comprehensive set of field-scale irrigation performance indices: application efficiency, E_a , irrigation requirement index, I_r , and uniformity (UCC and DU_{lq}), along with average, D_{av} , maximum, D_{max} , and minimum, D_{min} , depths. The computed E_a is 66.7%, I_r is 0.848, and D_{av} is 9.1mm with D_{max} and D_{min} of 15.4mm and 4.6mm, respectively. Assuming that precipitation rates are less than soil intake rates, the computed precipitation depth at any given point in the field surface is partitioned into beneficial and deficit/excess fractions based on the field capacity approach. The simulated field-scale UCC and DU_{lq} is 0.858 and 0.789, respectively, which represent high irrigation uniformity. Note that model predicted irrigation uniformity compares reasonably well with irrigation uniformities obtained for solid-set sprinkler systems with comparable system hydraulics as well as topographic and ambient weather conditions (Zerihun et al., 2011 and Zerihun and Sanchez, 2012).

The simulated field-scale spatial distribution of precipitation depths is summarized in Figure 19a. The spatial distribution pattern is dominated by localized peaks and troughs, hence a larger field-scale pattern could not be discerned. To the best of authors' knowledge, a published sprinkler precipitation depth data (measured or simulated) at the scale of an irrigated field does not exist. Hence, the simulated field-scale spatial distribution of precipitation depths cannot be compared with measured data to test its plausibility. On the other hand, measured depths

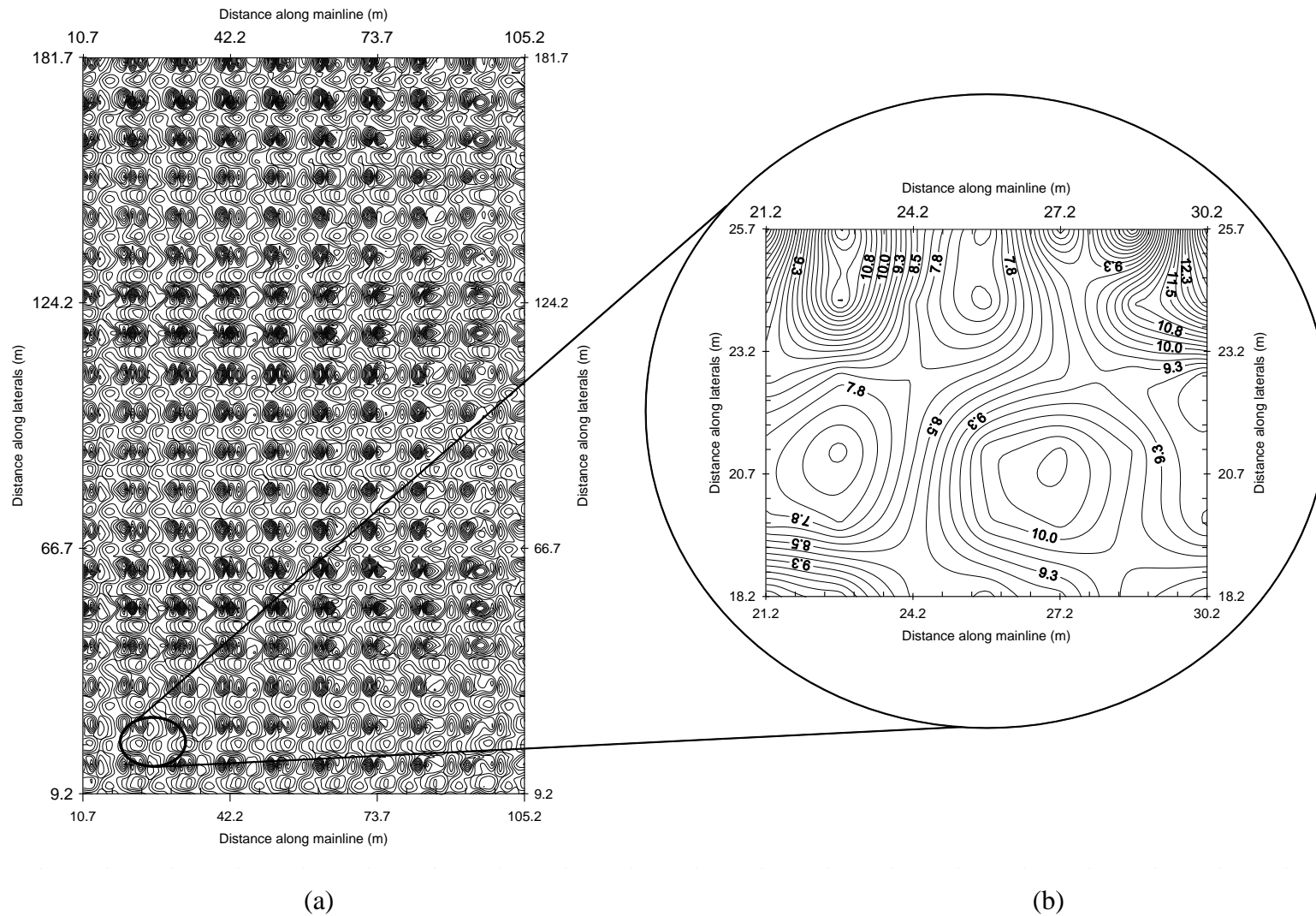


Figure 19 Contours depicting the spatial distribution of sprinkler applied irrigation water (precipitation) that reached the irrigated field surface for sprinkler and lateral spacing's of 9.16m×10.67m: (a) Field-scale distribution and (b) Plot-scale distribution

showing the spatial distribution of precipitation at the scale of a test-plot (a completely overlapped plot) exist (e.g., Zerihun et al., 2011; Zerihun and Sanchez, 2012). Hence, measured plot-scale precipitation depth contours can be compared with simulated ones (extracted from the field-scale data, Figure 19a) to assess the broad plausibility of the results of the field-scale simulation. Accordingly, Figure 19b shows a plot-scale precipitation depth data extracted from the field-scale data summarized in Figure 19a. Experience with measured plot-scale precipitation distribution data suggests that the simulated test-plot scale contours depict a pattern that is not untypical of irrigation distribution at a test-plot scale. Considering that the field-scale spatial distribution of precipitation depths is an aggregation of multiple plot-scale patterns, with limited variation, the preceding observation lends some credence to the plausibility of the simulated field-scale precipitation pattern.

For purpose of comparison consider a scenario in which a sprinkler system, which is exactly the same in all respects as the one described in the preceding section, but has a larger lateral spacing (13.67m or 44.85ft). With such spacing the sprinkler system requires eight laterals to cover the entire field (96.0m×174.0m). Each lateral supplies twenty sprinklers placed at a constant spacing of 9.16m. The corresponding field-scale sprinkler pressure head distribution was simulated with the hydraulic model referenced above. Considering a total dynamic head of 150.75m and elevation at the sprinkler system inlet of 100.0m, the simulated field wide pressure head vary in the range 49.2m to 50.1m, with an average of 49.4m. This represents a maximum field-scale nozzle pressure head variation of 0.9m with respect to the calibration pressure head. Assuming the pressure head variation is sufficiently small, the model parameters derived for the test conditions are applied over the field.

Simulated field-scale spatial distribution of precipitation depths are depicted in Figure 20a. The corresponding field-scale UCC is 0.781 and DU_{lq} is 0.682. Compared to the system with a smaller lateral spacing (10.67m) described above, this represents a decrease in UCC and DU_{lq} of about 9.0% and 14.0%, respectively. The observed trend in terms of decreased uniformity with increased spacing (while keeping all other factors constant) is consistent with the effect of spacing on irrigation uniformity. The model computed E_a is 65.7% and I_r is 0.672 with D_{av} , D_{max} , and D_{min} of 7.1mm, 14.5mm, and 3.9mm, respectively.

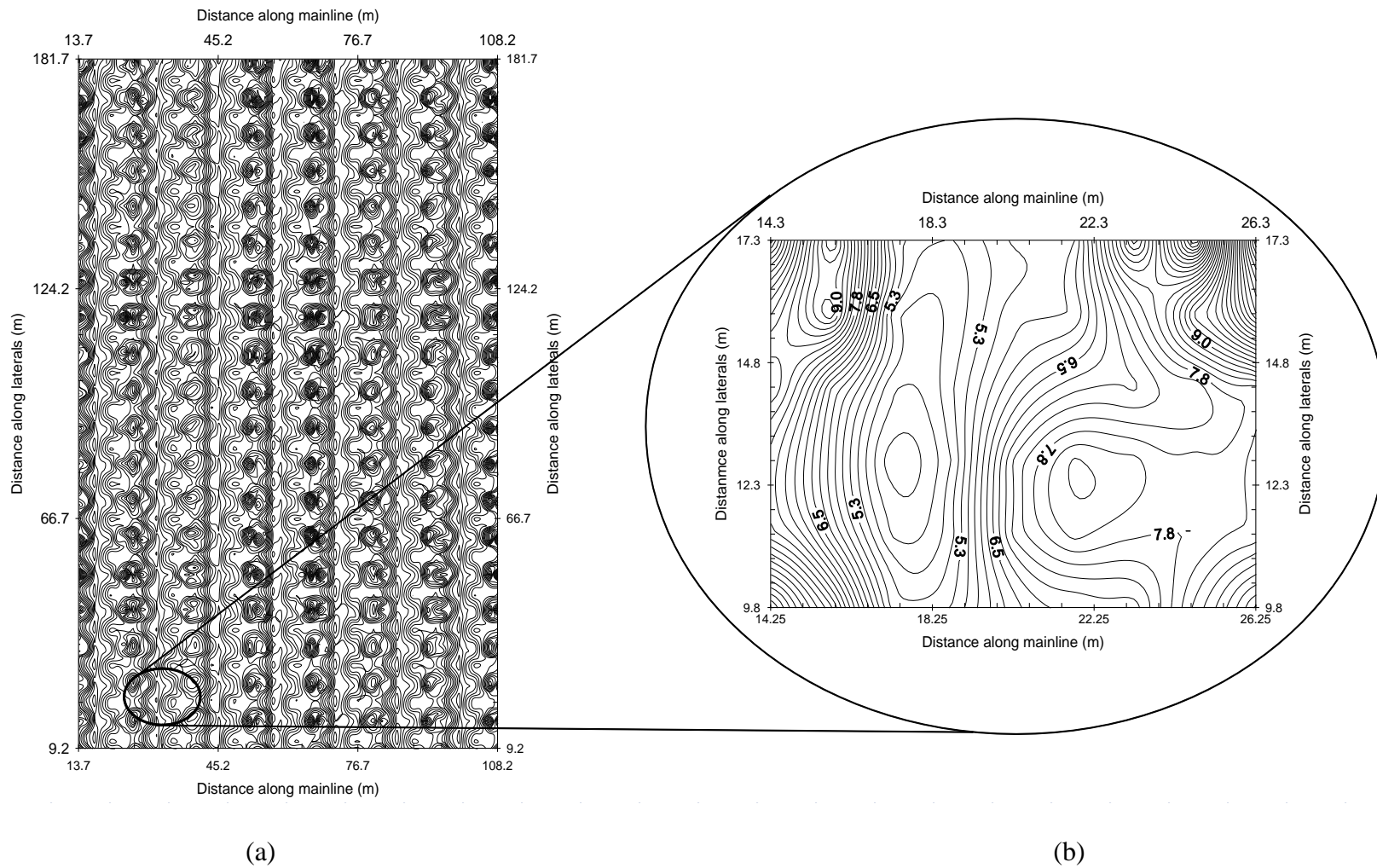


Figure 20 Contours depicting the spatial distribution of sprinkler applied irrigation water (precipitation) that reached the irrigated field surface for sprinkler and lateral spacing's of 9.16m×13.67m: (a) Field-scale distribution and (b) Plot-scale distribution

Application efficiency remained nearly unchanged from that obtained for lateral spacing of 10.67m (66.7%), whereas the irrigation requirement index decreased by 21.0% from 0.848 for lateral spacing of 10.67. Applied volumes in the two scenarios are significantly different: 223.4m³ for the system with 10.67m lateral spacing and 179.3m³ for the system with 13.67m spacing. It can be noted that this is mainly due to the number of sprinklers in the field, rather than pressure head variations. The fact that application efficiency remains essentially unchanged in the two irrigation scenarios implies that, although applied volumes are different, the fraction of the applied volumes retained in the crop root zone is nearly the same in both cases. This implies that for the system with 13.67m spacing the total volume that is retained in the crop root zone is only about 65.6% of 179.3m³ (117.6m³), as opposed to the 148.8m³ (two-thirds of 223.4m³) for the system with lateral spacing of 10.67m. Because the irrigation requirement is the same (required depth, 10.5mm, and irrigated area remain unchanged) for both systems, the substantial difference in the computed irrigation requirement index can be explained by the differences in the fraction of the irrigation volume that is retained in the crop root zone.

The spatial distribution of precipitation for a completely overlapped plot, extracted from the simulated field-scale data (Figure 20a), is depicted in Figure 20b. It can be noted from Figure 20b that the precipitation contours for lateral spacing of 13.67m show a depression (an area of relatively lighter precipitation) that runs across the field plot in a direction perpendicular to the mainline (between distances of about 16.5m and 19.0m). The fact that this area of light irrigation runs parallel to the laterals indicates that it is related to the reduction in precipitation overlap resulting from increased lateral spacing (compared to the smaller spacing of 10.67m).

Chapter 7 Sprinkler irrigation uniformity field evaluations

Irrigation field evaluations were conducted in growers' fields in the Yuma Valley Irrigation Districts. Four datasets, each in a different field, were collected as part of the field studies presented here. Three test-plots were installed in each of the irrigated fields. A test-plot covers a rectangular area of 30.0ft×35.0ft, which is discretized into 42 grid squares measuring 5ft×5ft. A rain gage is placed in each of the grid squares. The tests-plots were installed along the field diagonal and each test-plot is considered to be representing an equal fraction of the total area of the irrigated field. The data from test-plot measurements were used to compute plot scale

irrigation uniformity estimates. The test-plot scale irrigation uniformity estimates were then scaled up to field level through averaging. The field and computational procedure used in the current study, to determine test-plot and field-scale irrigation uniformity, is discussed by Zerihun et al. (2011). The rain gages used here are described in Section 6.3.1. The average wind velocities presented in subsequent discussion are obtained from the Yuma Valley AZMET station and hence represent average values for the area during the uniformity evaluations: i.e., they are not average wind velocities measured in the immediate ambience of the irrigated fields. A summary of the measured plot scale and field-scale irrigation uniformity indices as well as the maximum, minimum, and average depths is given in Table 8.

Irrigation evaluation I: The first irrigation evaluation was conducted in a grower's field with an irrigated area of 630.0ft×1290.0ft. Irrigation duration was 3.0h. The average wind speed in the Yuma Valley during the irrigation is about 1.2 m/s. Computed Christiansen's uniformity coefficient values are 0.883, 0.847, and 0.864 for the upstream end, middle, and downstream end test-plots, respectively (Table 8). The field-scale maximum and minimum collected precipitation depths are 7.6mm and 19.1mm, respectively. The test-plot scale average depths vary from 12.4mm for the middle test-plot to 13.3mm for the downstream end test-plot, with the average depth for the upstream end test-plot being 13.1mm. Distribution uniformity is 0.820 for the upstream end test-plot, 0.731 for the middle test-plot, and is 0.803 for the downstream end test-plot. The field-scale average UCC and DU_{Iq} are 0.864 and 0.784, respectively. The computed UCC and DU_{Iq} for all the test-plots can be considered sufficiently high.

Irrigation evaluation II: The second irrigation field evaluation event was conducted in a section of a grower's farm measuring 420.0ft along the mainline and 1290.0ft along the laterals. The average wind speed in the Yuma Valley area during the irrigation evaluation is 4.5m/s. The duration of the field evaluation was 3.0h. The test-plot UCC values are 0.869, 0.818, and 0.851 for the upstream end, middle, and downstream end test-plots, respectively (Table 8). Test-plot scale DU_{Iq} varies in the range 0.716 to 0.791. The field-scale average UCC and DU_{Iq} are 0.846 and 0.761, respectively. Both the field-scale UCC and DU_{Iq} can be considered acceptably high. Although the relatively high wind speed in the Yuma Valley during the irrigation evaluation suggests a more pronounced adverse effect on uniformity, the measured uniformity levels

indicate that wind speed in the immediate ambience of the irrigated field might have been appreciably lower. The collected precipitation depths vary from a minimum of 7.2mm to 19.1mm over the irrigated field. The field-scale average collected depth is 14.4mm.

Table 8 Field-scale irrigation application uniformity, maximum, minimum, and average depths

Parameters	Irrigation evaluation I					
	Test-plot scale				Field-scale	
		Test-plot				
		1	2	3		
<i>UCC</i>	(-)	0.883	0.847	0.864	0.864	
<i>DU_{lq}</i>	(-)	0.820	0.731	0.803	0.784	
<i>D_{av}</i>	(mm)	13.1	12.4	13.3	12.9	
<i>D_{min}</i>	(mm)	9.5	7.6	9.5	7.6	
<i>D_{max}</i>	(mm)	17.2	16.7	19.1	19.1	
Area	(acre)				18.9	
		Irrigation evaluation II				
<i>UCC</i>	(-)	0.869	0.818	0.851	0.846	
<i>DU_{lq}</i>	(-)	0.791	0.716	0.777	0.761	
<i>D_{av}</i>	(mm)	14.8	14.3	14.0	14.4	
<i>D_{min}</i>	(mm)	9.5	7.3	7.2	7.2	
<i>D_{max}</i>	(mm)	19.1	19.1	19.1	19.1	
Area	(acre)				12.6	
		Irrigation evaluation III				
<i>UCC</i>	(-)	0.728	0.645	0.728	0.7	
<i>DU_{lq}</i>	(-)	0.605	0.488	0.619	0.571	
<i>D_{av}</i>	(mm)	6.6	7.3	8.5	7.4	
<i>D_{min}</i>	(mm)	2.9	1.9	3.3	1.9	
<i>D_{max}</i>	(mm)	14.3	19.1	19.1	19.1	
Area	(acre)				9.0	
		Irrigation evaluation IV				
<i>UCC</i>	(-)	0.724	0.776	0.744	0.748	
<i>DU_{lq}</i>	(-)	0.549	0.614	0.583	0.582	
<i>D_{av}</i>	(mm)	12.6	14.3	12.6	13.2	
<i>D_{min}</i>	(mm)	4.8	6.7	4.8	4.8	
<i>D_{max}</i>	(mm)	19.1	19.1	19.1	19.1	
Area	(acre)				3.4	

Datasets I, II, III, and IV were collected on February 23 and 28 and March 1 and 2 of 2013, respectively

Irrigation evaluation III: The third field evaluation was conducted in a part of a grower's field and covers an area of 315.0ft×1230.0ft. Irrigation duration was 3.0h and 24min. The average wind speed in the Yuma Valley during the irrigation is about 3.3m/s. The computed test-plot scale UCC values are 0.782, 0.645, and 0.728 for the upstream end, middle, and downstream end test-plots, respectively (Table 8). DU_{lq} vary between 0.488 for the middle test-plot and 0.619 for the downstream end test plot. The field-scale collected precipitation depths vary over a wider range of 1.9mm to 19.1mm. Average depths for the test-plots vary between 6.6mm for the upstream end test-plot to 8.5mm for the downstream end test-plot, with the average depth for the middle test-plot being 7.3mm. The computed field-scale UCC and DU_{lq} values of 0.7 and 0.571, respectively, fall well short of the irrigation uniformity levels considered satisfactory for solid-set sprinkler systems. Average wind speed in the Yuma Valley, during the irrigation evaluation, is appreciably higher than what is considered conducive for higher uniformities. However, it is possible that higher wind speeds may not necessarily be the only factor contributing to the low irrigation performance. For instance the relatively lower uniformity (both UCC and DU_{lq}) computed for the middle test-plot, compared to the rest of the test-plots in the field, points to a localized routine maintenance issue and/or improper setting of sprinkler riser pipes as the possible causes. Overall, the relatively poor field-scale DU_{lq} suggests that an evaluation of current irrigation practices and the hydraulics of the irrigation systems may be needed to determine the contributing factors.

Irrigation evaluation IV: The fourth irrigation uniformity evaluation event was conducted in a section of a grower's farm measuring 245.0ft along the mainline and 600.0ft along the laterals. The average wind speed in the Yuma Valley area during the irrigation evaluation is 2.2m/s. The duration of the field evaluation was 3.0h. The test-plot UCC values are 0.724, 0.776, and 0.744 for the upstream end, middle, and downstream end test-plots, respectively (Table 8). Test-plot scale DU_{lq} varies in the range 0.549 to 0.614. The collected precipitation depths vary over a relatively wider range, between a minimum of 4.8mm and a maximum of 19.1mm over the irrigated field. The field-scale average collected depth is 13.2mm. While the computed field-scale UCC value of 0.748 can be considered acceptable, the field-scale DU_{lq} value, of 0.582, is low. The average wind speed in the Yuma Valley during the irrigation evaluation does not suggest that wind may have significant adverse effect on irrigation uniformity. As can be noted

from Table 8, irrigation uniformity as measured by DU_{lq} is poor across the field. Hence, this points to a need for evaluating current irrigation practices and the hydraulics of the sprinkler systems so as to determine the factors contributing to the low field-scale and test-plot scale irrigation uniformities.

Chapter 8 Summary and Recommendations

With increased use of solid set sprinkler systems for season long vegetable production, uniform and efficient application of irrigation water with these systems has become a concern for growers in the Yuma Valley Irrigation Districts. Development of guidelines for efficient irrigation requires the evaluation of existing systems and current operational practices, identification of limitations if any, and the development of design and management tools.

Over the last couple of years (2010-2013) authors have undertaken field and modeling studies of solid set sprinkler irrigation systems in the Yuma Valley Irrigation Districts, the results of which were documented in a series of publications (e.g., Zerihun et al., 2011; Zerihun and Sanchez, 2012). An important outcome of the field studies is the development of a procedure for field-scale irrigation uniformity evaluations. In addition, results of the irrigation evaluations suggest that field-scale irrigation application uniformities in the Yuma Valley Irrigation Districts are typically high (average field-scale UCC and DU_{lq} of about 0.85 and 0.75, respectively). Irrigation uniformity evaluations conducted in growers' fields as part of the current study largely confirms these results with measured field-scale UCC and DU_{lq} for two of the fields exceeding 0.83 and 0.75, respectively. However, computed field-wide uniformity levels for two more fields covered in the current study fell appreciably short of the level considered satisfactory for solid-set sprinkler systems (with $UCC < 0.75$ and $DU_{lq} \leq 0.58$). These results point to a need for a follow up (field and modeling) study to determine the factors contributing to the low performance, through evaluation of current irrigation (maintenance and operational) practices and the hydraulics of the sprinkler systems in those fields. In addition, the field studies have also shown that, even when field-scale irrigation uniformities are high, appreciable variations exist between test-plot scale uniformities within a field.

An efficient and robust sprinkler irrigation model with a capability to fully characterize the performance of a field-scale system can be used as a flexible and inexpensive tool for system

design, management, and evaluation. However the development of such a model remains a challenge. As a step toward this goal, a sprinkler irrigation hydraulic model that can simulate the spatial distribution of nozzle pressure head and discharge over an irrigated field - given the system hydraulic, geometric, and topographic characteristics - was developed and evaluated with field data (Zerihun et al., 2014; Zerihun and Sanchez, 2014a). This model also has a functionality for computing field wide irrigation performance based on test-plot scale field measurements. In addition, the modeling and field studies conducted by the authors also show that a typical sprinkler system in the Yuma Valley Irrigation Districts has a robust hydraulic design. The implication is that system performance should exhibit very low sensitivity to appreciable changes in pipe hydraulic resistance characteristics and field slopes, provided the systems are properly set, maintained, and operated under conducive weather condition. However, the studies have also noted that high irrigation performance does not necessarily translate into high economic return.

As a follow up to the modeling studies, described above, during 2013 authors have been working on the development of a sprinkler irrigation precipitation pattern simulation model capable of computing the spatial distribution of irrigation about sprinklers taking into account sprinkler design factors, sprinkler riser pipe height, nozzle pressure heads, and wind effects. Following the established pattern (Fukui et al., 1980; von Bernuth and Gilley, 1984; Seginer, et al., 1991; Carrion, et al., 2001; Playan et al., 2006), the model consists of two main components. A semi-empirical procedure was used to determine droplet population size, diameter ranges, and volumetric application rates as well as model parameters, as related to acceleration and wind effects on droplet motion. A physically based droplet dynamics model is used to simulate droplet motion, between the sprinkler nozzle and its eventual destination on the irrigated field surface. Equations that form the basis of the droplet dynamics modeling functionality developed here were derived based on a combination of established ideas proposed in earlier studies, cited above, and also new concepts formulated as part of the current study (Zerihun and Sanchez, 2014b). The set of nonlinear ordinary differential equations, governing droplet motion through the ambient air, derived as such are solved numerically with an embedded Runge-Kutta formulas consisting of a fourth-fifth order pair (Mathewes and Fink, 2004; Press et al., 1997; Burden et al., 1981). In addition, as part of the study reported here the physics of droplet dynamics is reviewed in some detail in an accompanying document. Based on a relatively rigorous physical analysis of droplet motion and wind effects on droplet drift and drag an alternative form of the nonlinear

differential equations, describing an impulsively started droplet motion through a viscous fluid (e.g., ambient air) that could be in uniform horizontal motion itself, was derived by the authors and is presented in the accompanying document.

Evaluation of the sprinkler precipitation pattern simulation model was conducted based on a comparison of model output with measured data and through theoretical analyses. The satisfactory agreement obtained between the output of the numerical droplet dynamics submodel and a simplified analytical model, under applicable conditions, suggest that the representation, in the numerical model, of the physics underlying droplet dynamics is sound. In addition, analyses of output of the numerical droplet dynamics model under wind conditions show that model predictions are largely consistent with intuitive physical reasoning. Simulated sprinkler radial precipitation patterns, for a range of nozzle pressure heads, compare reasonably well with measurements obtained under no-wind conditions. Furthermore, a limited functional evaluation of the sprinkler precipitation pattern model, based on a comparison of simulated and measured irrigation uniformity and precipitation depths, suggest that the accuracy of the model is satisfactory.

The potential application of the precipitation pattern simulation model in field-scale irrigation performance evaluation was explored. The results of the field-scale simulation study suggest that the development of a coupled hydraulic, precipitation pattern, and soil water flow simulation model for use in field wide irrigation performance evaluation is technically feasible. However, for the coupled field-scale irrigation model to be efficient and practically useful some significant limitations of the sprinkler irrigation precipitation pattern simulation model, pertaining to computational efficiency and parameter estimation, need to be addressed prior to model coupling.

The following discusses the limitations of the precipitation pattern simulation model, developed here, and the indoor and field evaluation procedures applied in the current study and outlines recommendations for further studies:

(1) Considering the range of droplet diameter, angular, and field discretization steps used in the numerical simulations conducted as part of this study, the average model run time required to simulate the precipitation pattern about a sprinkler (in a Dell desktop computer with a RAM of 6GB and a regular Intel Xeon processor, with speed of 2.8GH) is approximately 20 sec. In which

case, a field-scale simulation of the spatial distribution of irrigation over an average size field in the Yuma Valley Irrigation Districts (typically consisting of hundreds of sprinklers), considering the hourly average wind velocity and pressure head variations over each sprinkler in the field, may require hours of computer run time. The implication is that the development of an efficient and practically useful sprinkler irrigation design, management, and evaluation model requires substantial improvements, in the computational efficiency of the precipitation pattern modeling functionality. Further studies that may contribute to the development of a computationally efficient field-scale sprinkler irrigation model may include:

- (i) The tradeoff between numerical efficiency and accuracy, of sprinkler precipitation pattern simulations, stemming from the use of different combinations of angular, droplet diameter, and irrigated field discretization step sizes needs to be studied in some detail to ascertain ranges of numerical discretization step sizes that could lead to reasonably accurate yet efficient simulations.
- (ii) The use of more efficient computational techniques that can fully exploit the rather powerful hardware (multiple core processors) routinely available in current PCs may need to be explored.
- (iii) Experience with measured data and intuitive physical reasoning suggest that sprinkler pressure head variation within a limited range might not lead to significant variations in sprinkler precipitation patterns. On the other hand, in a typical sprinkler system, pressure head variation between sprinklers, that are in close proximity, is negligible. The implication is that for a field wide irrigation simulation, consideration of pressure head variations at every sprinkler in an irrigated field may not lead to appreciable gain in accuracy to offset the computational overhead that it entails. In which case, the pressure head range over an irrigated field can be discretized into a suitably selected number of subintervals that are sufficiently small, such that the range of variation in sprinkler precipitation pattern within a (pressure head) subinterval can be considered negligible. It can then be assumed that each subinterval can be represented in terms of a single parameter set, associated with an average nozzle pressure head for the subinterval, with satisfactory accuracy. Such an approach can

substantially improve the computational efficiency of a field-scale sprinkler irrigation model and can reduce the number of required indoor and field measurements to a practically manageable size. However, this requires the development of a procedure for the optimal discretization of a given field wide sprinkler pressure head range into sufficiently small subintervals that leads to improved computational efficiency without impairing accuracy.

(iv) Potential improvements in computational efficiency that may accrue from the solution of the equations of sprinkler irrigation droplet dynamics with alternative numerical techniques, including implicit Runge-Kutta methods and perhaps some of the multi-step methods, may need to be explored.

(2) Currently measured sprinkler radial application rate data is specified at the (model) input in terms of the parameters of a cubic polynomial derived through curve fitting, which introduces some error into the computed droplet diameter ranges and droplet volumetric application rates. A more accurate estimate of sprinkler radial application rates can be obtained through the implementation of a numerical algorithm that directly interpolates radial precipitation rates from measured data, given a radial distance from the test sprinkler.

(3) The accuracy of model prediction, to a significant extent, depends on the accuracy with which model parameters are estimated. Model parameter related issues that may require further studies include:

(i) Depending on the option used to specify wind velocity data at the input, the number of model parameters may vary from a minimum of three to approximately twice as many as the number of hours in the irrigation application duration. Considering the number of model parameters, which could be appreciable, and in any case not sufficiently small to be amenable to simple trial and error based approaches; the development of a parameter estimation functionality with an efficient and robust inverse modeling algorithm is essential for accurate simulation of precipitation patterns about sprinklers. Hence, the model developed here requires further development along these lines.

(ii) Although droplet acceleration effect on drag is known to vary with droplet diameter and its state of motion relative to the ambient air; for reasons of simplicity, in the current model, the empirical drag correction parameter for droplet acceleration effects is considered a constant, given the sprinkler model, nozzle size and pressure head, and wind condition. In which case, this parameter is effectively an empirical sprinkler precipitation pattern shape fitting coefficient. Evaluation of the significance of the limitation that this assumption imposes on the accuracy of model prediction could be useful. A similar analysis with respect to the parameters that take into account wind effects on droplet drag and drift may also be needed.

(iii) Additional studies aimed at, evaluating the interrelationship between model parameters (in terms of their effect on droplet motion and the precipitation pattern about a sprinkler) and, establishing specific limits on the ranges of variations of model parameters may need to be conducted.

(iv) Model parameters derived based on the semi-empirical procedure described here are specific to the sprinkler model and nozzle size, sprinkler riser pipe height, nozzle pressure head, and wind velocity, hence limiting the predictive capability of the model. Studies aimed at the development of a database of model parameters for commonly used sprinklers and settings as a function of a set of sprinkler pressure heads (within the range recommended by the sprinkler manufacturer) and a set of average hourly wind speeds (within the range of wind speeds under which sprinkler systems are commonly operated) could be useful in enhancing the applicability of such models in field-scale sprinkler system design and management.

(4) A more extensive evaluation of the model with measured data, covering a wider range of conditions, may need to be conducted to fully ascertain its range of applicability and limitations. Additional evaluations of the accuracy of the numerical solutions implemented in the current model through comparisons with those obtained based on alternative numerical techniques, mentioned in a preceding paragraph, could be useful.

(5) The equations describing droplet dynamics in the context of sprinkler irrigation under no-wind condition has a sound physical basis. However, approaches used to take into account wind effects on droplet motion, which commonly involve empirical modifications of the equations applicable to no-wind condition, may require further examination and development. As part of the current study, an effort was made to conduct a relatively rigorous analysis of the problem of sprinkler irrigation droplet dynamics, on the basis of which authors have formulated alternative equations for taking into account wind effects on droplet drift and drag. These equations are can be solved numerically with well established techniques. Hence, a comparative evaluation of sprinkler droplet dynamics models based on the new set of equations, proposed here, with those based on existing approaches could be useful. The soundness of the physical and mathematical reasoning that underlie the derivation of the equations and the amenability of the equations to efficient and accurate numerical solution with applicable techniques can be among the factors in terms of which these models can be evaluated.

(6) Considering the procedure used in the current study, conditions that need to be met, for the determination of sprinkler radial application rate with satisfactory accuracy, consist of: (i) the single sprinkler indoor evaluations need to be conducted under an environment that minimizes spray evaporation losses without causing condensation and (ii) the spacing between rain gages needs to be sufficiently small for the depth collected in a rain gage to be considered a representative average of the corresponding annular ring of irrigated area. Standardization of the indoor test procedure may help ensure that these conditions are closely approximated during the evaluations, thereby improving the accuracy of measured sprinkler radial application rates. Hence, further studies aimed at identifying the range of rain gage spacing's for acceptable accuracy as well as the development of a practically useful and inexpensive procedure (materials and methods) for environmental control and automation of measurements may need to be conducted.

(7) In the study reported here estimates of spray evaporation losses, from the single sprinkler field evaluations, were obtained with a volume balance method. This approach has the advantage of being simple and fully consistent with measured data. However, it is generally perceived that single sprinklers exert a lesser influence on the micro-climate of the test-plot, and the

surrounding area, than a system of overlapping sprinklers do over an irrigated field. Hence, the transferability of spray evaporation estimates, derived as such, to field-scale simulation applications depends on the significance of this difference on micro-climatic effects of the two irrigation scenarios. This suggests that further studies are needed to evaluate the significance of the difference in micro-climatic effects between a single sprinkler and a system of multiple, overlapping sprinklers, operating under the same set of field conditions. As part of such a study, the potential application of existing semi-empirical approaches for computing spray evaporation fractions (as a function of climatic factors) and their comparative advantage/limitations with respect to the approach used here, can be explored.

(8) The approach used in the current study for droplet volumetric application rate characterization presumes that for a given sprinkler and nozzle pressure head combination the underlying droplet size distribution remains unchanged regardless of the state of motion of the ambient air. It then follows that sprinkler droplet volumetric application rates derived based on indoor measurements, undertaken at a given nozzle pressure head, can be applied to a sprinkler of the same model, nozzle size, and riser pipe height, operating under field conditions. The implication is that wind effects on sprinkler precipitation pattern can be considered to be confined to the distortions it introduces to the trajectory of individual droplets, which is then taken into account through empirical parameters. However, there are studies that show that the formation of droplets and the resulting droplet size distribution is a function of the state of motion of the ambient air as well as the irrigation stream and the subsequently formed droplets. This suggests that further studies are needed to evaluate the significance of wind effects on sprinkler droplet size distribution and hence the error that the relevant simplifying assumptions introduce into sprinkler irrigation precipitation pattern simulation models.

References

- Bilanski, W.K. and Kidder, E.H. (1958). Factors that affect the distribution of water from a medium-pressure rotary irrigation sprinkler. *Trans ASAE*, 1(1):19-28.
- Burden, L.R., Fairies, J.D., and Reynolds, A.C. (1981). *Numerical analysis*. Prindle, Weber, & Schmidt, Boston, MA.

- Burguete, J., Playan, E., Montero, J., Zapata, N. (2007). Improving drop size and velocity estimates of an optical disdrometer: Implications for sprinkler irrigation simulation. *Trans ASABE*, 50(6):2103-2116.
- Carrion, P. Tarjuelo, J.M., Montero, J. (2001). SIRIAS: a simulation model for sprinkler Irrigation, I. Description. *Irrig. Sci.* (2001)20:73-84.
- Cartwright, J.H.E. and Piro, O. (1992). The dynamics of Runge-Kutta methods. *Int. J. Bifur. Chaos.*, 2:427-449.
- Dormand, J.R. (1996). *Numerical methods for differential equations: A computational approach*. CRC Press, Inc., Boca Raton, FL.
- Eigel, J.D. and Moore, I.D. (1983). A simplified technique for measuring rain drop size and Distribution. *Trans. ASAE*, 26(4):1079-1084.
- Fukui, Y., Nakanishi, K., and Okamura, S. (1980). Computer simulation of sprinkler irrigation uniformity. *Irrig. Sci.*, (1980)2:23-32.
- Goering, C.E., Bode, L.E., and Gebhardt, M.R. (1972). Mathematical modeling of spray droplet deceleration and evaporation. *Trans. ASAE.*, 15(2):220-225.
- Green, R. (1952). Evaluation of air resistance to freely falling drops of water. *Agric. Eng.* 33(1):28.
- Kincaid, D.C. and Longley, T.S. (1989). A water droplet evaporation and temperature model. *Trans. ASAE*, 32(2):457-462.
- Kincaid, D.C., Solomon, K.H., and Oliphant, J.C. (1996). Drop size distribution for irrigation sprinklers. *Trans ASAE*, 39(3):839-845.
- Kohl, R.A. (1974). Drop size distribution from medium-sized agricultural sprinklers. *Trans ASAE*, 17(5):690-693.
- Laws, J.O. (1941). Measurement of the fall velocity of water-drops and raindrops. *Trans Am. Geophys. Union*, (22):709-721.
- Mathews, J.M. and Fink, K.D. (2004). *Numerical methods using Matlab*. Prentice Hall Inc., Upper Saddle River, NJ.
- Miesse, C.C. (1955). Correlation of experimental data on the disintegration of liquid jets. *Ind. Eng. Chem.*, 47(9):1690-1701.

- Playan, E., Burguete, J., Zapata, N., Salvador, R., Bautista-Capetillo, C., Cavero, J., Martinez-Cob, A., Faci, J. and Dechmi, F. (2009). Mathematical problems and solutions in sprinkler irrigation. *Monografias de la Real Academia de Ciencias de Zaragoza*, 31:153-174.
- Playan, E., Slavador, R., Faci, J.M., Zapata, N., Martinez-Cob, A., Sanchez, I. (2005). Day and night wind drift and evaporation losses in sprinkler solid-sets and moving laterals. *Agric. Water Manag.*, 76(2005):139-159.
- Playan, E., Zapata, N., Faci, J.M., Tolosa, D., Lacueva, J.L., Pelegrin, J., Salvador, R., Sanchez, I., and Lafita, A. (2006). Assessing sprinkler irrigation uniformity using a ballistic simulation model. *Agric. Water Manag.*, 84(2006):89-100.
- Press, W.H., Teukolsky, S.A, Vetterling, W.T., and Flannery, B.P (1997). *Numerical Recipes in C, the art of scientific computing*. Cambridge University Press, New York, NY.
- Salvador, R., Bautista-Capetillo, C., Burguete, J., Zapata, N., Serreta, A., and Playan, E.. (2009). A photographic method for drop characterization in agricultural sprinklers. *Irrig Sci.*, (2009)27:307-317.
- Seginer, I. (1965). Tangential velocity of sprinkler drops. *Trans ASAE*, 8(1): 90-93.
- Seginer, I., Nir, D., von Bernuth, R.D. (1991). Simulation of wind distorted sprinkler patterns. *J. Irrig. Drain Eng.*, ASCE, 117(2):285-306.
- Silva, W., and James, L.G. (1988). Modeling evaporation and microclimate changes in sprinkle irrigation: I. Model formulation and calibration. *Trans. ASAE*, 31(5):1481-1486.
- Smith, R. (1970). Analog simulation of in-flight evaporation of spray droplets. *Trans ASAE*, 587-593.
- Stroud, A.H. (1974). *Numerical quadrature and solution of ordinary differential equations*. Springer Verlag, New York, NY.
- Temkin, S. and Kim, S.S. (1980). Droplet motion induced by weak shock waves. *J. Fluid Mech*, 96(1):133-157.
- Temkin, S. and Mehta, H.K. (1982). Droplet drag in accelerating and decelerating flow. *J. Fluid Mech* (116):297-313.
- Thompson, A.L., Gilley, J.R., and Norman, J.M. (1993a). A sprinkler water droplet evaporation and plant canopy model; II. Model development. *Trans. ASAE*, 36(3):735-741.

- Thompson, A.L., Gilley, J.R., and Norman, J.M. (1993b). A sprinkler water droplet evaporation and plant canopy model; II. Model application. *Trans. ASAE*, 36(3):743-750.
- von Bernuth, R.D. (1988). Effect of trajectory angle on performance of sprinklers in wind. *J. irrig. Drain Eng.*, ASCE, 114(4):579-587.
- von Bernuth, R.D. and Gilley, J.R. (1984). Sprinkler droplet size distribution estimation from single leg test data. *Trans. ASAE*, 27(5):1435-1141.
- Vories, E.D., von Bernuth, R.D., and Michelson, R.H. (1987). Simulating sprinkler performance in wind. *J. Irrig Drain Eng.*, ASCE, 113(1):119-130.
- Zerihun, D. and Sanchez, C.A. (2012). Field and modeling study of sprinkler irrigation for season long vegetable production in the Yuma Valley Irrigation Districts, *Report submitted to the USBR*.
- Zerihun, D. and Sanchez, C.A. (2014a). A field-scale sprinkler irrigation system hydraulic model, II: hydraulic simulation. *J. Irrig Drain Eng*, ASCE, *in Press*.
- Zerihun, D. and Sanchez, C.A. (2014b). Sprinkler irrigation droplet dynamics: a review and theoretical development. *A report submitted to the USBR*.
- Zerihun, D., Sanchez, C.A., and Nolte, K. (2011). Evaluation of sprinkler irrigation system for season long vegetable production in the Yuma Valley Irrigation District. *Report submitted to Arizona Specialty Crops Council*.
- Zerihun, D., Sanchez, C.A, and Nolte, K. (2014). A field-scale sprinkler irrigation system hydraulic model, I: Hydraulic characterization. *J. Irrig Drain Eng*, ASCE, *in Press*.